DAVID PUBLISHING

From Knowledge to Wisdom

Journal of Mechanics Engineering and Automation

Journal of Mechanics Engineering and Automation

Volume 4, Number 4, April 2014 (Serial Number 34)

Contents

Experimental Vehicles Program Aides in Innovative Hands-on Learning Experiences

Saeed Foroudastan[1] and Brigette Prater Thompson[2]

1. College of Basic and Applied Sciences, Middle Tennessee State University, Murfreesboro 37132, United States

2. Masters of Science in Professional Science, Middle Tennessee State University, Murfreesboro 37132, United States

Abstract: The EVP (experimental vehicles program) was created in 2004 as an umbrella program for five different undergraduate experimental vehicle design teams. These projects consist of the Solar Vehicle, Moonbuggy, Baja SAE (sina app engine), Formula SAE and Solar Boat. The goal of the EVP is to foster undergraduate student development through hands-on construction of experimental vehicles with the guidance of faculty mentors and partnerships with both national and international industry leaders. Each EVP project performs a vital function in the professional development of students. The projects provide a forgiving environment in which students can test their classroom knowledge in a real-world setting and learn important skills such as leadership, effective communication and working as a team member. Furthermore, the students in the EVP develop highly versatile and qualified skill sets that will allow them to fill various positions within the workplace. In the past, 90% of EVP graduates have been able to obtain highly regarded national and international positions upon graduation due to their real-world experience gained throughout their involvement in the EVP. Each year the EVP sponsors up to 60 interdisciplinary students that come together in peer-led teams to combine and expand upon their classroom knowledge in building innovative vehicles. The successes of the MTSU (Middle Tennessee State University) EVP have been recognized by becoming the national model for hands-on engineering education; helping engineering students take classroom knowledge and apply it to real-world situations. Students work to design, construct, and test novel vehicle designs for participation in national and international competitions. Due to the competitive nature of each of the events, students must use cutting edge technology and design methods in order to create the best entries possible. Often times, this means creating partnerships with industry leaders who help mentor the students from the design conception, the fabrication through the manufacturing of each vehicle.

Key words: Innovative vehicles, professional development, industry partnerships.

1. Introduction

The rising demand for inventive technology has had a strong influence on modern national and international engineering curricula over the past several years. Competent, innovative engineers are needed now more than ever to help solve some of the most complicated problems in the advancement of the engineering industry. The various projects of the MTSU (Middle Tennessee State University's) EVP (experimental vehicles program) allow engineering technology students to apply their innovative ideas and classroom

knowledge to real-world problems. Projects such as the Solar Boat, Moonbuggy, Mini Baja SAE (Sina App Engine), and Formula SAE supply a creative environment to nurture and inspire innovative thinking which allows students to give rises to groundbreaking technologies such as the carbon fiber structure used in the Formula SAE and Solar Boat vehicles.

Each year, the EVP students create a new, increasingly efficient, well-designed vehicle for each of the five projects. These projects attract roughly 40 new students each year from a variety of age groups and backgrounds. With a common goal in mind the students are separated into peer-led teams consisting of both new faces to EVP and members that have remained involved in the projects throughout their

Corresponding author: Saeed Foroudastan, Ph.D., professor, research fields: engineering science and mechanics. E-mail: saeed.foroudastan@mtsu.edu.

secondary education. This helps to insure continuity as well as collaboration within the vehicle teams. Success of these vehicles by winning awards at national and international competitions is primarily the reflection of the innovation and dedication of MTSU students. The unique research projects provide great benefits for the professional development of engineering and engineering technology students. Hands-on learning is a direct application of classroom concepts. In addition, these particular projects help students learn to think innovatively, communicate professionally, manage projects efficiently, and work in a team environment [1]. The competitions are also an opportunity for MTSU students to associate with other students from engineering schools around the country and globe [2].

Although most participants represent engineering and engineering technology majors, students from various disciplines have participated within the program. Students think creatively to design their blueprints, construct each vehicle from scratch, and enter each project into its respective competition. Each competition is composed of several events, providing a unique set of challenges along with racing against some of the top engineering schools in the nation including Georgia Institute of Technology (ranked 4th), the University of Illinois Urbana Champaign (ranked 5th), and Cornell University (ranked 11th) [3].

The program provides a large range of students with a diverse collection of projects to facilitate excellence in engineering technology education and to encourage undergraduate participation through innovative, competitive research. Students work diligently on these projects and incorporate skills needed in the workforce: project management, decision making, leadership, critical analysis, and problem solving. Participants learn the value of research, teamwork, and effective communication. They learn to incorporate innovative ideas into a single goal, complete projects, and excel at competitions. In addition, the national and international design competitions provide valuable exposure for

Middle Tennessee State University and EVP partners [2].

These projects also provide invaluable experiences which give EVP students a competitive edge in the job market upon graduation. MTSU engineering technology students must function together as a team to research, design, build, test, promote, and race each vehicle in national and international competitions. The innovative projects have increased interest in engineering, incorporated classroom learning into hands-on experiences, and fostered an atmosphere of peer-led team learning which has benefited the students both personally and academically. The remainder of the article goes into further detail about the specific projects the students engage in during their time with the EVP. The article also highlights the benefits of undergraduate research by enhancing both retention and graduation rates within the EVP populous. Section 2 talks about the four experimental vehicle projects of the EVP; Section 3 refers to the increased graduation and retention rates encouraged by EVP participation; Section 4 concludes the article.

2. Innovative Design Developed at MTSU

Because of the competitive nature of each event the EVP participates in, students must use cutting edge technology and design methods in order to field the very best entry possible. Often, these projects serve as rolling test beds for the latest innovations in various technical fields and are accompanied by a great deal of student research.

2.1 Solar Boat

MTSU offers several nationally competitive experimental vehicle projects as extracurricular activities for undergraduate engineering technology students [4], including a solar boat project. The solar boat project was founded following the inception of the Institute of Electrical and Electronics Engineers Power Electronics Society's Solar Splash Competition, an international collegiate competition showcasing

solar/electric boating [5]. The solar boat project focuses on the capture, utilization, and storage of solar energy to power a special-purpose boat. The boat design must follow a set of regulations to accomplish numerous pre-determined outcomes [6]. Nevertheless, the students are given a large amount of freedom in the design and operation of their solar boat. The project culminates at the annual five-day competition where the students showcase their efforts and compete against other student design teams in various categories [5]. The Solar Splash Competition may be classified as a "brain sport", an activity giving engineering students an opportunity to experience real-world design and engineering problems [7].

The overarching theme of the solar boat project is to encourage students to excel in their studies and to get them excited about solar energy. It has been noted that past solar boat students became so interested in their projects that they actively pursued careers in the solar and other alternative energy fields. The project provides the fundamental knowledge and hands-on experience valued by employers, and serves to fill in any gaps in understanding from the students' classroom education.

The EVP solar boat team members collaborate on all decisions throughout the lifetime of their project. Together the students decide how they want to build their boat as well as conduct all the necessary research, construction, and testing in preparation for the annual competition. During the solar boat project, students are faced with challenging dilemmas that are best solved through creative problem solving. For example, the 2012 solar boat incorporated an innovative drivetrain system seen in Fig. 1.

The drive system provides adjustable trim while simultaneously facilitating rudderless steering. This groundbreaking steering integrates interchangeable motors, transom-mounted surface drive, interchangeable sprockets for variable gear ratios that allow for a wide variety of torque and horsepower combinations, and therefore a high degree of adjustability. The drive system

Fig. 1　Solar boat drivetrain.

is also outfitted with surface-piercing propellers, which dramatically increase propeller efficiencies by decreasing overall propeller slip. This type of innovative drivetrain had never before been attempted at MTSU.

Furthermore, the 2012 team constructed the hull completely of carbon fiber paired with a special core material known as Lantor® Soric XF3. This core material, while serving as an inter-laminar breather material, also serves as a buoyant foam-core material similar to Nomex® honeycomb, but at a fraction of the cost. By utilizing this low-cost option, the team was able to construct a lightweight, structurally rigid hull with a finished weight of approximately 90 pounds.

In addition, a new wireless data acquisition system was developed to allow an onshore pit crew to collect and analyze data while simultaneously adjusting motor controller parameters to carefully regulate the power consumption of the electrical system, especially during the endurance races. For ease and simplicity, this system utilizes parameter monitoring functions of the motor controllers paired with an over-the-counter microcontroller and simple transducers to provide a complete analysis of the system without an overpriced data acquisition unit and software.

2.2 Moonbuggy

The Moonbuggy project is a versatile vehicle that has inspired MTSU undergraduates to create novel

engineering innovations. The Moonbuggy is designed to be a lightweight, compact, flexible and durable "all-terrain" vehicle. According to the NASA-sponsored Great Moonbuggy Race rules the vehicle must be human powered and controlled by one male and one female student over a half-mile simulated lunar terrain full blown with craters, "lava" ridges, rocks, inclines and lunar soil. To further complicate the race, and force students to think outside the box, students are required to carry the un-assembled vehicle to the starting line and are then judged on assembly time. The vehicles are also judged on the performance over the terrain and the overall design. Students involved in the project each year work diligently to incorporate new and innovative designs to enhance the performance of the Moonbuggy over the lunar topography.

Brainstorming as a team prior to the fabrication of the vehicle has led to exciting inventive breakthroughs in the past such as the carbon fiber frame and groundbreaking wheel design. Eighty to ninety percent of all vehicle fabrication and assembly is carried out in MTSU's Voorhies Industrial Studies Complex in a dedicated workspaces by EVP students.

Every year students have paid close attention to the wheels of the vehicle, fabricating them entirely in the engineering laboratories at MTSU. Some of the most innovative discoveries by the EVP students came a few years ago when the wheels were constructed from 1/2" aluminum stock and measured 21 inches in diameter, with a 2.5" tire. The design consists of six identical sections bolted to a central aluminum plate as shown in Fig. 2. The spokes were made on a CNC (computer numerical control) machine from a design that eliminates the imminent strength problems that most teams encounter with classic bicycle spokes. The spokes increase the strength of the wheels, but also allowed for the replacement of only the affected part in the event of damage.

Last year's Moonbuggy team took thinking outside of the box to a new level when they designed a

Fig. 2   Six spoke aluminum wheel.

competition vehicle containing six wheels instead of the usual four. This groundbreaking vehicle design was the first of its kind to be used in the Moonbuggy competition. The six-wheel conformation distributes weight over a larger area and imparts greater stability and a wider distribution of traction for the wheels. The long, narrow chassis also ensured that the vehicle could fit on the race track and make tight turns. By using a six wheels design allowed the vehicle to be streamlined; the vehicle was able to maneuver around the competition course with incredible flexibility and speed.

To improve upon last year's model this year students are creating the chassis and main components from schedule 6063 aluminum tubing with a 0.133 wall thickness. The elastic and ductile properties of the material allow it to deform under stress, making it good for absorbing shock when the Moonbuggy is driven over rough terrain or is subjected to sudden and intense forces. This material is ideal for a lunar vehicle due to its exceptional strength to weight ratio allowing easy maneuverability in a low gravity atmosphere. The vehicle shown in Fig. 3 was very successful during competition.

2.3 Baja SAE

The Baja SAE vehicle is designed to be a single seat off-road recreational vehicle that is safe, fun to drive, easy to maintain, and has the ability to be mass produced and sold to the public. The Society of Automotive Engineers sponsors an annual competition to test all components of the vehicles design on various

Fig. 3   2013 Moonbuggy.

Fig. 4   Baja SAE during competition.

terrains. Fig. 4 shows one of MTSU's past Baja SAE designs in the midst of the competition.

Past EVP Baja SAE teams have developed an innovative body that is capable of withstanding tough terrains while keeping its passenger comfortable and safe. Probably the most innovative design to come from this vehicle was its Galexy gear setup, which impressed the likes of Nissan engineers at recent completions. This innovative gear design was created solely by EVP students and was manufactured in MTSU engineering laboratories.

The frame of the Baja SAE was designed to consider ease of manufacturing as well as safety. MTSU students had to create a vehicle design that was durable and light enough to cross an irregular terrain while at the same time keeping its passenger safe and comfortable. In an effort to eliminate a cramped cockpit all steering and braking as well as throttle mechanisms were located in a front cage bulk head. This provided extra safety for the driver's feet in the event of a head on collision. The cockpit also has a

sizable compartment where most drivers will have no problem fitting into. This allows for a larger range in driver body type and size to be comfortable in a cross-terrain vehicle. Additionally, MTSU students designed body panels that were constructed with .08" thick Lexan to provide ample durability and protection to the driver. This Lexan has been proven to withstand high impacts of sharp and dull objects with destructive testing methods. All testing of vehicle material was done within the MTSU engineering laboratories. Along with the body panels, Baja team members constructed Skid plates which were fabricated out of .125" thick steel to protect the driver as well as the drive-train and rear brake.

The Baja design teams also took into consideration accessibility to critical portions of the vehicle in the event of a breakdown. The engine bay on the rear of the car is designed to facilitate prompt access to the drive-train in the event of a failure. This will allow repairs to be done without necessarily removing the engine. This allows repairs to be done quickly and without unnecessary tools.

2.4 Formula SAE

The Formula SAE vehicle is designed to be an open wheeled racer and must adhere to strict guidelines set forth by Society of Automotive Engineers. The Formula SAE Collegiate Competition is an annual competition where entries are judged not only by their performance on the track, but also by their technical and engineering innovation. Teams are also required to show manufacturability of their concept, and must prove their design on its merits before proving it on the track. Fig. 5 shows MTSU's Formula SAE while competing on the track.

Formula SAE teams over the years have struggled with finding creative ways in which to gain enough power to race the vehicles under the strict guidelines of the competition committee and still maintain a safe environment. Safety of the driver was paramount and as such, 1" × .095" wall mild steel tube was used to

Fig. 5   Formula SAE during competition.

create the main and front hoops. Portions of the frame directly protecting the driver, such as the impact attenuator area, as well as portions of the frame directly carrying suspension loading points and harness points were designed with 1" × .065" wall mild steel tubing. Additional supportive bracing tubes were designed with 1" × .049" wall mild steel tubing to minimize weight while maintaining node to node tensile and compressive strength. The tube frame was TIG (tungsten inert gas) welded for maximum flexibility in the welding process.

Autodesk Inventor was used to design the vehicle and to perform stress analysis to further ensure the safety of the EVP team.

3. Retention and Graduation

The first major retention issue the EVP projects target is the lack of a well-defined student support systems. Numerous studies have shown that students who are involved in small groups retain more than students who work alone [8]. Isolation of a student from his or her peers can cause stress beyond that imposed by an already formidable field of study. At the beginning of each school year, the EVP projects falls under the responsibility of a group of approximately 60 students who opt to become members of the University's Solar Boat Team, Moonbuggy Team, Mini Baja Team or Formula SAE Team. Students from any background and major are invited to attend, though historically teams have primarily consisted of students from the engineering technology department. All EVP teams are primarily student-led, with assistance

provided by the Faculty Advisor and numerous University staff members. Team organization and operation relies on a modified and proven PL-TL (peer-led, team-learning) model [9], where students support and mentor each other throughout the course of the project. The PL-TL model is designed to supplement classroom lectures by requiring students to engage in active group learning. The group environment can prove more conducive to learning than a classroom setting, as the students feel less pressure to provide correct answers or "textbook solutions" to the problem at hand. The benefits of group activities to engineering-student retention have been well-documented. A study conducted by Foroudastan reported that student involvement in group learning environments promoted student retention. Foroudastan writes that "For some students, the collaborative environment of the learning community provided a safe place, a smaller knowable place of belonging, in which they were valued and in which they discovered they could learn [9]".

The second problematic issue the EVP projects seek to mitigate is the suppression of creativity and ingenuity. In mathematics and engineering, much value is placed on achieving single, correct answers with no additional credit awarded for innovative approaches to problem solving [4]. Students are often discouraged to recognize or explore alternative approaches to problems. The fear of being wrong or labeled as "unusual" can lead to excessive reliance on stilted or rote problem solving skills [4], which may likely discourage some students from remaining in or entering the engineering field. Conventional and uncreative behavior is directly counter to the qualities desired of future innovators, especially those expected to tackle some of the most important engineering issues ever encountered in modern human history. As per the PL-TL model, the more senior students lead the inexperienced students [8]. The students often develop strong relationships with their teammates, which in turn encourages them to continue the pursuit of the

project and their degree. Such academic and social support networks are crucial components of student retention [10]. The aim of all collegiate engineering programs is to produce sophisticated and talented engineers who are ready to enter the workforce upon graduation. Many students may leave the engineering discipline or choose not to pursue such a career because they lack confidence in their knowledge and abilities, namely in mathematics and science. The EVP projects seek to encourage students to put their hands on an actual project and gain experience regardless of their opinion of their engineering skills.

At the beginning of the projects, there is no right or wrong solution, and students of all backgrounds and skill levels combine their ideas as they work towards a common goal. The learning objective of the projects is to test out a variety of theories and methods and to investigate the consequences of each decision. Mistakes are seen as learning opportunities for the future. Even if a student lacked confidence in his or her abilities as an engineer, such hands-on experiences are often the spark that fires the creative imagination that causes the student to become fascinated with solar energy and the future of alternative fuel, making him or her more likely to continue studying engineering and engineering technology.

The EVP takes engineering students beyond classroom learning. Though students may amass a large amount of knowledge in the classroom and feel confident in their abilities prior to graduation, they could feel overwhelmed once entering the workforce, deterring them from remaining in an engineering field. Difficult or seemingly esoteric concepts can be made clear through direct application or visualization via a hands-on undergraduate engineering project. Through the active development of the vehicles, students gain appreciation for the development of a design from the concept-phase through final production. The students learn how to respect both ergonomic and equipment restraints—a fundamental consideration for all practicing engineers. However,

they also work in an environment that encourages the freedom to develop alternatives to the given challenges [11]. Solar energy is a field full of potential and unexplored avenues, and students on the EVP teams are given a unique perspective on the issue and are motivated to design something new and different. These students are less likely to form to textbook solutions when exposed to similar challenges upon entering the workforce [4].

The EVP competition vehicles provide a creative outlet for engineering students. The peer-led environment provides a congenial and supportive network, while the projects themselves beg for clever and imaginative approaches. Solar technology provides a plethora of challenges in its capture and utilization, and when applied to its application in a vehicle it gives the students a foundation on which to focus their efforts. Creativity must be supported and cultivated among students of engineering, as they are not as restrained by conceptual barriers that may cloud the mind of an experienced engineer [4]. The future success of solar energy will no doubt be the product of a collection of unconventional "outside-the-box" ideas generated by a new generation of inventive engineers.

In the past, the EVP experience has not only provided a valuable way for MTSU students to gain essential hands-on experience but also had led to higher retention and graduation rates. In addition out of the multiple students that participate in EVP projects 95% receive highly desired jobs upon graduation both at the national and international level. As further testament to the fortitude of this program the Tennessee Board Regents awarded the program the academic excellence award in 2012.

4. Conclusions

The EVP projects provide a change in the traditional course structure of lecture, book problems, and exams while offering a great opportunity for inquiry and discovery. The inclusion of hands-on research projects on the freshman level has created interest, enthusiasm,

and self-motivation for STEM (science, technology, engineering, and mathematics) students. While the research projects require more time than traditional lecture course, the students walk away with a greater understanding of the material and a real-world experience of their chosen field of study. The on campus engineering laboratories help to facilitate the complete working experience for the students. The labs allow the students to design, create, and enhance their vehicles. In addition, these projects help students to sharpen their skills for future workmanship, such as team work, understanding responsibility, and making use of techniques learned in class. With prestigious awards won each year by each vehicle and its participating students, this distinguished research program will continue to provide an undergraduate learning experience with the latest advancements in technology. Moreover, the EVP students gain an invaluable experience and lifelong relationships while working with international partners.

References

[1]   S. Foroudastan, Mechanical engineering education: Not just about the math, in: IMECE International Mechanical Engineering Congress, Anaheim, CA, Nov. 13-19, 2004.

[2]   S. Foroudastan, R. Klapper, S. Hyde, Intercollegiate design competitions and Middle Tennessee State University's machine shop: Kindling engineering technology-student creativity & confidence, in: 2011 Annual Conference & Exposition, CA, 2011.

[3]   S. Foroudastan, Enhancing undergraduate education through innovative, applied research projects, in: ASEE 6th Global Colloquium on Engineering Education in Istanbul, Turkey, Oct. 1-4, 2007.

[4]   M. Holmes, Brain sports find a place in the sun, SWE Magazine 57 (3) (2011) 14-16.

[5]   Make solar energy economical, Grand Challenges for Engineering, http://www.engineeringchallenges.org/ cms/8996/9082.aspx (reviewed on May 2, 2011).

[6]   Welcome to Solar Splash, http://www.solarsplash.com/splash/spl_intro.html (reviewed on May 2, 2011).

[7]   U.S. News & World Report, http://grad-schools.usnews.rankingsand reviews.com/ best-graduate-schools/top-engineeringschools/rankings (retrieved Sept. 21, 2009).

[8]   The Case for a Name Change, A UMR White Paper, http://www.umr.edu/namechange (Nov. 10, 2006).

[9]   S. Foroudastan, Enhancing Undergraduate Performance through PL-TL (Peer-Led, Team-Learning), American Society for Engineering Education, 2009.

[10] S.C. Hockings, K.J. DeAngelis, R.F. Frey, Peer-led team learning in general chemistry: Implementation and evaluation, Journal of Chemical Education 85 (7) (2008) 990-996.

[11] V. Tinto, Promoting student retention through classroom practice, in: Enhancing Student Retention: Using International Policy and Practice, Amsterdam, Sept. 8, 2010.

Robotic Path Learning with Graphical User Interface

George Zhang[1], Jianjun Wang[1] and Jingguo Ge[2]

1. Corporate Research Center, ABB Inc., Windsor 06095, CT, USA

2. Robotics R & D, ABB Engineering (Shanghai) Ltd., Kangqiao, Shanghai 201319, PRC

Abstract: This paper describes an automated path generation method for industrial robots. Based on force control, a robotic subsystem has been developed for path automatic generation or path learning. Using a dummy tool and roughly taught guiding points around a part contour, the robot moves in position and force controlled hybrid mode, following the order of the guiding points and with contact force direction and value predefined. During the motion, robot actual position is recorded by the robot controller. After the motion, the recorded position data is used to generate a robot path program automatically. Robot lead-through may be used in the guiding point teaching. Furthermore, a GUI (graphical user interface) is developed on the teach pedant to guide through the guiding point creation and teaching, path learning, program verification and execution. The development has been incorporated into a robotic machining product option. Combination of the robot path learning function and GUI enhances the interaction between the robot and operator and drastically increases the level of robotic ease-of-use.

Key words: Robot, force control, path learning, user interface.

1. Introduction

Robot force control has been developed and used in assembly, machining and other applications where there is a contact between robot and objects which the robot is manipulating. With force control, robots gain touching "feeling"—one more step towards nature sense of human's. Refs. [1-6] described the force control development and applications conducted by ABB Robotics and its industry partners. At the beginning of the development, one of the goals was to use the force control feature to make the interaction between the human and robot easier in terms of robotic programming and teaching. Several related topics were investigated including lead-through teaching [7, 8], force control-based calibration and path generation [9].

This paper introduces and reviews an automated path generation method for industrial robotics. Based on force control, a method and system was developed for

robot path automatic generation or path learning. Using a dummy tool (real tool may be also used in some cases), guiding points are taught roughly around the part contour for which the robot path is generated. Then, the robot can be switched to its path learning mode; and following the order of guiding points taught, robot will move with a predefined contact force vale and direction along the contour of the part. During the motion, robot position is recorded and stored into variables in the robot controller. After the robot finished its motion, the recorded data is used to generate robot path program automatically. Technically, both 2-D and 3-D paths can be generated. Also robot lead-through may be used in the guiding point teaching. Furthermore, a GUI (graphical user interface) is developed on the teach pedant to guide through the guiding point creation and teaching, path learning, and program verification and execution. The development has been incorporated into a force control machining product. The combination of the robot path learning and GUI enhanced the interaction between robot and operator, improving the easiness of "programming" and reducing the time

Corresponding authors: George Zhang, Ph.D., senior principal scientist, research fields: robot kinematics and control, force control application, advanced manufacturing technology and process optimization. E-mail: george.q.zhang@us.abb.com.

needed to generate a precision robotic machining such as deburring, grinding and polishing program from weeks to hours.

Section 2 of this paper deals with the evolution of the robotic path learning concept. A real-world case of path learning on which the concept was formed is introduced and described. Algorithm used to realize the robotic path learning function has been developed; Section 3 briefly presents the implementation and application of the robot path learning technology; Section 4 of this paper deals with GUI for the robotic path learning feature. With carefully designing, the GUI has dramatically increased the level of easiness for robot force control setup, calibration, teaching and path learning, verification, as well as execution. An example of the impact of path learning with GUI to its end users is described and evaluated; Finally, Section 5 gives the summary and conclusions.

2. Path Learning Concept Development

As mentioned in the introduction, utilizing the touching feeling of robot force control in robot path automatic generation has been in consideration at initial stage of force control development at ABB. The first path learning lab experiment is done on a casting case of water pump. Fig. 1 gives the experiment set up. A dummy tool is used in the guiding point teaching and path learning along the gasket grove of the casting part. In this particular scenario, the edge of the grove will guide the tool through during the path learning; the force applied is in tool Z direction; robot is under force control in X and Y direction and position control in the orientation direction Rx, Ry and Rz. Robot lead-through is used for teaching the guiding points. To verify the accuracy of the path learned, an actual milling tool and a spindle was employed to cut the sealing gasket grove into final dimension.

With the successful demonstration of the complete process of guiding point teaching, path generation, and finally actual part cutting in the 2-D application, further development for 3-D path leaning and using path

curvature in path post processing were studied and developed. Ref. [10] gives the detail of the system configuration of the path learning and post processing. Fig. 2 shows the system configuration diagram.

A typical workflow of the system is shown in Fig. 3, which comprises: (1) determining the guiding points of the path on the part; (2) using robot lead through to teach the guiding points; (3) executing force feedback contour following with the robot based on the taught guiding points while continuously recording the TCP (tool center point) positions of the robot during movement; and finally (4) post processing the recorded position and generating the robot motion program. The benefit of this system is that the operator is only involved with the steps of determining and teaching the gross guiding points while the rest of work is automatically done by the robot controller.

The guiding points should cover any sharp turns on the contour of the workpiece. Typically, the guiding points are needed at corners and places of large curvature. If a specific application requires a big change of the tool position and/or orientation at certain places on the contour, these places should also be included in the guiding path. Since force control can enforce the contact, the guiding points are not required to be physically on the workpiece. However, it is generally required that the robot tool is in the same preferred orientation as in the actual application.

In order to realize the force controlled robotic path learning, a force/position hybrid control loop, robotic lead through teaching, contour following motion and position recording, as well as post processing are necessary and desired. Those feathers and functions are described respectively as below.

2.1 Hybrid Position/Force Control Loop

The hybrid position/force control is built on top of existing position control loop. Fig. 4 shows an explicit force control outer loop that closes around the existing joint PID position loop from most of industrial robot manufacturers.
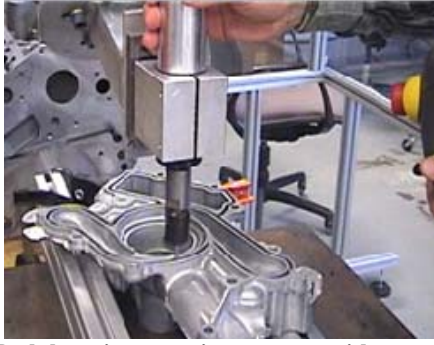
Fig. 1   Path learning experiment setup with a water pump casting.
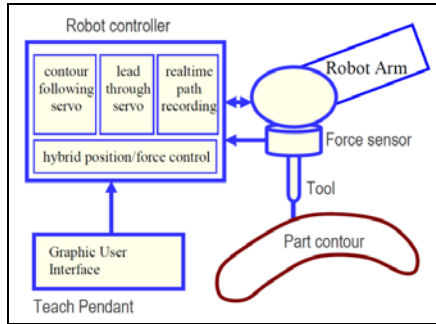
Fig. 2   System configuration for a force controlled robotic pathgeneration.
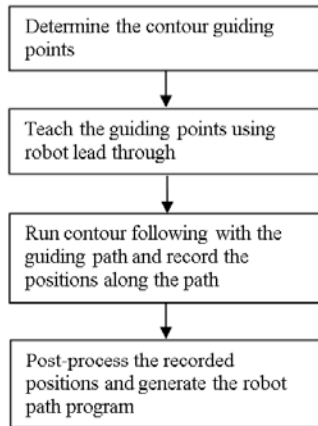
Fig. 3   Workflow of the proposed system.
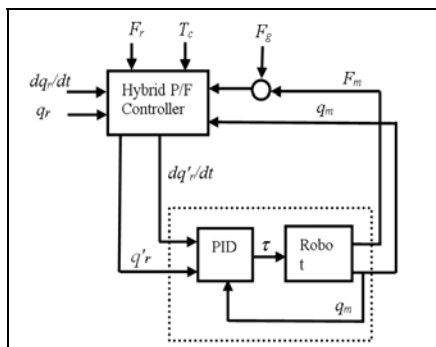
Fig. 4   Hybrid position/force loop built on top of existing PID loop.

Here q_r and dq_r/dt are the joint position and velocity reference, F_r the force reference, and T_c the task frame in which the force reference and force controlled directions are defined. q_m is the measured joint position, and F_m is the measured force in force sensor frame. F_g is the calculated gravity force of the force sensor payload. The hybrid position/force controller modifies the original joint references before forwarding them to the inner joint PID loop. The PID gains are also modified to improve the force control dynamic performance. A simplified explicit force control scheme is adopted (Fig. 5), where D is a constant and LP is a low pass filter.

2.2 Teach Guiding Path Using Lead-through Robot

It is not necessary but much easier to teach the guiding points by using lead-through robot. Because the lead-through servo puts the robot in a hybrid position/force mode, there is no need to worry about the collision of the tool with the workpiece since all contact forces will be well controlled. In addition, because the robot force control is performed in Cartesian coordinates, the lead-through robot is very intuitive since the operator never needs to think about the mapping between the jogging directions on the teach pedant and the actual robot moving direction in robot Cartesian frame. Testing revealed that changing orientation with the lead through is very difficult due to the couplings of the force and the torque and the difficulty of applying pure torque onto the robot tool. Recommendation is using the lead through teaching in translational directions while using (teach pedant) joystick jogging in rotational directions. In lead through mode, the task frame T_c is often taken as the
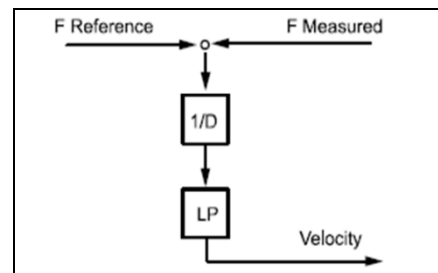
Fig. 5   A simplified force control scheme.

tool frame, and the joint references generated from the joystick are directly forwarded to the hybrid P/F controller.

The user is required to hold the teach pendant in lead through mode in order to comply with robot safety requirement. Lead through safety is further enhanced by adding force control specific supervisions. For instance, the TCP is not allowed to move beyond a specified distance from its original force-control enabling position and the speed limit is set to lower than the standard 250 mm/s position jogging safety limit.

2.3 Contour Following Servo

During contour following, the task frame T_c of the hybrid position/force control is chosen as the path frame. As shown in Fig. 6, a path frame is defined such that:

(1) The path frame *X* axis (Xp) is the tangent of the path along the traveling direction;

(2) The path frame *Y* axis (Yp) is calculated as the cross product of the tool frame *Z* axis (Zt) and the path frame *X* axis;

(3) The path frame *Z* axis (Zp) is calculated as the cross product of the path frame *X* and *Y* axes.

The tasks of the contour following servo are: (1) to determine the safe speed in executing the contour following; (2) to configure the force control loop as position controlled in the path tangential direction and force controlled in the path normal directions; and (3) to continuously generate and feed the position and force references as well as path frame to the force control loop. The inclusion of the path frame in the

trajectory references calls for an extended trajectory generator. Such a generator could be built on the existing trajectory generator of a position controlled robot with the addition of a path frame calculation module.

Fig. 7 illustrates a typical two stage trajectory generation process commonly found in commercial industrial robots. The demonstrated guiding path is a simple two line segment that starts from P_1 and ends with P_3 via a sharp corner point P_2. In the first stage of the trajectory generation, a macro interpolator divides in the Cartesian space the guiding path into short line segments (marked by macro points S1 to S11), each having the same traveling time. Kinematic and dynamic models are applied at each macro point to calculate the joint position, speed and acceleration references. In the second stage, a micro interpolator further divides each macro step into smaller time equal micro steps that are ready for the joint PID controller. As this stage is done in the joint space, no Cartesian information is available at the micro points q_1-q_3. As a result, the path frame is preferably calculated at the end of macro interpolation stage where the Cartesian information is available. The path frame at a micro point is then interpolated from the path frame data at the neighboring macro points. To avoid time delays, the calculation and the interpolation should always involve the past, present and future points. For instance, the path frame at point S_2 is calculated using points S_1, S_2 and S_3 Cartesian position data, while at point q_1, the path frame is calculated using the well-known sphere linear interpolation algorithm [11]:

$$\text{Slerp}(\Omega_1, \Omega_2; t) = \Omega_1 \left(\Omega_1^{-1} \Omega_2 \right)^t \qquad (1)$$

Fig. 6   Path frame definition.
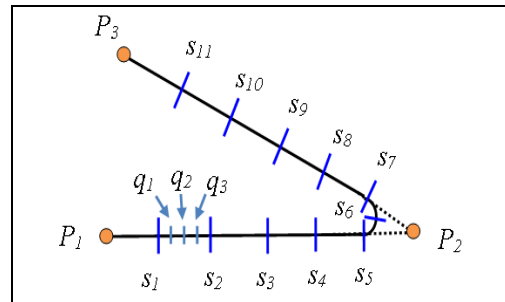
Fig. 7   Extended trajectory generation.

where, Ω_1 and Ω_2 are the quaternions of the path frames at macro point S_1 and S_2, and t is the interpolation parameter that equals 0.25, 0.5, 0.75 at point q_1, q_2 and q_3, respectively.

2.4 Real-Time Path Recording

While the robot with tool is moving along the workpiece contour, the actual robot target (position and orientation) is continuously recorded. To be able to capture the corners and the places of sharp curvature, the sampling rate has to be high enough with respect to the contour following speed. On the other hand, a fast sampling rate will create a huge amount of data to be stored in the robot controller memory. This would be a problem if the path was very long and the controller had limited memory. Ideally, fewer points would be saved for regions of a contour where the curvature changes slowly, while more points would be saved for regions of a contour where the curvature changes sharply. In this way, a more efficient program with less point data can be generated for production use. In the proposed system, a real-time line recovery module (to get rid of unnecessary intermediate points) is implemented for this goal. Due to the real-time nature of this module, a simplified line recovery algorithm is adopted. More sophisticated line recovery is decided to be left to the offline post processing.

The line recovery algorithm is simply the real-time merging of short line segments into longer ones based on a set of user-defined criteria. In this algorithm, a path point buffer is set up to receive the incoming path points from the real-time position recording function. Every time the position recording function pushes a new point (for instance point 14 in Fig. 7) into this buffer, the real-time line recovery module is activated to scan the buffer and try to merge shorter line segments into a longer one. As can be expected, during the contour following process the merged (P_{t_1} to P_{t_4}) and un-merged line segments (P_{t_4} to $P_{t_{14}}$) would coexist in the buffer. The line recovery module only deals with unmerged points (P_{t_5} to $P_{t_{14}}$). It checks if

two or more long line segments can be formed by those unmerged points according to a user-defined Path Accuracy Parameter. This is achieved by the following procedure. First, the system calculates the distance between each unmerged point (P_{t_5} to $P_{t_{14}}$) and the line connecting the last merged point (P_{t_4}) and the last unmerged point ($P_{t_{14}}$). Then, the system compares the calculated distances to the Path Accuracy Parameter. Merging occurs by deleting all the points between the last merged point and the first unmerged point whose distance is greater than the user specified parameter (P_{t_5} to $P_{t_{12}}$).

During post processing of the learned path, extra points are taken out for path cleanness and robot motion efficiency by avoiding two robot targets being too close together. Later the algorithm was implemented into the learning process. The extra points will not be recorded, which further improved the path generation process. Fig. 8 shows the system set up for the path learning and actual cutting test. And Fig. 9 illustrates the path post processing result.

3. Implementation and Applications

After the technology development, the algorithm and engineering knowledge were transferred and implemented into a robot product. Fixell, et al. [12] described the implementation process and result. Since then, force control robots have been increasingly used for laptop cover grinding and finishing, blade grinding, costing part pre-machining and various robotic material removal and finishing applications. Recently
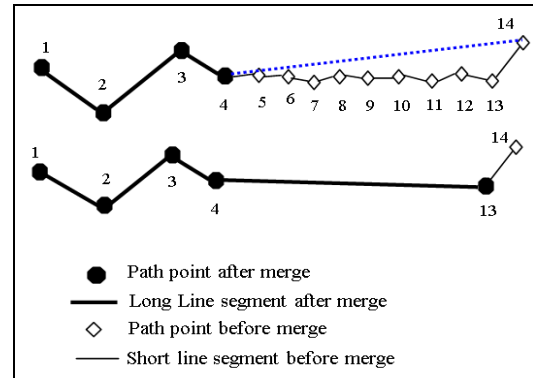
Fig. 8   Real-time line recovery.

Fig. 9   Pictures taken while the tool is in force control mode and programmed to follow the edge of a part.

(a)   (b)
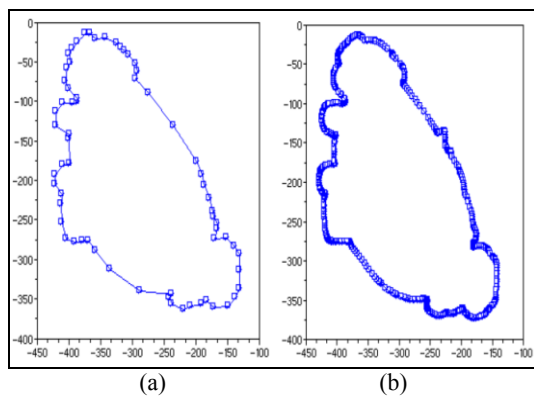
Fig. 10   post processed (a) and Learned path recorded (b).

low-cost force sensor development helped reducing the force control robot system cost and make robotic machining application more affordable. Standard robotic force control machining cell has also been built to reduce the complexity of using force control feature, which further helped customer acceptance of the robotic path learning feature. Recently, a successful demo to an aerospace company for a turbine blade paint removal application quickly built up the user's confidence in the robotic path learning technology.

As mentioned in the introduction, utilizing the touching feeling of robot force control in robot path automatic generation has been in consideration at initial stage of force control development at ABB. The first path learning lab experiment is done on a casting case of water pump. Fig. 1 gives the experiment set up. A dummy tool is used in the guiding point teaching and path learning along the gasket grove of the casting part.

In this particular scenario, the edge of the grove will guide the tool through during the path learning; the force applied is in tool Z direction; robot is under force control in X and Y direction and position control in the orientation direction Rx, Ry and Rz. Robot lead-through is used for teaching the guiding points. To verify the accuracy of the path learned, an actual milling tool and a spindle was employed to cut the sealing gasket grove into final dimension.

4. Graphical User Interface

GTU (graphical teach unit) is a relatively new feature of ABB industrial robots. It has a nice touch screen and a powerful on-board CPU. The touch screen makes the human robot interaction a lot easier. With the powerful CPU and API (application program interface) software library support, customized user interface can be easily created. At the last stage of the robot path learning development, a GUI was developed to guide the operator to perform the force control setup, path creation (through teaching or learning), program generation, testing, and execution. Ref. [13] describes the development of the GUI. As part of the FC machining package, path learning option can generate high accuracy path for machining applications such as milling, deburring, grinding and finishing applications. Robot lead-through feature can be enabled/disabled by simply pressing a button and easily used in the guiding points teaching. Robot targets can be displayed along with the machined surface on the GTU. Colored dots show different status of target points such as grey (untaught), blue (learned), and green (tested). In this way, user can easily visualize the location and the status of the target position. Fig. 10 gives the main page of the GUI of FC Machining package.

As a major portion of the FC machining package, path leaning process can be graphically guided through on the GTU. Using a grinding path generation as an example, entry points (position-controlled motion), guiding points (used in force-controlled motion for learning) and leaving points (position-controlled motion
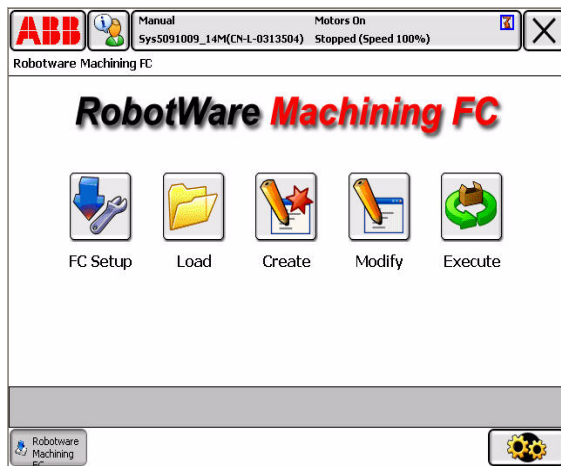
Fig. 10 **Main page of the FC machining package.**

Fig. 11 **A set of control points used in path learned.**
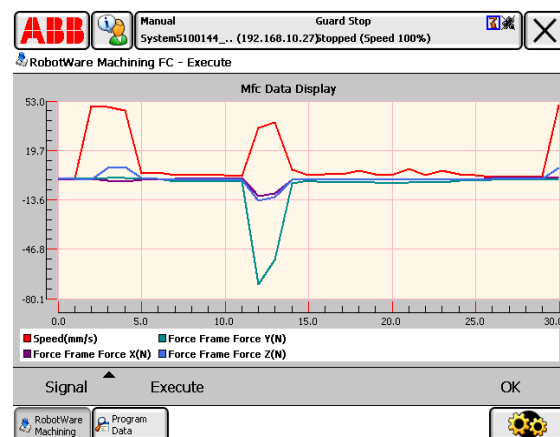
Fig. 12 **Display of the contacting force during force controlled motion.**

after leaning) are defined. While number of entry and leaving points are usually fixed, the number of guiding points used in learning can be various depending on the complexity of the part geometry and path accuracy required. Fig. 11 shows the graphically defined robot points on the GTU.

After the points are defined, the GUI can guide the user through target position teaching, testing, path leaning, verification and execution. The whole process can be done graphically without a single line of coding. The generated path can be also displayed on the GTU. Furthermore, during the testing, verification and execution process, contact force values can be plotted out on the GTU as well, which will help the user to understand the process and get better quality control. Fig. 12 shows a typical contact force plot.

This new way of robot "programming" can be greatly appreciated by customers across the industry from large enterprises to small and medium size manufacturers. A training/demo of this feature has been done recently at USCRC lab to a manufacturing company which is trying to use robot to automate its blade grinding process. Within two hours, two process engineers who have no experience with robot programming learned how to define, teach, learn, and verify the robot path and execute the robotic grinding program. The robotic blade gridding system was demonstrated on a major aerospace manufacturing automation show.

5. Summary and Conclusions

As described above, a force control based robot path learning function has been developed, implemented and marketed for ABB industrial robots. From basic concept creation, laboratory experiment, implementation and productization, the current result is a joint effort among different organizations. Feedback from our industrial partners and end users helped us a lot in understanding the manufacturing processes throughout the development and productization processes. In summary, it can be seen that:

(1) Force control gives industrial robot touch "feeling", which enhanced its capability to be used in contact type applications such as assembling and machining. Force control also provides a new way for human and robot interaction;

(2) Robot lead-through teaching and path learning have been researched at ABB. Lab experiments and functionality development have been conducted and the results have been productized into a standard product;

(3) Graphical user interface has been helped on the way towards ease-of-use for industrial robotics especially for robot path learning where human and robot interaction are needed. Properly designed GUI gives inexperienced users a quick starting point and reduced the fear of the complexity of robot programming;

(4) Force control-based robot learning with Graphical User Interface has been proven to be an example among many efforts to make human robot interaction easier and therefore will help with expanding the user base of industrial robot from automotive and other highly selected industries to general industry and small and medium size businesses.

References

[1] H. Zhang, Z.X. Gan, T. Brogard, J.J. Wang, M. Isaksson, Robotics technology in automotive powertrain assembly, ABB Review 13 (1) (2004) 13-16.

[2] G. Zhang, H. Zhang, H.P. Chen, J.J. Wang, T. Fuhlbrigge, D. Barrey et al., Automated engine piston installation using industrial robots, in: ICMA 2007, Harbin, China, Aug. 5-8, 2007.

[3] D. Gravel, G. Zhang, A. Bell, B. Zhang, Objective metric study for DOE-based parameter optimization in robotic torque converter assembly, in: International Conference on Intelligent Robots and Systems, St. Louis, MO, Oct. 11-15, 2009.

[4] J. Wang, G. Zhang, H. Zhang, T. Fuhlbrigge, Force control new technologies for new robotics applications, in: IEEE International Conference on Technologies for Practical Robot Applications, Woburn, MA, Nov. 10-11, 2008.

[5] ABB Robotics Application Manual, Force Control for Assembly, 3HAC025057-001_revD, 2007.

[6] ABB Robotics Application Manual, Force Control for Machining, 3HAC027595-001_revB, 2007.

[7] G. Zhang, Y.Q. Sun, J.J. Wang, Z.X. Gan, H. Zhang, G. Rossano, Accelerometer to monitor movement of a tool assembly attached to a robot end effector, US Patent, 20060178775 A1 (2006).

[8] S. Choi, W. Eakins, G. Rossano, T. Fuhlbrigge, Lead-through robot teaching, in: IEEE International Conference on Technologies for Practical Robotic Applications, Woburn, MA, Apr. 22-23, 2013.

[9] H. Zhang, T. Brogardh, J.J. Wang, G. Zhang, Z.X. Gan, Method of and apparatus for automated path learning, U.S. Patent, 2006093652 A2 (2006).

[10] J. Wang, H. Zhang, G. Zhang, A force control assisted robot path generation system, in: 4th IEEE on Automation Science and Engineering, Key Bridge Marriott, Washington DC, Aug. 23-26, 2008.

[11] K. Shoemaker, Animating rotation with quaternion curves, in: Int. Conf. on Computer Graphics and Interactive Technologies, 1985, pp. 245-254.

[12] P. Fixell, T. Groth, M. Isaksson, H. Zhang, J.J. Wang, J.M. He, et al., A touching movement—Force control turns machining robots into universal tools, ABB Review 4 (2007) 22-25.

[13] J. Ge, F. Tan, H. Zhang, Robotic Machining: A Force-Control-Based Fast Programming Method, in: IEEE Conference on Robotics, Automation and Mechatronics, Chengdu, China, 2008.

Adaptive Optimal Control of a Heavy Lathe Operation

Viktor D. Kovalev[1], Yana V. Vasilchenko[1] and Predrag Dašić[2]

1. Department of Machine Tools and Instruments, Mechanical Engineering Faculty, Donbass State Engineering Academy (DSEA), Kramatorsk 84300, Ukraine

2. SaTCIP Publisher Ltd., Vrnjačka Banja 36210, Serbia

Abstract: To create control laws of the cutting process on the heavy lathe, the temperature-force model of optimization of cutting conditions for turning was selected. The models to manage the process of cutting on heavy lathe in real time were created. It was found that the optimization of the cutting process must be carried out according to the criteria: productivity, cost and tool life. The hardware structure of the adaptive control system for heavy lathe was developed and its dynamic performance was investigated. The system provides function of the cutting speed of adaptive control and the possibility of compensation of linear, nonlinear and temperature-related inaccuracies. Research results were implemented in the prototype of adaptive control system for heavy lathe and the integral complex of optimal control of an adaptive technological system.

Key words: Heavy machine tool, cutting tools, power cutting, performance.

1. Introduction

The possibility of heavy machinery manufacturing, being competitive in the world market, is provided by the equipment of engineering enterprises by modern machinery. With the development of the industry, the requirements for machines increase, accuracy of their manufacture improvement, new brand materials are used, which provides the possibility of achieving a new level of performance. Technological processes of automated production should be provided with the equipment of a high class accuracy, as well as with high stability of functioning parameters.

Manufacture of heavy metallurgy, energy, transport of equipment is the basis of mechanical engineering of Ukraine and an important part of its exports. In the production structure of a heavy engineering enterprise, the larger part is the share of parts which are solids of

revolution for modern machines. These are rolls of rolling mills, rotor shafts of power plants, propellers of ships, etc.

In connection with a wide automation of engineering production, the task of determining the optimum modes of tool operation is of great importance. The equipment operation, the cost and accuracy processing, cutting tool capacity, the quality of the surface layer and other parameters of the metal working process depend largely on it. In industry, the cutting conditions are set in accordance with the regulations. However, the production conditions, as a rule, differ from the standard ones. Here there is an influence of the dynamic state of the machine, the fluctuations of properties between the parties of the product, the fluctuations of properties between the parties of the tool, etc., and to take them into account at the design stage of the technological process is not possible. The influence of a subjective factor turns out to be inevitable considering the real conditions. In the conditions of new materials processing, new materials, tools, with the new technological processes, i.e., when

---

Corresponding author: Viktor D. Kovalov, Ph.D., research fields: improvement of quality, exactness and functionality of machine tools, development of adaptive control systems of machine tools, development of hardening and coating technologies, development of progressive friction units, fluid friction supports and gears. E-mail: kovalov_viktor@mail.ru.

the normative data are not available or are not complete, the task is considerably complicated. In the existing literature, a large number of works are dedicated to the decision of optimization problems of the cutting process when turning on machines and FMC (flexible machining cells).

Their main methodological orientation is reduced to find the best combinations of the parameters, which determine the quality of processes in a most significant way. Most often, these parameters are the ones of technological processing mode: speed, depth of cutting and feed.

The existing methods and the systems of management and optimization of cutting modes are based either on the use of empirical indicators of the cutting process, which are obtained under certain conditions of the experiment not adequately reflecting the state of mechanical system or they require a large amount of material expenses and additional hardware at a relatively low effectiveness of regulation for their implementation. The loss of precision in the measurement of the cutting process indicators inevitably leads to economic losses. These losses are determined by the equipment and labour downtime, overtime work, violation of the production process continuity, the increased cutting tool wear, which negatively affects the quality of products, and may lead to penalties for failure to comply with contract obligations. The economic losses will inevitably increase the cost of products, and the inefficient use of equipment reduces its performance.

Aspiration to overcome these shortcomings led to the emergence of automated control systems, which allow optimizing the process of metal working thanks to the received current information on the parameters that determine the conditions and the quality of the cutting process. The task of such management systems, which are called adaptive [1, 2], is the change of the controlled parameters of the cutting process, which in the conditions of random disturbances would provide the extremum of the selected optimization criterion of

performance, cost, etc. And the change of parameters of the cutting process is carried out in real time environment [3], which is understood as the information processing mode, providing the interaction of information processing system with the external processes at a pace that corresponds to the speed of these processes. Cutting determines the pace of the interaction of information processing system with external processes, corresponding to the period of the cutting tool resistance.

2. Methods of the Adaptive Control of Cutting Process

The creation of the adaptive systems of automatic control of exactness is the most perspective way now. Principle of adaptability consists in the receipt of information about technological process parameters by means of aggregate of sensors, and subsequent application of this information for adequate interference with motion of technological process with the purpose of maintenance of values of certain product parameters within the limits of admittance. This direction has powerful theoretical support as a theory of automatic control and it applies to the questions of exactness which practically possesses unlimited possibilities. It became possible with appearance of the CNC (computer numerical control) systems and by virtue of development and reduction of prices of facilities of the electronic computing engineering, automation and measuring. Nowadays, the adaptive control appears as the most effective and economic way of exactness achievement. The question of rational choice of minimum necessary set of the guided parameters and diagnostic information generators is the unique substantial problem for this direction.

The increase of degree of equipment automation, especially due to numerical control, resulted in strong reduction of auxiliary, preparatory and final times. By comparison of basic times of treatment on an ordinary heavy lathe and heavy lathe with CNC exposed, it showed that basic time in percent correlation from the

total expenses of time approximately were twice as much than for a heavy lathe with a hand management (Fig. 1). Thus, skilled determination of the best values of technological parameters' treatment is required. The technological parameters of treatment method are determined by the set technological task and chosen technological facilities. Part of parameters of a heavy-lathe, clamping facilities and instrument set structurally (primary parameters), and part of parameters in the limited area can be chosen freely (adjusting parameters). The technological modes (cutting speed, serve and cutting depth) allow adapting the treatment method to the technological task. The optimum adaptive adjusting is based on the complete dynamic initial model of cutting process. Optimization is carried out during all of treatment process and guarantees the optimum conducting of cutting process. Permanent determination of instantaneous position of optimum working point in accordance with the instantaneous cutting process state is carried out with permanent comparison of actual values of parameters' characteristic sizes. Metal-cutting machine tools for the heavy cutting equipped the systems of optimum management on the base of machine-tools with CNC, present the high degree of automation and optimization of treatment process presently. At the development of the optimum adjusting system intercommunications are developed between statistical and continuous optimizations (Figs. 2 and 3). The dynamic model of cutting process lies in basis of the optimum adjusting. The values of criteria for the optimum adaptive adjusting present the extreme values of criteria of optimality of cutting process, proper the objective functions of statistical optimization. A kind and essence of time-changeable values in objective functions is set by the treated signals, characterizing the process of treatment.

The regulation of processing is that, depending on the availability of primary parameters to characterize the selected type of work-piece (material, size and stock, etc.) and adopted the method of processing

(a)

(b)
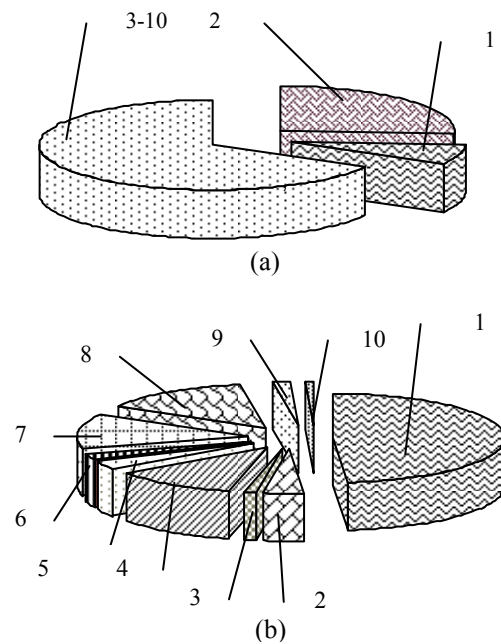
Fig. 1 Time of heavy lathe work. (a) ordinary lathe; (b) lathe with CNC. 1—basic time; 2—time of auxiliary motions; 3—outages because of a control system; 4—outages because of a machine-tool; 5—time of expectation; 6—service and care; 7—outages between operations; 8—preparatory-final time; 9—trial treatments; 10—demonstrations.
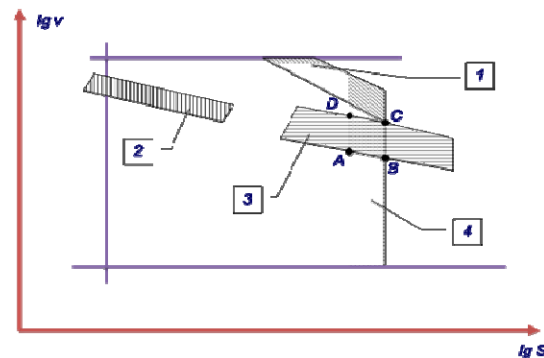
Fig. 2 The dynamic model of cutting process. 1—possible field for geometric constraints defined by the power; 2—possible geometric field dividing line value; 3—possible geometric field for tool life; 4—possible geometric field of cutting speed.

(machine, device, scheme cutting technological environment), changing the control parameters (cutting conditions, the option and the geometrical parameters of tool parameters and structure of the carrier system tools), to influence the control parameters (mechanics of cutting process, chip breaking, thermal phenomena, the strength and cutting power, vibration) and make the
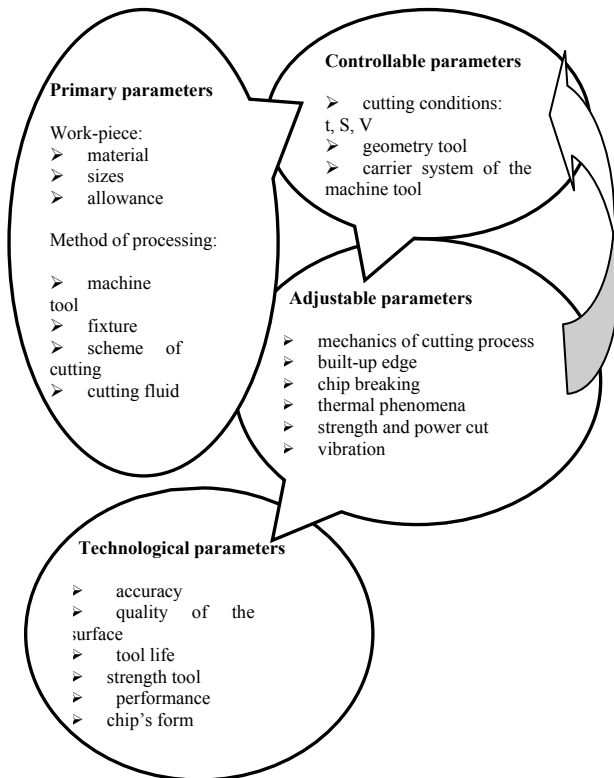
Fig. 3   Structure of adaptive control system.

necessary technological parameters (accuracy, surface quality, tool life, strength, tool, productivity, efficiency, the shape of chips) [4, 5].

Mathematical modelling and the choice of regression equation of processes and systems are given in Refs. [6-11], and mathematical modelling using the artificial neural network is given in Ref. [12].

3. The Creation of the Adaptive Systems of Automatic Control of Exactness

During automatic cycle of heavy equipment operation, the management tasks are multi-level and multiple-factor. In addition, there are situations, when there are no necessary sensors of primary information, or the existing means of measurement do not provide the required information in pace with the process, or there is only qualitative information on the object of control. In this case, the adaptive management of cutting processes should be built on the basis of multi-level decision-making system with the elements of artificial intelligence, which allows you to get the required information for control on the basis of

high-quality computer processing or misleading information on the object and the purpose of control. The studies are dedicated to the decision of tasks of the economically optimum cutting conditions directly in production process.

The system was designed to automatically maintain the set value of the cutting force in the longitudinal turning on heavy lathes with the purpose to obtain maximum processing performance excluding the overloads of the cutting tool that is being developed. This is a stabilizing system of automatic control of feed speed, consisting of the following components (Fig. 4): of chip loading sensor 1 of tension-metric type, of comparison device 2, of nominal chip loading device 3, of proportional or proportional-integral controller 4, of the electronic analogue of inertia element with a controlled time-constant 5, and of limiting device 6. The output of the last element is the control signal for longitudinal feed drive 7.

The system works as follows. Sensor 1 measures the current value of the cutting force, which is compared with the nominal value set for the selected tool. In case of deviation of the cutting force current value from the nominal one, which takes place due to a variety of factors (non-uniformity of allowance, non-uniformity of the material properties of the product, etc.), controller 4 adjusts the feed speed until the equality of the current and the given values of the cutting force is received in the steady state mode.
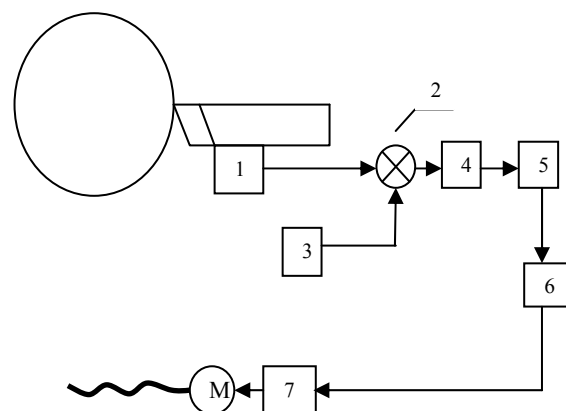
Fig. 4   Block diagram of the optimum control system of feed speed of cutting force.

Adaptive inertia element 5 is necessary to ensure the sustainability of the regulation system at different rotation speeds of the billet. From the point of view of the automatic control theory, the feed drive considering its feed speed is a typical inertia element, and the process of chip removal during one rotation of the billet depending on the cutting force and the feed speed can be represented by a more complicated structure, in addition, containing the element of pure delay of the signal in time. The series connection of the examined elements makes the system unstable and leads to self-oscillations of the feed speed. The stability of the system is ensured, when the time constant of feed drive is equal or bigger than the period of rotation of the billet. Additional inertia element 5 provides the equality of the different frequencies of a spindle rotation, at the same time ensuring maximum performance of the system.

For the stability analysis of the proposed system, as well as for the assessment of its performance, and the reaction to the rapidly changing perturbations a dynamic model of the simulation system in Matlab Simulink package was constructed (Fig. 5).

Fig. 6 shows the graphs of the transition process, describing the reaction of the established system to the rapidly changing disturbances. Quick change disturbance is a change of any of the input parameter of the system (in the pattern it is the value of the cutting depth) for a period of time, which is less than the time constant of feed drive, or change according to harmonious laws with a frequency bigger than the cut-off frequency of feed drive. Fig. 7 shows similar graphs in case of slow disturbances, i.e., disturbances of the signal with the frequency or speed of change, which falls in bandwidth of feed drive.

When modelling the following parameter values were applied:

- time constant of feed drive—3 s;
- the period of a spindle rotation—1 s (frequency of rotation is 60 rev/s);
- the form parameters of the cutting force—according to the case of turning cut of structural steel;
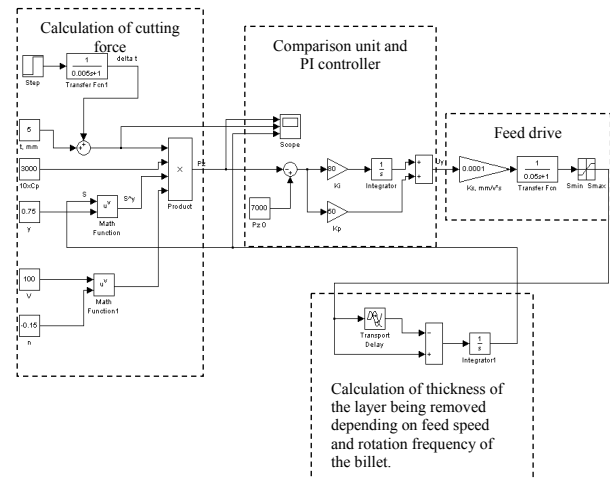
Fig. 5　Dynamic model of the system.
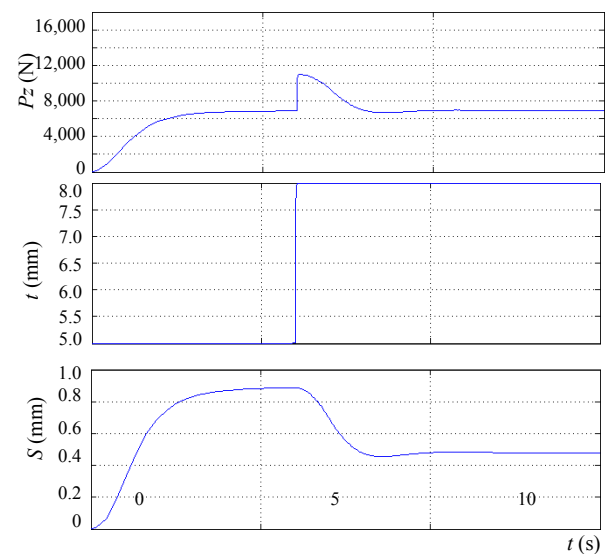
Fig. 6　Transition process in fast disturbance.
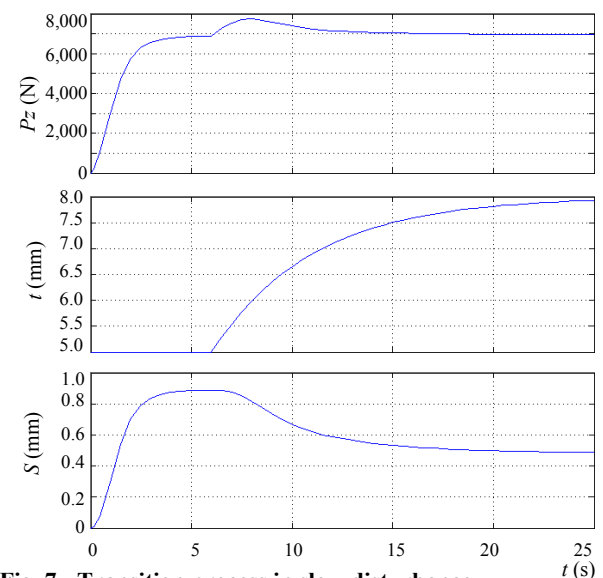
Fig. 7　Transition process in slow disturbance.

- the depth of cut before disturbance—5 mm;
- the depth of the cut after disturbance—8 mm.

In the first case, the change in the depth of the cut occurs with a time constant of 0.01 s, and in the second with a time constant of 5 s.

The graphs show that in case of slow disturbance, the degree of irregularity of cutting force is about 10% (in case of change of the cutting depth at 60%) and it decreases with a decrease in the speed of disturbance. With the rapid activation, the system is effective only after the transition process, and during the transition process, overloading of the tool is completely determined by the degree of disturbance.

Thus, the system can be considered efficient and effective on the rough treatment for velocities of disturbance entering the bandwidth of feed drive, i.e., when the time constant of feed drive is less than the one of the process of disturbance. Such disturbances include, for example, the fluctuations of the allowance in the longitudinal section of the billet.

The results of simulation of the developed system allow you to use it in feed drives of heavy lathes when roughing the parts of heavy industry.

In the same way, the algorithms of optimal systems of adaptive control including the criteria: processing cost, performance, accuracy, quality, reliability of the system, etc., can be developed.

The structure of the adaptive control system must have a high order of feedback covering: on the relative position and trajectories of forming movements of the system components, their physical conditions and disturbance impacts.

Optimal adaptive control is based on the full dynamic of the original model of the cutting process. Optimization is carried out during the entire processing and it guarantees the optimal cutting process. Continuous determination of the instantaneous position of the optimal operating point, in accordance with the instantaneous state of the cutting process, is carried out by means of constant comparison of actual values of the characteristic values of the parameters.

4. Conclusions

The processing on the heavy machine tools has its own peculiarities. To increase the efficiency of processing CNC machines, with operative optimization of the cutting process on the basis of artificial intelligence, it should be used.

For creating control laws of the cutting process on a heavy lathe temperature and force model of optimization of cutting conditions for turning was selected.

It was found that the optimization of the cutting process must be carried out according to the criteria: productivity, cost and tool life. Limitations are: the cutting possibilities of tool, electric main motion drive motor power, the strength of the feed mechanism, the stiffness of the tool and the work-piece, the kinematic capabilities of the machine.

The hardware structure of the adaptive control system for heavy lathe was developed and its dynamic performance was investigated.

Research results were implemented in the prototype of adaptive control system for heavy lathe and the integral complex of optimal control of an adaptive technological system.

References

[1] B.S. Balakshin, Use of adaptive control to improve the accuracy and efficiency of processing, Machines and Tools 4 (1972) 28-33.

[2] M.A. Mannan, S. Broms, B. Lindström, Monitoring and adaptive control of cutting process by means of motor power and current measurements, CIRP Annals—Manufacturing Technology 38 (1) (1989) 347-350.

[3] A. Patricia, S. Ralston, T.L. Ward, Mathematical models used for adaptive control of machine tools, Mathematical and Computer Modelling 11 (1988) 1151-1155.

[4] V. Kovalev, Y. Vasilchenko, A. Makarkina, Researches of chip breaking at new ways of deep drilling, in: Proceedings of the 7th International Conference "Research and Development in Mechanical Industry" (RaDMI-2007), Donji Milanovac, Serbia, 2007, pp. 202-208.

[5] V. Kovalev, Y. Vasilchenko, M. Melnik, etc., Trends of adaptive control of accuracy of the technological systems

on the basis of heavy machine-tools, in: Proceedings of the 2nd International Conference ICQME 2007, Budva Montenegro, 2007, pp. 263-275.

[6] P. Dašić, Analysis of wear cutting tools by complex power-exponential function for finishing turning of hardened steel 20CrMo5 by mixed ceramic tools, Fascicle VIII Tribology 12 (2006) 54-60.

[7] P. Dašić, Approximation of cutting tool wear function using polynomial regression equation, Journal of Research and Development in Mechanical Industry (JRaDMI) 3 (3) (2011) 171-180.

[8] P. Dašić, Comparative analysis of different regression models of the surface roughness in finishing turning of hardened steel with mixed ceramic cutting tools, Journal of Research and Development in Mechanical Industry (JRaDMI) 5 (2) (2013) 101-180.

[9] P. Dašić, The choice of regression equation in fields metalworking, in: Proceedings of the 3rd International Conference "Research and Development in Mechanical Industy" (RaDMI 2003), Vol. 1, Herceg Novi, Serbia and Montenegro, Sept. 2003, pp. 147-158.

[10] S.V. Kovalevskyy, V.I. Tulupov, P. Dašić, A.P. Nikolaenko, The Research of Electro-Impulse Turning Process, Scientific Monography, SaTCIP Publisher Ltd., Vrnjačka Banja, 2012.

[11] D. Milenković, P. Dašić, V. Nedeff, E. Moşnegutu, Analysis of regression models of maximal adsorption on high-porosity adsorbents with and without ultrasonic application, Revista de Chimie 60 (7) (2009) 706-710.

[12] V. Mereuta, P. Dašić, S. Ciortan, L. Palaghian, Assessment the influence of surface processing on fatigue damage using artificial neural network, Journal of Research and Development in Mechanical Industry (JRaDMI) 4 (1) (2012) 11-20.

A New Force Control Strategy Improving the Force Control Capabilities of Standard Industrial Robots

Markus Lotz, Hartmut Bruhm and Alexander Czinki

Robotics Lab, University of Applied Sciences, Aschaffenburg 63743, Germany

Abstract: In this paper, a new force control strategy (FineForce) is proposed, which is intended to improve the force control capability of standard industrial robots. The strategy distinguishes between joints with low and high (force control) bandwidth and tries to utilize the individual performance of the robot joints, such that improved results concerning force control can be achieved. The paper describes the FineForce control strategy as well as its laboratory implementation, based on a standard industrial robot. On the basis of experimental investigations, the performance of FineForce is demonstrated and compared to conventional force control strategies. Furthermore the usability of the new strategy in an industrial application is shown by a robot-based grinding process.

1. Introduction

Force control is an essential feature for industrial robotics on its way towards new and advanced applications. For example, human robot interaction, robot-based machining and assembly and the like all rely on force-sensitive manipulation capabilities.

For the force sensitive interaction between manipulator and environment the literature proposes, depending on the desired interaction behavior, several force control strategies like the hybrid force-/position control [1], the parallel force-/position control [2] or the impedance control [3]. Applied on standard industrial robots, these strategies offer the opportunity to operate the robot in force control mode. In contrast to soft robots [4] industrial robots usually only allow for limited force sensitivity. This results in awkward hand-guiding behavior; problems with the impact scenario (only limited impact velocities feasible) and offers only relatively slow force guided tracking velocities of unknown surfaces, necessary in many processes like grinding and the like. For the main part

---

Corresponding author: Markus Lotz, M. Eng., research fields: control of industrial robots, especially force feedback control for force sensitive machining applications. E-mail: markus.lotz@h-ab.de.

these limitations are caused by the mechanical characteristics and insufficiencies of standard industrial robots [5].

In this paper, a new force-feedback control strategy, named "FineForce" is proposed which is intended to partly overcome the before mentioned limitations of standard industrial robots in force-control applications. For controlling the desired force value, the FineForce strategy makes use of the inhomogeneity of joint dynamics that can be widely found in standard industrial robots. By assigning the high frequency portions to the robot axes with the highest dynamics, the mechanical part of the robot is utilized such that improved results concerning force control bandwidth and force sensitivity can be achieved.

The paper is structured into five major parts. Following this introduction, Section 2 introduces the general principle of FineForce; In Section 3, the benefits as well as the limitations of the FineForce control strategy—compared to conventional force control methods are pointed out; A transfer to an industrial force-sensitive grinding application is presented in Section 4 followed by the conclusions in Section 5.

2. General Principle of the FineForce Control Strategy

In order to improve the force control ability of standard industrial robots, FineForce splits the kinematical chain of a serial robot into two groups of joints. On the one hand there are the wrist axes which are operated in force control mode. And on the other hand there are the base axes which remain in position control mode and thus are only indirectly involved in the force control process.

The division is based on the fact that different robot axes usually provide different control bandwidths. The difference in bandwidth could be shown for position control [6] and also for force control [5] operation.

The FineForce strategy was applied to a specific industrial robot. Since the investigations showed a significant difference between the dynamics of the wrist and base axes, it's the robots axes were divided into the group of (relatively) fast wrist axes and the group of (relatively) slow base axis.

However, it is important to note that the general principle of the FineForce strategy is neither limited to a specific dispartment of the axes nor to a division into a specific number of groups.

Fig. 1 shows the control structure of the FineForce strategy as it was implemented for the test robot. The control structure can be split up into two major sections—each of them being allocated to one of the before mentioned joint groups. The green part regulates the wrist axes, whereas the yellow one actuates the base axes.

2.1 Direct Force Control by the Wrist Axes

The green part of Fig. 1 represents the closed loop force control system. This part of the control system regulates the desired contact force f_d only by using the wrist axes. For this purpose, a hybrid force-/position controller [1] is implemented. It allows force control along selected directions, whereas all directions orthogonal to the force controlled direction remain in position control.

Fig. 2 illustrates the resulting behavior of the force controlled wrist axes for two different cases. In both cases, the base axes are deactivated. The pictures on the left hand side in Fig. 2 show the systems behavior for the case that vertical direction is operated in force control mode while the horizontal direction is covered by the position control mode. Consequently, only external contact forces f_{ext} along the force-controlled vertical direction cause an evasive movement of the robot system. On the right hand side in Fig. 2, the situation is just the other way round: the force control is enabled in horizontal direction, whereas the vertical direction is covered by position control mode[2].
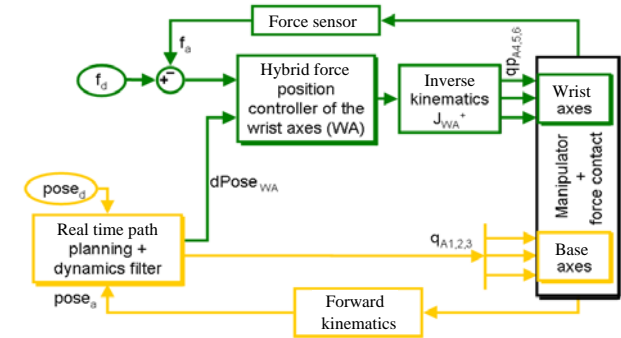
Fig. 1   Control structure of the FineForce strategy. The green part controls the WA (wrist axes) and the yellow part actuates the base axes.
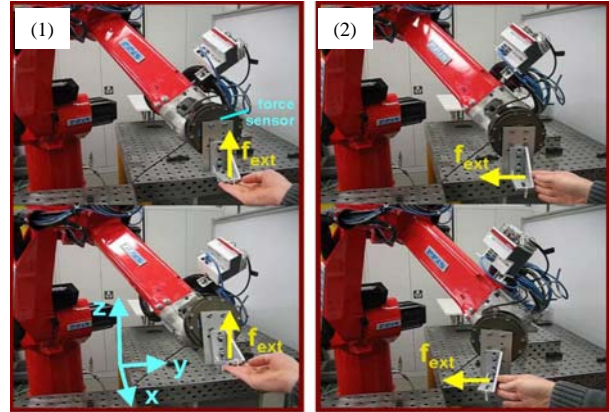
Fig. 2   Two examples for the hybrid force-/position controlled wrist axes: In example (1) the *z*-direction is operated in force control mode, whereas force control along axis y is activated in example (2).

---

[1]Of course, it is possible to select other directions for the force control, e.g. diagonal to y-z plane of the coordinate system. Also several directions can be force controlled at the same time, such as the horizontal and the vertical (refer to Section 3.3 for details).

It is important to note that the spherical wrist with its three joints is actually under-articulated and unable to generate deflections in one specific direction (as a reference: direction a in Fig. 3 cannot be force controlled). Thus a force related deflection of the TCP can only be generated along the two remaining cartesian directions b_{A4} and b_{A5} (also depicted in Fig. 3).

Because of the afore mentioned under-articulation, the pseudo inverse of the Jacobian J^+ [7] is being used in order to determine the inverse kinematics of the wrist joints. Thus a projection of the desired actuation vector onto the manipulability plane of the wrist axes is achieved. As a consequence of the under-articulated wrist, a position and orientation error of the tool occurs. As you can see in the pictures, the position error arises along the x-direction. And the orientation error appears around y for the left case example and around z for the right case, respectively.

2.2 Pose Error Compensation by Base Axes Deployment

For correcting the occurring position and orientation error, the yellow part of the control structure in Fig. 1 is used. The included real time path planning algorithm updates the desired joint position values of the base axes in order to compensate the pose errors of the position and orientation controlled directions (not along the force controlled direction).
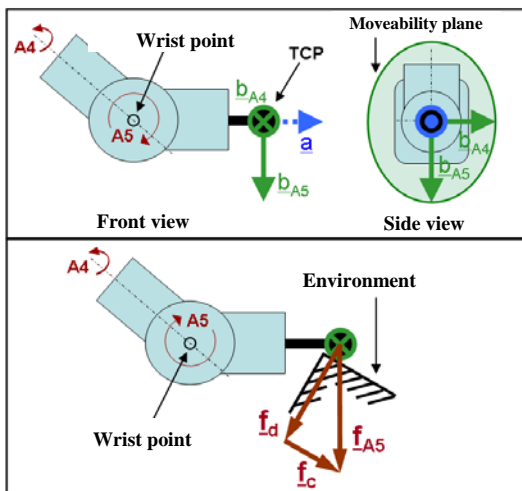
Fig. 3   Illustrates the under articulation of the wrist axes and the hereby resulting limitations of FineForce.

The calculated new joint variables are passed through a dynamics filter in order to adapt them to the dynamic constraints of the base joints. For this purpose a linear filter, e.g., FIR (finite impulse response) or IIR (infinite impulse response) can be used, or alternatively a non-linear filter can be deployed [8].

Remark: Because of the new joint values of the base axes, the wrist point[3] changes its orientation. Thus also the TCP position changes along with the new wrist point orientation. "dPose" in Fig. 1 represents the corresponding deviation which is regulated by the hybrid force-/position controller of the wrist axes.

2.3 Example for the Cooperation of Base and Wrist Axes

Fig. 4 illustrates the cooperation of the two parts of the FineForce control strategy. The figure shows a case in which a contact force along the z-axis is controlled. The figure is subdivided into three sections, each of them demonstrating a different phase of the FineForce strategy. Phase (a) shows the manipulator in its initial position. The force controller is deactivated and the robot is positioned at the desired tool pose ("pose$_d$") and applies no force against the spring. In phase (b), the force controller is activated and the desired contact force value f_d is adjusted. According to the green FineForce part (Fig. 1), the force is generated by a rotation of one or more of the wrist axes resulting in the desired force value, but also leading to a deviation in terms of the tool orientation and tool position (deviation in x- and around y-direction).
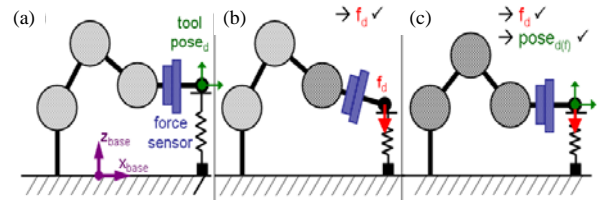
Fig. 4   Demonstration of the cooperation of the base- and wrist joints. Phase (a) shows the initial situation with the desired pose posed; In phase (b), the desired force f_d is regulated by the wrist joints; In phase (c), the resulting pose error is compensated by the base joints.

---

[2]Wrist point: the point where all axes of the wrist joints intersect.

For the compensation of these errors, the second part of FineForce is responsible (phase (c)). With the help of the inverse kinematics, new joint values are calculated which realize the desired pose for the given external force load ($pose_{d(f)}$) .

In reality, the cooperation is in contrast to the schematic presentation in Fig. 4a smooth process with both parts of the FineForce-control structure being executed simultaneously. As soon as FineForce generates the force generating motion of the wrist axes, it also initiates a motion of the base axis. The movement of the base axes is qualified to compensate the orientation error resulting from the force-generation movement of the wrist axes. Thus the compensation motion starts, as soon as a pose error arises. However, due to the slower dynamics of the base axes, the orientation errors are not compensated as fast as they are produced by the comparatively fast wrist axes.

3. Evaluation of the FineForce Control Strategy

In this section, the FineForce strategy is compared to a CFC (conventional force control) strategy. Based on experimental tests with a standard industrial robot, investigations were conducted in order to work out the specific benefits and limitations of FineForce.

In contrast to the FineForce strategy, CFC employs all six robot joints for the force control process. In this case the hybrid force/position controller actuates not only the wrist axes (as this is the case using the FineForce strategy) but also the base axes of the robot.

3.1 Experimental Setup

For the experiments, an industrial robot of the robot manufacturer Reis Robotics (type RV6L shown in Fig. 2) is being used. It is equipped with a compliant six degrees of freedom force sensor (Schunk FTACL 50-40).

The force control strategies are implemented on an external controller, which is part of a rapid control prototyping system (dSPACE DS 1005). By the use of a specifically designed CAN interface, the external controller is able to transmit the actuating variables, calculated by the force feedback controller, directly to the drive units of the robot. The direct access to the drive units allowed for a cycle time of only 1.5 m/s in combination with a very small dead time (Fig. 5).

In both cases, the FineForce and the CFC strategy, the outer force control loop is closed around an inner velocity control loop operating in joint space. This is well suited for industrial robots because no model-based control as in Ref. [7] is needed. For the force- and pose- controller of the hybrid controller a classical PI controller (in case of hand-guiding a P controller) turned out to be sufficient for the task.

3.2 Comparison/Benefits of FineForce

In general, the FineForce strategy offers higher force sensitivity and a higher force control bandwidth than the conventional force control strategy. This leads to a better force sensitive hand-guiding, a faster force sensitive tracking of unknown surfaces and it also allows for a higher approach velocity towards unknown surfaces. In the following sections, all these advantages will be proven based on experimental results.

3.2.1 Force Sensitivity

The force sensitivity can be measured with the experiment shown in Fig. 6. The robot is in force control mode and a force set point of zero is adjusted. Upon application of an external contact force along the horizontal direction (illustrated by the yellow force meter), the robot reacts with an evasive motion of the TCP along the same direction. The higher the evasive motion velocity, the higher the force sensitivity.

Fig. 7 shows the corresponding force and velocity values. In case of FineForce, a force sensitivity of 16.66 mm/s/N could be achieved. This is about 4.5 times higher than the sensitivity that was possible by using the CFC strategy (which allowed force sensitivity values of up to 3.66 mm/s/N only).
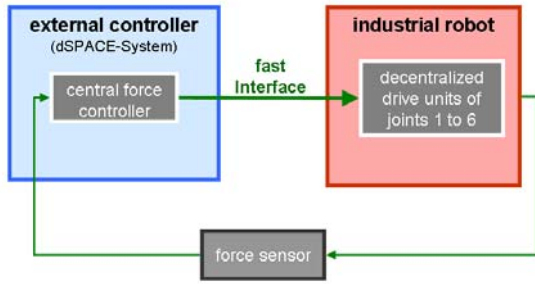
Fig. 5 Controller setup consisting of a force controller located on an external controller with fast and direct access to the drive units of the robot joints.
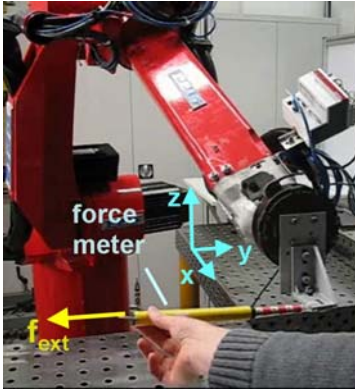
Fig. 6 Experimental setup for measuring the force sensitivity.

3.2.2 Force Control Bandwidth

In contrast to the previous criterion where the disturbance reaction of the control loop was analysed, this section evaluates the force control performance from the view of reference action on the control loop. Fig. 8 compares the step response for the FineForce strategy with the CFC strategy. Investigations in the frequency domain showed that FineForce allowed for a control bandwidth of 5 Hz whereas the CFC achieved only 2.5 Hz.

3.2.3 Force Sensitive Tracking of Unknown Surfaces

In this section, additional investigations concerning the force control performance are presented. The robots task in the experiments presented is to control the contact force along the z-direction while moving over a sine-shaped contour (Fig. 9).

Fig. 10 shows a plot of the actual force value during the sinus-contour test. The test was performed at a TCP motion speed of 6 mm/s and was conducted with the CFC strategy, and for comparison also with the
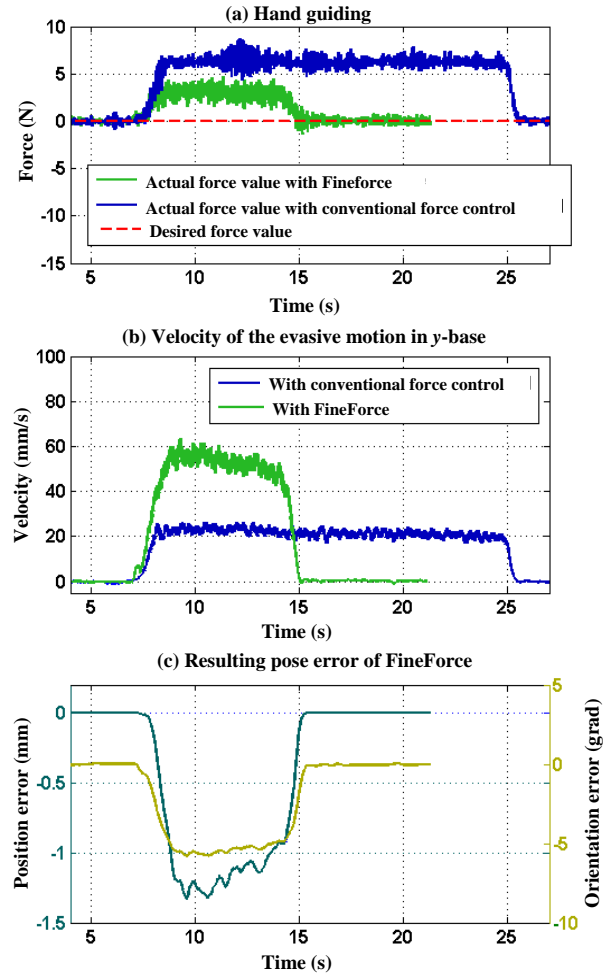
Fig. 7 Comparison of FineForce and the CFC concerning the force sensitivity. (a) shows the external force f_{ext} and (b) the resulting velocity of the evasive motion; (c) displays the resulting positioning error along x and the resulting orientation error around z axis while FineForce strategy was applied (refer to Section 3.3 for more details).
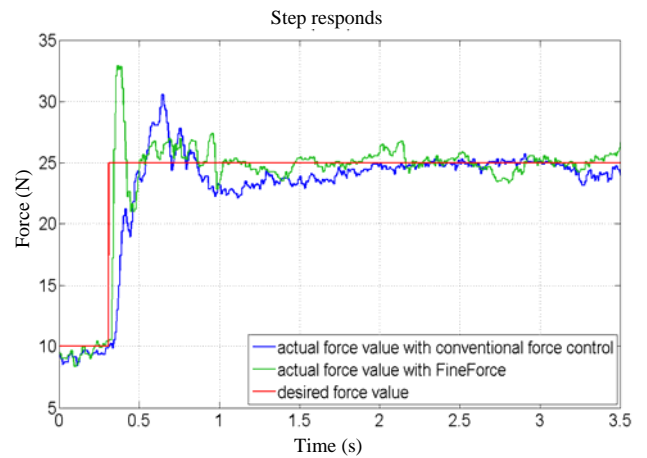
Fig. 8 Comparison of the step response of FineForce and the CFC.
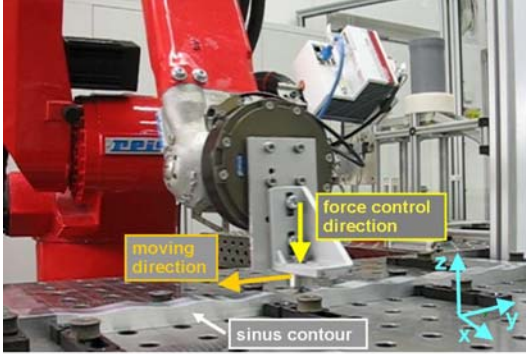
Fig. 9   Force sensitive contour tracking of sinus contour.
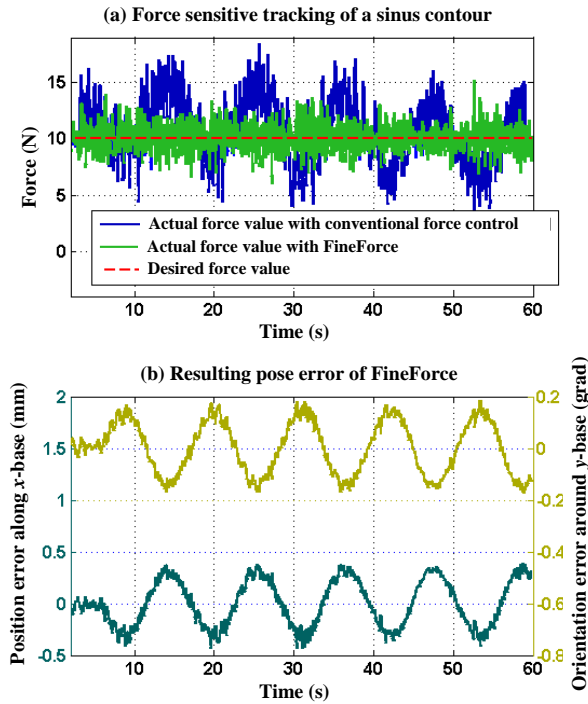
Fig. 10   (a) Comparison of the actual force value of the FineForce strategy with the CFC in case of force sensitive tracking of a sinus contour; (b) shows the resulting pose error of the FineForce strategy (discussed in the Section 3.3 in more detail).

FineForce strategy. With the CFC strategy a significant control deviation occurred (about ±6 N). The very same deviation occurred only at a significantly higher velocity of over 15 mm/s with the FineForce strategy applied. By the use of the FineMove strategy, the moving velocity could be increased by a factor of 2.5 compared to a CFC strategy without having any disadvantages concerning the force control accuracy.

3.2.4 Impact Scenario

The impact scenario describes the transition from

free space conditions into contact conditions with a more or less rigid environment. In the test setup shown in Fig. 11, the rigid environment is represented by a solid metal table. Again a comparison between the conventional and the FineForce strategy was conducted. For both strategies the same conditions were applied (this includes the conditions for switching from position- into the force-control mode). The transition between position and force control was trigged when the measured force reached a value of 5 N. Fig. 12 shows the corresponding experimental results. At an impact velocity of 24 mm/s the force peak could be significantly reduced by using the FineForce strategy instead of the CFC strategy.

3.3 Limitations and Opportunities of FineForce

The achieved benefits of FineForce are accounted by some disadvantages, which will be discussed below. In general these disadvantages result from the under-articulated wrist axes and can be summarized with the following three statements:

(1) The occurring pose error caused by the force controlled wrist axes can be compensated by the real time path planning. But due to the limitations concerning the dynamics of the base axes, the compensating motion can only take place with some time delay. So small deviations from the desired pose remain in the dynamic state, not in the static state (Figs 7 and 12; Fig. 10 does not plot the static state). The pose error consists of a position error along a (Fig. 3) and an orientation error. The direction of the orientation error depends on the force controlled direction f_d and can be described as the vector product of f_d and a;

(2) Because of the under-articulated wrist axes, force control is only possible along two degrees of freedom, as sketched on the left hand side in Fig. 3. In the sketched configuration, joint five offers a moveability along the vector b_{A5} and joint four along b_{A4}. However, the hand axes are not able to generate a movement along the vector a;
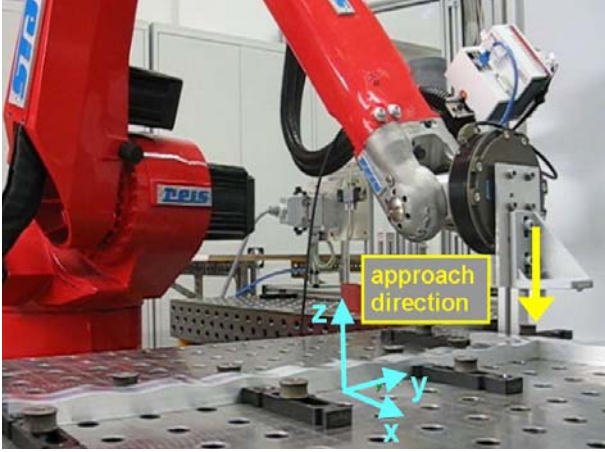
Fig. 11   Illustration of the impact scenario: The force control mode is activated until the table is touched.
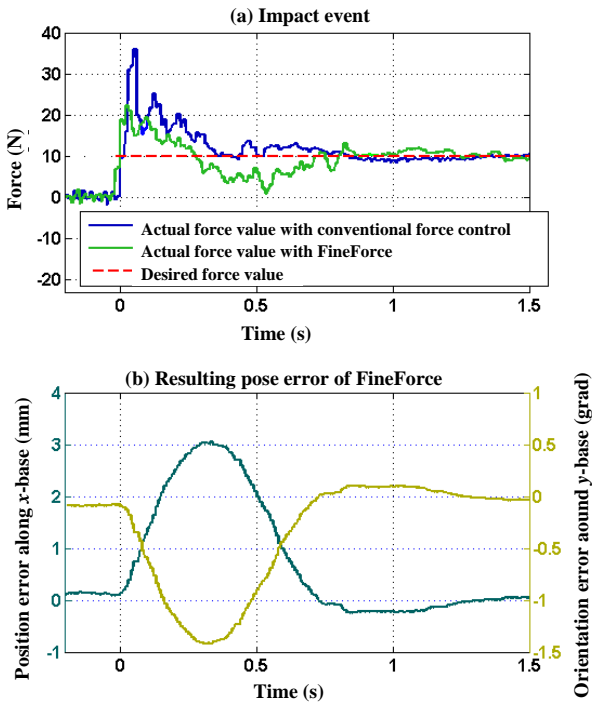
Fig. 12   The upper plot compares the FineForce strategy and the CFC during the impact scenario. The lower plot shows the resulting pose error of the FineForce strategy (see Section 3.3 for details).

(3) Force control along directions, which are not within the moveability plane (spanned by the velocity vectors b_{A4} and b_{A5}) and which are not aligned with the missing degree of freedom (vector a), are generally possible but provide a specific disadvantage: For producing a force f_d which is not aligned within the moveability plane (illustrated on the lower part of Fig. 3), a cross force f_c may arise.

4. Industrial Application: Force Sensitive Grinding

Robot-based grinding is an important application with high economic potential and a well suited example where force control is needed. Classical position controlled industrial robots are usually not qualified to perform this type of tasks. Because of workpiece tolerances and tool wear, fixed programmed tool feeds can results either in too high process forces (risk of quality deterioration or even damages) or too low process forces (risk of lost cycle time).

Taking these considerations into account, the exact adjustment of contact forces in grinding can be regarded as both, essential and challenging at the same time. Thus robot based grinding represents a very well-suited example for application cases where reliable and sensitive force control is needed.

In the section below, the results from the authors investigations concerning the usability of FineForce for industrial robot-based grinding applications are presented. It will be shown that the limitations coming along with the FineForce strategy mentioned before, only have minimal impact on standard industrial grinding process. Basis for the investigations on the usability of the FineForce strategy to industrial applications was the experimental setup shown in Fig. 13a. A standard industrial robot was equipped with a grinding tool. This test setup was used in order to remove a welding seam on the surface of a workpiece.

Below, the effects of the limitations of the FineForce strategy (Section 3.3) in context with the above mentioned grinding application will be discussed:

First of all, the remaining pose error in the dynamic state turned out to be very small. The pose error had no noteworthy effect on the grinding quality. The welding seam was smoothly grinded, as can be seen in the comparision between the workpiece before and after the grinding operation (Fig. 13);

Secondly, the missing degree of freedom (depicted by the blue arrow in Fig. 13) did not cause any limitations to the investigated grinding process, since

(a)

(b)
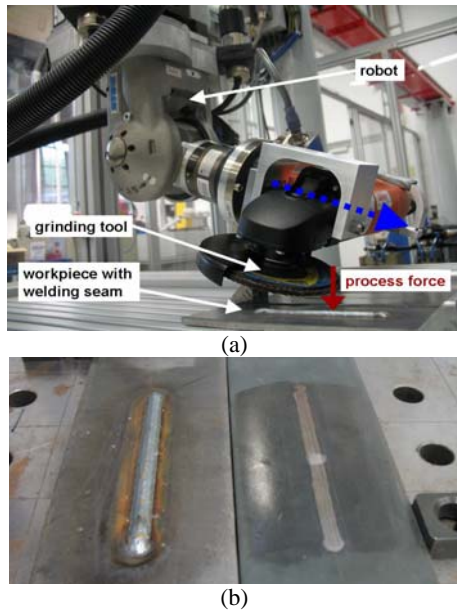
Fig. 13   (a) Standard industrial robot equipped with a grinding tool; (b) The left side shows the workpiece before and the right side after the grinding process.

the setup was designed such that the normal force (red arrow in Fig. 13) could easily be generated and controlled by the remaining degrees of freedom;

And thirdly, noticeable cross forces f_c did not occur. This is generally true for standard grinding applications, because the rotating grinding disc already exhausts the maximum friction angle between workpiece and tool. As a consequence, no additional (cross-) forces can be transmitted within the workpiece-tool contact area.

5. Summary and Outlook

In this paper, a new force control strategy, called FineForce, was presented. It was developed to improve the force control capability of standard industrial robots.

By conducting extensive experimental investigations, the benefits of the FineForce control strategy in contrast to conventional force control could be proved. The results document that FineForce achieves a significantly higher control bandwith and force sensitivitiy than conventional force control strategies.

However, the introduced FineForce strategy also causes, by principle, minor disadvantages such as small pose errors that occur in the dynamic state and a limitation to 2-dimenisional force control.

However, by the investigation of a robot-based grinding process operated with FineForce, it could be demonstrated that the disadvantages will usually only have minor or even no negative impact on standard grinding applications.

References

[1]   M.H. Raibert, J.J. Craig, Hybrid position/force control of manipulators, Journal of Dynamic System, Measurement, and Control 103 (2) (1981) 126-133.

[2]   S. Chiaverini, L. Sciavicco, The parallel approach to force/position control of robotics manipulators, IEEE Trans. Robot. Automat. 9 (1993) 361-373.

[3]   N. Hogan, Impedance control, an approach to manipulation: Part I, II, III, Journal of Dynamic Systems, Measurement and Control 107 (1985) 1-24.

[4]   A. Albu-Schäffer, S. Haddadin, Ch. Ott, A. Stemmer, T. Wimböck, G. Hirzinger, et al., The DLR lightweight robot: Design and control concepts for robots in human environments, Industrial Robot: An International Journal 34 (5) (2007) 376-385.

[5]   M. Lotz, M. Pfeffermann, H. Bruhm, A. Czinki, Quantitative analysis of the force control capability of standard industrial robot axes, in: The 9th France-Japan Congress & the 7th Europe-Asia Congress and the 13th International Workshop on Research and Education in Mechatronics, Paris, Nov. 21-23, 2012.

[6]   H. Bruhm, A. Czinki, M. Lotz, V. Wenzel, A motion control strategy for robots in laser material processing and other high speed applications, in: The Joint Conference of the 41st International Symposium on Robotics (ISR 2010) and the 6th German Conference on Robotics (ROBOTIK 2010), Munich, Germany, June 7-9, 2010.

[7]   L. Sciavicco, B. Siciliano, Modelling and Control of Robot Manipulators, 2nd ed., Springer, New York, 2001.

[8]   L. Biagiotti, R. Zanasi, Open-loop and closed-loop filters for optimal trajectory planning under time and frequency constraints, in: Workshop on Robot Motion Planning: Online, Reactive, and in Real-time 2012 IEEE/RSJ International Conference on Intelligent Robots and Systems, IROS 2012, Vilamoura, Algarve, Portugal, Oct. 7-12, 2012.

A Metapopulation Model with Patches Distributed in Two Geographical Scales

Vanderlei Manica and Jacques Aveline Loureiro da Silva

Department of Pure and Applied Mathematics, UFRGS, Porto Alegre 91509-900, Brasil

Abstract: We propose a metapopulation model with two geographical scales. In a regional scale, the model describes the dynamics of a collection of habitats connected by migratory movements. In a local scale, we consider some granularity within each habitat, in the sense that each habitat is itself a collection of patches linked by dispersal. The whole ensemble can be seen as a metapopulation composed by local metapopulations. We analyze the synchronization of the model in the two geographical scales. We present an analytic criterion for synchronization where only the habitats in the regional scale evolve with the same dynamics. Through numerical simulations, we discuss the different synchronization modes. It depends on how the individuals are distributed in the local patches that compose a habitat after migration takes place in the regional scale.

Key words: Metapopulation, distribution matrix, Lyapunov number.

1. Introduction

A metapopulation is composed of populations spatially distributed in fragments called patches and connected by dispersal process [1]. A phenomenon related to the dispersal process is the synchronized dynamics where the population densities in all patches evolve with the same amplitude. Its importance lie in the fact that a local population can be recolonized if the whole system is not synchronized [2].

Systems of discrete equations are often used to model metapopulations [3-5]. A model with patches linked by migration and subjected to external perturbations was considered in Ref. [3]. The model is a discrete-time system composed by single specie where a constant fraction disperses per generation. Through numerical simulations, it was shown that chaos can prevent global extinctions when coupling is weak. Ref. [4] was obtained an analytical result for the stability of synchronized trajectories in a model with

an arbitrary number of patches linked by dispersal. A special case of density-dependent dispersal was analyzed in Ref. [5] and it was concluded that this mechanism reduces the stability regions of the synchronous dynamics.

In this paper, we propose a metapopulation model with patches distributed in two scales. In a regional scale, the model is composed of habitats connected by dispersal process. In a local scale, we assume some granularity within each habitat in the sense that each habitat is itself a collection of patches and individuals migrate among the patches and the habitats.

The paper is organized as follows: Section 2 introduces the metapopulation model; Section 3 analyzes the asymptotic local stability of synchronized trajectories and obtain an analytical criterion based on the calculation of the transversal Lyapunov numbers; Section 4 describes our numerical simulations and discussion is done in Section 5.

2. Metapopulation Model

Our metapopulation model is composed by patches

Corresponding author: Vanderlei Manica, Ph.D., research fields: systems dynamics and simulation. E-mail: vanderlei.manica@ufrgs.br.

distributed in two geographical scales. In a regional scale, the basic unit is a habitat. In a local scale, the basic unit is a patch and individuals migrate among the patches and the habitats.

2.1 Metapopulation Model in a Local Scale

We start describing the dynamics in a local scale, i.e., the dynamics within the habitat. In this case, the metapopulation will be a collection of patches linked by dispersal as in Refs. [3-5]. Assume that the habitat is composed by d patches and the local patch dynamics is described by a smooth map f on $[0, \infty)$. In the absence of dispersal between patches, the time evolution of the population is given by:

$$x_{t+1} = f(x_t) \qquad (1)$$

where, x_t represents the number of individuals at time t.

After the local dynamics given in Eq. (1), individuals migrate between the patches. Let m be the fraction of individuals that leave patch i, $i = 1, 2, \ldots, d$. Thus, the density of individuals that leave patch i at time step t is given by $mf(x_t^i)$. Moreover, from individuals that disperse from the neighboring patches k, a fraction γ_{ik} reach patch i. Assumption on the conservation during dispersal and assuming that individuals do not return to the same patch, we have $\sum_{k=1}^{d} \gamma_{ki} = 1$ and $\gamma_{ii} = 0$, $i = 1, 2, \ldots, d$. Taking these into consideration, we can write the equations describing the dynamics of the isolated habitat as:

$$x_{t+1}^i = (1-m)f(x_t^i) + \sum_{k=1}^{d} \gamma_{ik} mf(x_t^k) \qquad (2)$$

The first term in the right hand side of the above equation represents the individuals that did not leave patch i at time t, while the second one is the sum of all contributions of neighboring patches.

2.2 Metapopulation Model in Two Scales

The model in two geographical scales consists of n equal habitats, labeled as 1, 2, …, n, each one containing d equal patches. The total number of patches in the whole network is nd.

Let x_t^{ji} the number of individuals in patch i of

habitat j at time t. Let $z_t^j = (x_t^{j1}, x_t^{j2}, \ldots, x_t^{jd})$ the d-dimensional vector representing the distribution of individuals among the patches of habitat j. In the absence of dispersal between the habitats, the habitat local dynamics, represented by $F : R^d \to R^d$, is given by:

$$F(z_t^j) = \begin{pmatrix} (1-m)f(x_t^{j1}) + \sum_{k=1}^{d} \gamma_{1k} mf(x_t^{jk}) \\ (1-m)f(x_t^{j2}) + \sum_{k=1}^{d} \gamma_{2k} mf(x_t^{jk}) \\ \vdots \\ (1-m)f(x_t^{jd}) + \sum_{k=1}^{d} \gamma_{dk} mf(x_t^{jk}) \end{pmatrix} \qquad (3)$$

After the habitat local dynamics, we assume that individuals migrate among the habitats. Let μ be the fraction of individuals that leave habitat j. The density of individuals that leave habitat j at time t is $\mu F(z_t^j)$, $j = 1, 2, \ldots, n$. From these individuals, only a fraction will move to habitat j. This process is governed by a nonnegative $n \times n$ matrix $C = [c_{jl}]_{j,l=1}^n$ satisfying $c_{jj} = 0$ and $\sum_{l=1}^{n} c_{lj} = 1$, $j = 1, 2, \ldots, n$. Thus, the number of individuals that leave patch i of habitat l and reach habitat j at time t is $\mu c_{jl} F(z_t^j)$. Due to the habitat subdivision in patches, we assume a new migration process where individuals that reach the neighboring habitat may choose some patches with different probabilities. For example, individuals can migrate to the neighboring habitat and have a preference to move to certain patches, or individuals can choose the local patches in the neighboring habitat with the same probability. In order to take this consideration into account, we define a patch interaction coefficient by w_{ik}, $0 \leq w_{ik} \leq 1$ (Fig. 1).

Thus, we can write the system of equations describing the dynamics of the model with patches distributed in two geographical scales as:

$$z_{t+1}^j = (1-\mu)F(z_t^j) + \sum_{l=1}^{n} \mu c_{jl} WF(z_t^l) \qquad (4)$$

where, $W = [w_{ik}]_{i,k=1}^d$.

The matrix W is called as distribution matrix and tells us how the migrants in the departure habitat are
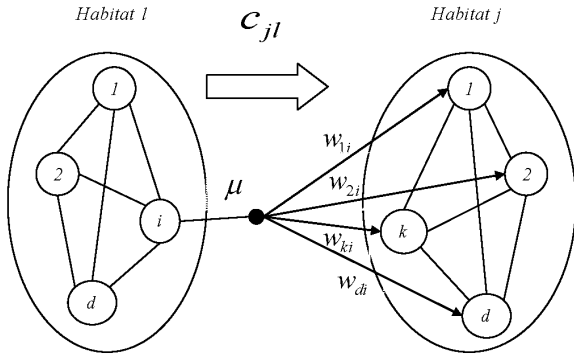
Fig. 1 Distribution of individuals between habitats. A fraction of individuals migrate from patch *i* of habitat *l*. From these individuals, a fraction c_{jl} reach a neighboring habitat *j* and establish in the patches with proportions w_{ik}, *i*, *k* = 1, 2, …, *d* and *j*, *l* = 1, 2, …, *n*. The fraction of individuals that leave patch *i* in habitat *l* and establish in patch *k* of habitat *j* is $\mu c_{jl} w_{ki}$.

distributed as well as how they distribute in the destination habitat. For example, if individuals distribute uniformly in all *d* patches of the destination habitat, we have a uniform distribution and all the entries of *W* are equal $1/d$.

In the following, we linearize the system in Eq. (4) around the synchronized trajectories and obtain a stability criterion based on the computation of the transversal Lyapunov numbers of attractors on the synchronous invariant manifold.

The synchronized state is achieved if the density of all habitats is the same, that is $z_t^j = z_t^s$, where, $z_t^s = (x_t^1, x_t^2, ..., x_t^d)$, *j* = 1, 2, …, *n*. Substitution of $z_t^j = z_t^s$ in Eq. (4), leads us to the existence of such synchronized solution if $\sum_{l=1}^{n} c_{jl} = 1$, *j* = 1, 2, …, *n*. Furthermore, the dynamics of each habitat in the synchronized state satisfies:

$$z_{t+1}^s = (1-\mu)F(z_t^s) + \mu W F(z_t^s) \qquad (5)$$

The solution set in Eq. (5) represents the synchronized state and it depends on the local habitat dynamics and the whole migration process. We are interested in studying the local asymptotic stability of the synchronized state, that is, whether orbits that initiate close to the synchronized state will be attracted to it. In order to achieve this goal, we assume that *C* is diagonalizable and it allows us to decompose the

Jacobian matrix of system in Eq. (4) evaluated at the synchronized state into *n* blocks of dimension *dxd*.

Standard linearization around the synchronized mode yields:

$$\Delta_{t+1} = J(Z_t^s)\Delta_t \qquad (6)$$

where, $\Delta_t \in R^{nd}$ is the perturbation of the synchronized state, $Z_t^s = (z_t^s, z_t^s, ..., z_t^s) \in R^{nd}$ is the synchronized trajectory and $J(Z_t^s)$ is the Jacobian matrix of Eq. (4) evaluated at Z_t^s. Note that $J(Z_t^s)$ can be written as:

$$J(Z_t^s) = (1-\mu)I \otimes DF(z_t^s) + \mu(C \otimes W)DF(z_t^s) \qquad (7)$$

where, *I* is the identity matrix and $\otimes$ represents the Kronecker product. Since *C* is diagonalizable, there exists an invertible matrix *Q* such that $\Lambda^* = QCQ^{-1}$, where, $\Lambda^* = diag(\lambda_0, \lambda_1, ..., \lambda_{n-1})$ and λ_j are the eigenvalues of *C*, *j* = 0, 1, …, *n* − 1. Making the change of variables $Y_t = (Q \otimes I)\Delta_t$ and taking Eqs. (6) and (7) into account, we may write:

$$Y_{t+1} = (Q \otimes I)((1-\mu)I \otimes DF(z_t^s) + \mu C \otimes W) DF(z_t^s))\Delta_t$$
$$= ((1-\mu)Q \otimes DF(z_t^s) + \mu QC \otimes W) DF(z_t^s))\Delta_t \qquad (6)$$

but $\Delta_t = (Q \otimes I)^{-1}Y_t = (Q^{-1} \otimes I)Y_t$, thus:

$$Y_{t+1} = ((1-\mu)I \otimes DF(z_t^s) + \mu\Lambda^* \otimes W) DF(z_t^s))Y_t \qquad (7)$$

that is:

$$Y_{t+1} = \bigoplus_{j=0}^{n-1}((1-\mu)I + \mu\lambda_j W)DF(z_t^s)Y_t \qquad (8)$$

where $\oplus$ represents the direct sum of matrices.

The importance of this block decomposition lies in the fact the local stability of the synchronized state generated in Eq. (5) can be studied by analyzing the spectrum of the individual blocks in Eq. (8). The connectivity matrix *C* is doubly stochastic (all rows and columns add up to one), thus, 1 is the dominant eigenvalue of *C* [6]. The block corresponding to such eigenvalue corresponds to the variational matrix of the system in Eq. (5) that generates the synchronized trajectories, while the other *n* − 1 blocks correspond to transversal directions and govern its local asymptotic stability. In order to describe the synchronized

attractor behavior and its local asymptotic stability, we define the parallel Lyapunov number h by:

$$h(z_0^s) = \lim_{\tau \to \infty} \left\| P_{0,\tau-1} \cdots P_{0,1} P_{0,0} \right\| \qquad (9)$$

where, $P_{0,t} = ((1-\mu)I + \mu W)DF(z_t^s)$, and the maximum transversal Lyapunov number, K, by:

$$K(z_0^s) = \max_{j=1,\ldots,n-1} \left(\lim_{\tau \to \infty} \left\| P_{j,\tau-1} \cdots P_{j,1} P_{j,0} \right\| \right) \qquad (10)$$

where, $P_{j,t} = ((1-\mu)I + \mu \lambda_j W)DF(z_t^s)$, $j = 1, \ldots, n - 1$.

Let ρ be the natural probability measure for G, where, $G(z) = ((1-\mu)I + \mu W)F(z)$, that is, the map that generate the synchronized state given in Eq. (5). Assuming the integrability of $\ln^+ \left\| ((1-\mu)I + \mu \lambda_j W)DF(z) \right\|$ with the ergodicity of ρ, $j = 0, 1, \ldots, n - 1$, we can apply the Ergodic Theorem of Oseledec [7] to guarantee the existence and uniqueness ρ —almost everywhere of the limits defining h in Eq. (9) and K in Eq. (10) and state a criterion for the local asymptotic stability of an attractor in the synchronized invariant mode by:

$$K < 1 \qquad (11)$$

The value h is associated to the synchronized attractor, and chaotic trajectories are observed if $h > 1$, while periodic trajectories at $h < 1$.

3. Numerical Simulations

We perform numerical simulation to illustrate the behavior of our network of patches distributed in two geographical scales. The ensemble trajectories are calculated using Eq. (4), while the dynamics of the synchronized modes are obtained using Eq. (5). In order to determine whether synchronization occurs in the metapopulation, we define the synchronization error by:

$$e_t = \frac{1}{n} \sum_{j=1}^{n} \left| \xi_t^j - \xi_t^{j+1} \right| \qquad (12)$$

where, $\xi_t^j = x_t^{j1} + x_t^{j2} + \ldots + x_t^{jd}$ and $\xi_t^{n+1} = \xi_t^1$. Synchronization is detected when $e_t \to 0$. Moreover, the parallel Lyapunov number h, and the maximum transversal Lyapunov number K are calculated

numerically using an algorithm described in Ref. [8] that calculates the average separation of trajectories in orthogonal directions. If $K < 1$, it means that the synchronized state is stable.

The configuration matrix C can be defined in different forms. Two well-known configurations are the nearest neighbor and the global coupling [4]. We illustrate our results considering habitats linked in a ring format with the two nearest neighbors habitats (two-nearest neighbors coupling), with a symmetric distribution, i.e., 50% to each habitat. Thus, the matrix C is diagonalizable and its eigenvalues are given by:

$$\lambda_0 = 1 \quad \text{and} \quad \lambda_j = \cos\left(\frac{2\pi j}{d}\right), \quad j = 1, \ldots, n-1$$

The local patch dynamics in Eq. (1) is given by the following Ricker map: $f(x) = x \exp(r(1-x))$, where x represents the number of individuals and r represents the population growth rate. A trajectory given by the Ricker model can present different behaviors [9]. For $0 < r < 2$, the trajectory converges to 1. For $0 < r < 2.526$, the fixed point is unstable and the trajectory becomes a two periodic cycle. As r is increased, doubling cycles and chaos are observed. We assume the habitats subdivided in two patches and no dispersal in the local scale. Thus, the local habitat dynamics in Eq. (2) is given by $F(x_1, x_2) = (f(x_1), f(x_2))$. Of course, others local dynamics could be considered, but our main concernment is to illustrate the behaviors generated by two different distributions matrices.

3.1 Preferential Distribution

We start describing the case where individuals migrate to patch 1 in the neighboring habitat. In this case, the matrix W is given by:

$$W = \begin{pmatrix} 1 & 1 \\ 0 & 0 \end{pmatrix} \qquad (13)$$

This case is called as preferential distribution and the system of Eq. (5) is written as:

$$\begin{pmatrix} x_{t+1}^1 \\ x_{t+1}^2 \end{pmatrix} = (1-\mu)\begin{pmatrix} f(x_t^1) \\ f(x_t^2) \end{pmatrix} + \mu \begin{pmatrix} 1 & 1 \\ 0 & 0 \end{pmatrix}\begin{pmatrix} f(x_t^1) \\ f(x_t^2) \end{pmatrix} \qquad (14)$$

Eq. (14) can also be written as:

$$\begin{pmatrix} x^1_{t+1} \\ x^2_{t+1} \end{pmatrix} = \begin{pmatrix} f(x^1_t) + \mu f(x^2_t) \\ f(x^2_t) - \mu f(x^2_t) \end{pmatrix} \quad (15)$$

Observing that the above equations synthesize two populations coupled by dispersal where just one of them migrates. In Eq. (15), we are able to calculate fixed points and analyze its stability.

Denoting the fixed points in Eq. (15) by $X^* = (x^*_1, x^*_2)$, we have:

$$\begin{pmatrix} x^*_1 \\ x^*_2 \end{pmatrix} = \begin{pmatrix} x^*_1 \exp(r(1-x^*_1)) + \mu x^*_2 \exp(r(1-x^*_2)) \\ x^*_2 \exp(r(1-x^*_2)) - \mu x^*_2 \exp(r(1-x^*_2)) \end{pmatrix} (16)$$

Thus, we can calculate three fixed points that are given by: (1) $X^*_1 = (0,0)$, (2) $X^*_2 = (1,0)$ and

(3) $X^*_3 = \left(x^*_1, 1 - \dfrac{\log(1/(1-\mu))}{r} \right)$.

The third fixed point cannot be calculated analytically, but we can perform numerical simulation to calculate it through an iterative method. The stability analysis yields:

(1) X^*_1 is stable if $r < 0$;

(2) X^*_2 is stable if $0 < r < 2$ and $1 - \exp(-r) < \mu \leq 1$;

(3) X^*_3 is stable if $1 - \exp(-r+2) < \mu < 1 - \exp(-r)$.

The first fixed point is not applicable to the model, since the growth rate is less than zero. The second fixed point is characterized by persistence in patch 1 and extinction in patch 2. The last fixed point is stable within an interval that relates the growth rate and the dispersal fraction, thus, we have a stabilizing effect on the synchronized trajectory. In Table 1, we show three different values of the growth rate and the respective interval where the fixed points are stable.

We can observe in Fig. 2 the perfect agreement between the above stability analysis and the attractors that are a fixed point generated by the system in Eq. (5). Fig. 2a shows extinction in patch 2 and it is characterized by high migration rates. Fig. 2b shows the trajectory decreasing its periodicity as the migration rate is increased. Even when the patch local dynamics is chaotic, it goes from chaos to periodic

Table 1   Behavior of Ricker map for three growth rates and interval where the synchronized trajectory is a fixed point.

r	Trajectory	Stability of X^*_2	Stability of X^*_3
1.8	Fixed point	$\mu > 0.8347$	$\mu \leq 0.8347$
2.6	4-Periodic	--	$0.4 < \mu < 0.91$
3.1	Chaos	--	$0.67 < \mu < 0.95$
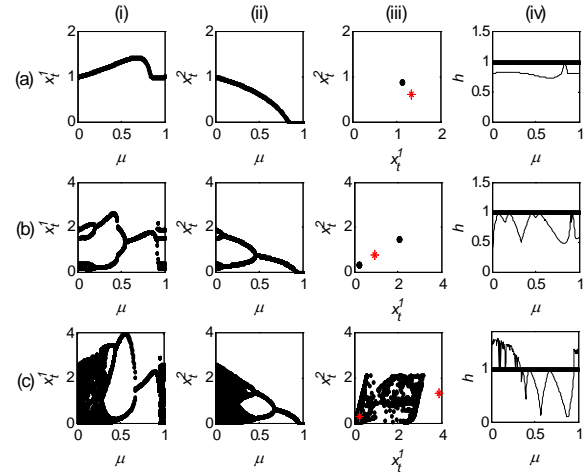
Fig. 2   Synchronized attractor for two patches within each habitat and preferential distribution. Local habitat dynamics: $F(x_1,x_2) = (x_1 \exp(r(1-x_1)), x_2 \exp(r(1-x_2)))$. **(a)** $r = 1.8$; **(b)** $r = 2.6$; **(c)** $r = 3.1$. **(i)** x^1_t vs μ; **(ii)** x^2_t vs μ; **(iii)** x^2_t vs x^1_t, for $\mu = 0.2$ **(black) and** $\mu = 0.5$ **(red*); (iv)** h.

trajectories or equilibrium points due to the dispersal process (Fig. 2c). Moreover, due to the preferential movement, the synchronized attractors tend to have more population density in patch 1 for any value of the dispersal fraction.

Fig. 3 shows the synchronization error and the correspondent maximum transversal Lyapunov number. We observe that periodic synchronized trajectories are stable and chaotic synchronized trajectories depend on the dispersal process. Thus, we show the results for $r = 3.1$ whose patch local dynamics is chaotic. In this case, we observe that migration rates larger than 0.335 and smaller than 0.995 generate stable synchronized trajectories. Moreover, the increase of 5 habitats to 10 habitats does not change significantly the maximum transversal Lyapunov number.

3.2 Uniform Distribution

Now we assume that the individuals that reach a new habitat choose between patch 1 and patch 2 with the same probability. In this case, the matrix W is given by:

$$W = \begin{pmatrix} 0.5 & 0.5 \\ 0.5 & 0.5 \end{pmatrix} \qquad (17)$$
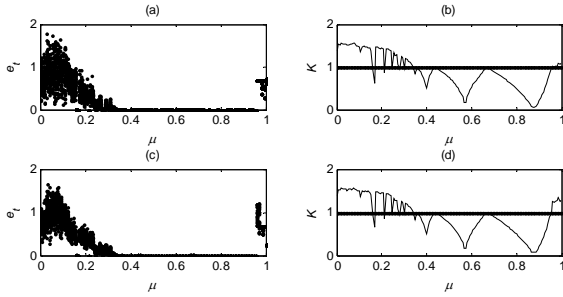
Fig. 3 Synchronization error ((a) and (c)) and respective maximum transversal Lyapunov number ((b) and (d)). Local habitat dynamics: $F(x_1, x_2) = (x_1 \exp(r(1-x_1)), x_2 \exp(r(1-x_2)))$**, with** $r = 3.1$**. (a) 5 habitats; (b) 10 habitats. The habitats synchronize in the regions that** $K < 1$**.**

This case is called uniform distribution and we can write the system of Eq. (5) as:

$$\begin{pmatrix} x_{t+1}^1 \\ x_{t+1}^2 \end{pmatrix} = \begin{pmatrix} f(x_t^1) - 0.5\mu f(x_t^1) + 0.5\mu f(x_t^2) \\ f(x_t^2) - 0.5\mu f(x_t^2) + 0.5\mu f(x_t^1) \end{pmatrix} \qquad (18)$$

The above system of equations synthesize two populations coupled by symmetric dispersal [10, 11]. For $r = 1.8$, we can observe that the synchronized trajectory converge to the value 1 independent of the migration rate (Fig. 4a). It is exactly the fixed point of the Richer map given in Eq. (1). Intuitively, we could expect that the synchronized state has all the patches with the same density due to the distribution and equation symmetries, but it is not what exactly happens. For $r = 2.6$, whose local patch dynamics has a trajectory with period 4, we can observe a different synchronized attractor for small values of the migration fractions, as shown in Fig. 4b. It shows that weak interaction can generate different dynamics even if the patch local dynamics is periodic. For $r = 3.1$, we observe the synchronized attractors mainly

characterized by three different behaviors, as shown in Fig. 4c. For small migration rates, $\mu < 0.09$, the synchronized attractors are chaotic. For intermediate migration rates, $0.09 \le \mu \le 0.27$, the synchronized attractors are two periodic and out of phase. For values larger than 0.27, they are over the phase diagonal.
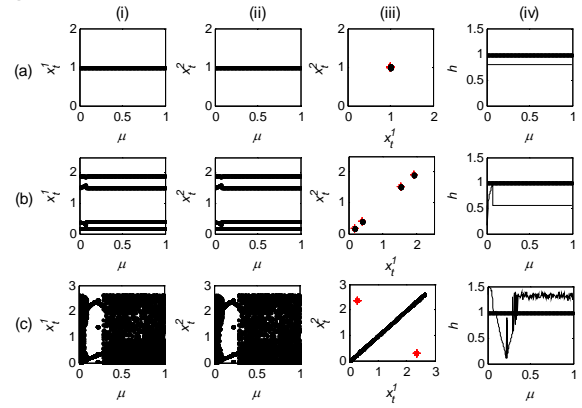
Fig. 4 Synchronized attractor for two patches within each habitat and uniform distribution. Local habitat dynamics $F(x_1, x_2) = (x_1 \exp(r(1-x_1)), x_2 \exp(r(1-x_2)))$**. (a) r = 1.8; (b) r = 2.6; (c) r = 3.1. (i) x_t^1 vs μ; (ii) x_t^2 vs μ; (iii) x_t^2 vs x_t^1 for** $\mu = 0.2$ **(red*) and** $\mu = 0.5$ **(black); (iv) h.**
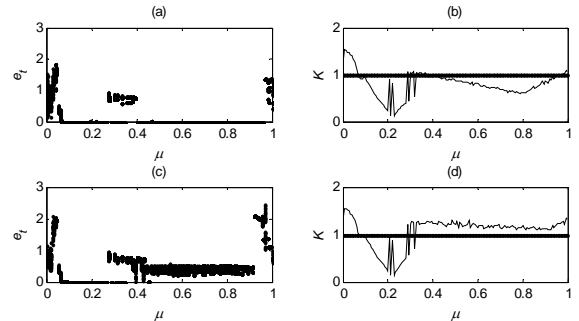
Fig. 5 Synchronization error ((a) and (c)) and respective maximum transversal Lyapunov number ((b) and (d)). Local habitat dynamics: $F(x_1, x_2) = (x_1 \exp(r(1-x_1)), x_2 \exp(r(1-x_2)))$**, with** $r = 3.1$**. (a) 5 habitats; (b) 10 habitats. The habitats synchronize in the regions that** $K < 1$**.**

Fig. 5 shows the synchronization error and the maximum transversal Lyapunov number. Once again, we observe that periodic synchronized trajectories are stable and we perform numerical simulations for r = 3.1. We observe that synchronized trajectories depend on the dispersal process and the habitats number.

4. Discussion

We propose a metapopulation model composed by patches distributed in two geographical scales. In a regional scale, the basic unit is a habitat and individuals disperse among them. In a local scale, there is some granularity in the habitats and they are subdivided in patches. In this case, the basic unit is the patch and individuals disperse among the patches and the habitats. Due to the subdivision of habitats in patches, we assume that individuals arrive in the neighboring habitats and choose certain patches with different probabilities. This assumption defines a distribution matrix, W, that quantifies the preference of individuals to settle in certain patches.

We then analyze the synchronization of the model and obtain a criterion to the local stability of synchronized solutions. The criterion is obtained from the block decomposition of the Jacobian matrix of the system in Eq. (4). The key point is that one of the blocks corresponds to the variational matrix of the system in Eq. (5) that generates the synchronized trajectories and allows us to calculate the parallel Lyapunov number, h. It provides information about the trajectories of the synchronized state, i.e., a periodic cycle ($h < 1$) or a chaotic behavior ($h > 1$). The other blocks correspond to transversal directions necessary to calculate the maximum transversal Lyapunov number, K, that inform whether trajectories that initiate near to the synchronized state are attracted ($K < 1$) or repelled ($K > 1$) to it.

Our observation based on numerical simulations show different behaviors that depend on how the individuals are distributed in the local patches that compose a habitat. In the case of preferential distribution, individuals that reach a new habitat migrate preferentially to patch 1, we observe extinction and persistence in the local patches and a stabilizing effect on the synchronized trajectories especially for high migration rates (Fig. 2). In the case of uniform distribution, individuals choose patches in the neighboring habitat with the same probability, the synchronized trajectories are characterized by three behaviors when the local patch dynamics is chaotic. For small migration rates, the synchronized trajectories are chaotic and unstable. Intermediate migration rates characterize synchronized trajectories out of phase and stable, while high migration rates characterize in-phase trajectories and its stability depends on the migration fraction (Figs. 4 and 5). Of course, different local patch dynamics and distribution matrices could be considered, but our main concernment was to describe patterns that could be important to describe metapopulations patterns.

References

[1]   R. Levins, Some demographic and genetic consequences of environmental heterogeneity for biological control, Bull. Entom. Soc. Am. 15 (1969) 237-240.

[2]   R.M. May, A.L. Lloyd, Synchronicity, chaos and population cycles: Spatial coherence in an uncertain world, Trends Ecol. Evol. 14 (1999) 417-418.

[3]   J.C. Allen, W.M. Schauffer, D. Rosko, Chaos reduces species extinction by amplifying local population noise, Nature 364 (1993) 229-232.

[4]   D.J.D. Earn, S.A. Levin, P. Rohani, Coherence and conservation, Science 290 (2000) 1360-1364.

[5]   J.A.L. Silva, F.T. Giordani, Density-dependent migration and synchronism in metapopulations, Bull. Math. Biol. 68 (2006) 451-465.

[6]   P. Lancaster, M. Tismenetsky, The Theory of Matrices, Academic Press, London, 1985.

[7]   J.P. Eckmann, D. Ruelle, Ergodic theory of chaos and strange attractors, Rev. Modern Phys. 57 (1985) 617-656.

[8]   I. Shimada, T. Nagashima, A numerical approach to ergodic problem of dissipative dynamical systems, Prog. Theor. Phys. 61 (1979) 1605-1616.

[9]   R.M. May, Biological populations with nonoverlapping generations: Stable points, stable cycles, and chaos, Science 186 (1974) 645-647.

[10] A. Hastings, Complex interactions between dispersal and dynamics: Lessons from coupled logistic equations, Ecology 74 (1993) 1362-1372.

[11] B.E. Kendall, Spatial structure, environmental, heterogeneity, and population dynamics: Analysis of the coupled logistic map, Theor. Pop. Biol. 54 (1998) 11-37.

Dynamic Diagrams—Post Processing Software Tools for Simulation Analysis of Spacecraft Docking Dynamics

Andrey V. Yaskevich and Ivan E. Chernyshev

Space Electromechanical System Division, Rocket Space Corporation "Energia", Korolev 141070, Russia

Abstract: Realistic 3D-animation is used in all motion simulation systems of mechanisms and other mechanicals systems. It provides a high-quality illustration of time processes, but it has a weak capability for analysis of their dynamics, for simultaneous display of contact interaction and functioning of mechanisms of different motion types. A spacecraft docking is characterized by a complex contact interaction of docking assemblies with mechanisms and devices of different motion types. Integration and time synchronization of the animation, plots and numerical values greatly facilitates the understanding of dynamics features of these processes. Usage of simple wireframe graphical models allows displaying all contact points. A changing of the set of graphical elements focuses attention on major events of a simulated process. Graphical models developed with consideration of these features and used for spacecraft docking simulation analysis are called dynamic diagrams and described in this paper.

Key words: Spacecraft docking, math modelling, computer graphics.

1. Introduction

Computer 3D-animation and plots of parameter changing are usual representations of time processes. Animation based on realistic images of moving objects and their elements, with consideration of a large number of details, light source direction and other effects, is used in the simulation systems of mechanical system dynamics, Adams [1], Catia [2], Dads [3], Pro/mechanica motion [4], vortex dynamics [5], open dynamic engine [6], Simecs [7], universal mechanism [8], Euler [9], etc. The graphical models of such universal systems show the spatial motion of separate mechanism elements, e.g. a shock-absorber system, or the motion of whole vehicles, such as cars, trains, airplanes, etc. Also, images often contain elements missing in mathematical motion models. The animation of transmissions and rotation mechanisms includes detailed images of gears. Images are normally

presented as isometric views, with the capability of an arbitrary change of the look direction. Such graphical models of time processes ensure a high illustration quality although they have the following drawbacks:

• Lack of integration with numerical values and plots of motion math model parameters, weak capabilities for analysis of the causes of one or another event occurrence;

• Difficulty to integrate 3D models of mechanisms of different motion types;

• Weak capabilities for displaying contact interaction of mechanical systems.

For spacecraft docking processes, spatial, multiple and stochastic contact interaction of docking assemblies is typical. Mechanisms of such assemblies have elements of different motion types. In particular, links of translational and angular motion connect the contacting buffer link of the docking mechanism with rotatory type devices, such as springs, dampers, friction clutches, differentials and electrical motors that provide kinetic energy absorption and alignment and retraction of docking interfaces. Given this, a

Corresponding author: Andrey V. Yaskevich, Ph.D., research fields: space docking and robotic system dynamics. E-mail: Andrey.Yaskevich@rsce.ru.

simplified animation, integrated and time-synchronized with numerical parameters of the motion math model, and supplemented with specific graphical elements for the explanation of the functioning of certain devices of docking assemblies and mechanisms, can be more useful for understanding the docking dynamics features than a highly realistic virtual reality. Graphical models used for such approach called dynamical diagrams, are described in this paper.

The paper consists of the following sections: (1) introduction; (2) design concept of graphical models for spacecraft docking dynamics analysis; (3) dynamic diagram for displaying the interaction of probe-cone assemblies; (4) graphical model of APAS peripheral docking mechanism functioning; (5) dynamic diagram for analysis of berthing; (6) conclusions.

2. Design Concept of Graphical Models for Spacecraft Docking Dynamics Analysis

Docking is a controlled mechanical process of spacecraft connection in orbit. It is performed with a docking system that includes docking assemblies and control avionics. Methods of design, development, simulation and testing of different docking systems were first described in Ref. [10]. Their short review is presented in Ref. [11]. Docking assemblies directly implements the mechanical process of spacecraft connection with initial conditions provided by the spacecraft rendezvous system. Generally, this process can be divided by four main steps. The first step starts at the moment of the first contact and ends with a formation of a primary mechanical connection of the spacecraft (capture). At the second step, the major part of the spacecraft relative motion kinetic energy is absorbed. At the third step, the alignment of the relative positions of the assemblies is performed, and at the last fourth step a stiff and strong mechanical connection of the docking interfaces is acquired. A relative displacement of the units is determined by contact reaction forces of their guide surfaces. Contacts of

docking units are spatial, multiple and stochastic.

For a sequential restriction of relative displacements of docking units, and spacecraft accordingly, several different mechanisms are used. Normally, during a docking sequence only mechanisms of one docking unit operate, and that unit is called active. The reciprocal passive unit interacts with links of these mechanisms by elements of its guide surface.

A docking mechanism is installed along the longitudinal axis of the active unit body, and performs the following functions:

● Elimination of misalignments between elements of contacting buffer link guide surfaces and the passive unit until a value sufficient to achieve a capture;

● Absorption of the kinetic energy of the spacecraft relative motion, and restriction of their maximal relative displacements after the capture;

● Alignment and retraction of the unit docking planes.

Capture mechanisms are installed on the docking mechanism buffer link. Their spring-loaded links move under external contact forces and get engaged with mechanical stops on the reciprocal passive docking unit body. Hard mating mechanisms are installed on the docking unit bodies and ensure their stiff, hard and leak-proof connection. They develop great forces with a low link displacement amplitude.

Sensors installed in mechanisms and on both docking units register occurrences of typical events or a change of link lengths. Based on this information, the active unit avionics determines the process status and performed automatic control. First contact, capture and other signals can be transmitted to the spacecraft control systems to change their motion modes.

Docking units can be of two main types—central (probe-cone) or peripheral, depending on the location of the guide surface elements, kinematics of the docking mechanisms and the location of the capture mechanisms. They have the following common design features. Translational movements of separate links of the docking mechanism are linked through ball screw

transmissions with rotations of the shafts of small springs, magnetic dampers, friction clutches and electric motors. Redistribution of rotational motion is performed by planetary differentials. Docking mechanism springs are preloaded, they have a finite stroke at which exhaust the internal mechanical stop is reached. Spring stiffness characteristics are symmetrical with respect to the sign of the deformation, which change depending on its value. Therefore, such devices are called spring mechanisms due to their complex design. Magnetic dampers can be non-controllable (operating constantly) or controllable, i.e., switched temporarily.

Graphical models that provide a better understanding of the influence of the above mentioned design features on docking dynamics are developed for different types of docking units, and sometimes for individual operations in accordance with the following principles.

The graphical image of docking units, as a rule, is more important than the image of docking objects.

The possibility of simultaneous comparison of mixed type data for a docking dynamics analysis is more important than a highly realistic image of objects and their elements. Animation and graphics provide the maximal speed of perception, and textual data (inscriptions and numbers) enable an accurate analysis of simulation results.

Wireframe graphical models of docking units are the basis for computer animation because they allow displaying all their spatial multiple stochastic contacts. Projections of wireframe models on separate coordinate planes are more demonstrative and convenient than their isometric views.

Simplified symbolic representation of individual structural elements and an artificial change of their scale is used for a clearer idea of the movements that cause contact and deformation forces.

Compatibility of graphical models with binary files of simulation results is ensured by using simple text templates. A dynamic mnemonic diagram displays only the geometric elements and numerical parameters used in the motion math model.

All integrated data of the graphical model is changed synchronously during its scrolling over the current time axis.

Emphasis on events affecting the docking process is made by changing the configuration of displayed graphical objects, by color or by specific symbols.

The described below graphical models used for docking dynamics analysis make use of three types of data changing synchronously:

● 3D wireframe images of docking units and their contacts;

● Diagrams displaying conversion and absorption of mechanical energy in docking mechanism devices;

● Time plots of a selected group of parameters, e.g. components of interface forces and moments.

All information is displayed in several (usually three) windows. The relative position and contacts of docking units are shown in the upper window. Some geometric elements can be displayed only if conditions for an occurrence of a certain contact type are met. This means that the image in the upper window may change depending on the simulated process phase and focus on its main features.

The middle window shows mechanical energy conversion and absorption by the spring mechanisms, magnetic dampers and friction clutch of the docking mechanism, using vertical or horizontal bars colored with three different colors. The gray color corresponds to the absence of deformation or movement, the magenta (fuchsia) color marks spring compression and positive shaft rotation velocities, and the blue color goes with tension and negative velocities. If needed, the upper two windows display a simplified kinematics of a docking mechanism.

Math modelling results in several hundreds of parameters changing with time. They are saved in three binary files describing:

● Relative motion of docking objects, forces and moments applied on them, flexible oscillations of their structures;

- Functioning of a docking mechanism, movements and deformations of its links, shock absorbers, characteristic contact points and corresponding reaction forces;
  - Functioning of sensors and latches.

File names are made up from characters indicating their purpose and simulation case name. The content of each file is described by a text template file. A user menu allows selecting any pre-simulated docking case and any group of correlated parameters, e.g. components of interface forces and moments, functional parameters of individual docking mechanism devices, characteristic distances, deformations and forces in contact points to be displayed as plots in the lower window. Information on most important parameters is replicated in the upper windows in the numerical text format.

Upon an enter key press, plots in the lower window start moving from right to left relative to the current time vertical axis. They are supplemented by numerical parameter values. This data is located in the lower window on the left, together with the indication of the simulation date, case name, simulated process duration, current time value and time increment value of the dynamic diagram state change. All geometric and numerical data in the upper two windows changes synchronously with the plots in the lower window. A break, restart and scrolling speed change for the whole graphical model is made with hot buttons. An increase or decrease of the plot display scale is made with the mouse cursor pointing to the corresponding arrows.

Thus developed graphical models due to their features got the conventional name dynamical diagrams. Below are briefly described their implementations for analysis of functioning of different docking systems. The main focus is made on the first three stages, which are characterized by high amplitudes and quick change of dynamic process parameters. Graphical models for dynamics analysis of hard mating docking objects are currently under development.

3. Dynamic Diagram for Displaying Interaction of Probe-Cone Units

The guide contact surface of the central type passive docking unit represents a receiving cone with a cylindrical receiving socket on its top, with grooves for latch engagement, i.e., to ensure capture. A simplified diagram of the active unit docking mechanism is shown in Fig. 1. A buffer link is represented by the semi-spherical probe head. It can contact with the receiving cone and the passive unit socket. Under the contact force, the probe can translationally move along the longitudinal axis of the movable body coupled with the base with a universal joint. This relative movement is transformed by a ball-screw joint to a rotational motion of the axial shock absorber devices, i.e., spring mechanism SMx, friction clutch FrC and non-controllable magnetic damper NCDx. The friction clutch dissipates kinetic energy at high closing velocities of docking objects. The LPS sensor shows a probe length change.

An external contact force may also be applied to the head in the lateral direction rotating the movable body and causing probe bending. Centration and limitation of turns of the movable body is provided by two translational spring mechanisms SM1 and SM2. They are positioned in the mutually perpendicular planes that pass through the longitudinal axis of the docking mechanism. Two kinematic chains of the magnetic dampers are also positioned in the perpendicular planes turned by 45 degrees about the planes of the spring mechanisms. Their movement is also restricted by the mechanical stops. Each of these chains sets in rotation the non-controllable (NCD1, NCD2) and the more powerful controllable magnetic dampers (CD1, CD2) as well as the BPR and BPT sensors of yaw and pitch rotation of the movable body. The bending angle of the probe end is negligible due to the spherical shape of its head. That is why the distributed bending deformation is replaced by the rotation angle in the dummy joint, which is located in the point where the probe exits the movable body.
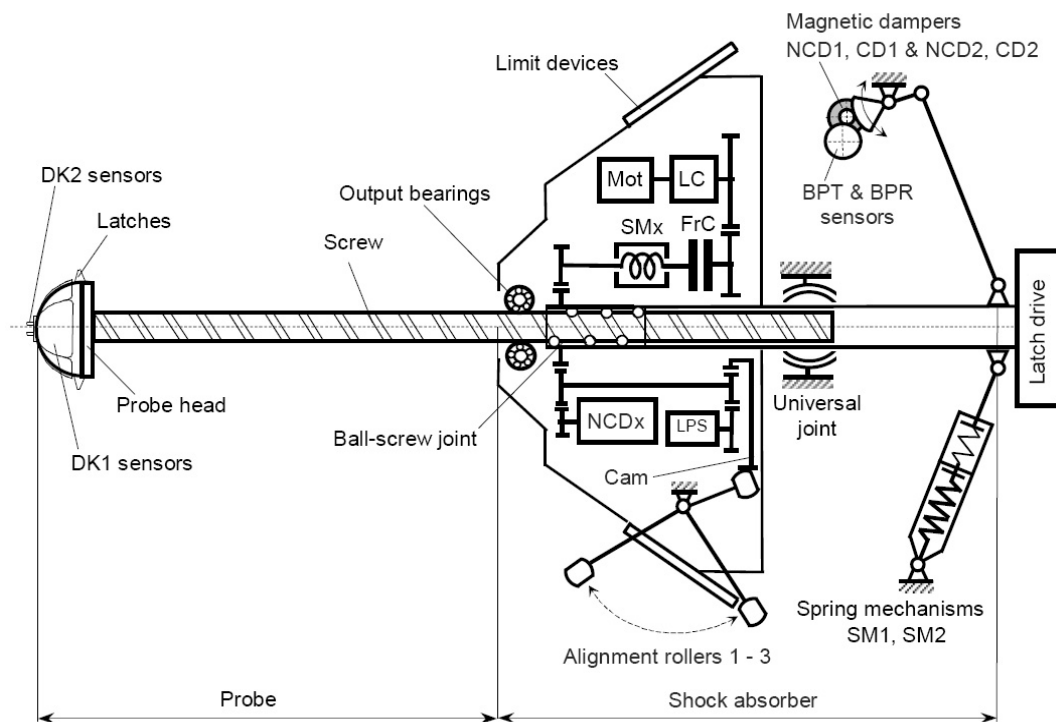
Fig. 1 Simplified kinematic diagram of the probe-cone docking mechanism.

The DK1 and DK2 sensors are located on the probe head surface which detect its contact with the receiving cone and the receiving socket bottom, and the four latches and two capture sensors are located along the perimeter. The first DK1 signal may initiate an activation of the jet thrusters to induce an axis force accelerating capture. After the head entering the receiving socket and capture, upon the head hitting the socket bottom, the DK2 signal initiates an automatic sequence of active docking assembly control commands. These commands switch on and off the controllable magnetic dampers, the docking mechanism drive during alignment and retraction, and the drives of all the mechanisms in turn upon rigid connection of the assemblies.

The turn amplitudes of the docking mechanism about the passive assembly after capture are restricted upon contacts of the limit devices of the movable body with the receiving cone and upon contacts of the latches with the grooves and stops of the receiving socket. After absorption of the main part of the energy of docking objects relative motion, the electric motor

Mot of the docking mechanism drive pulls in the probe into the movable body and at the same time pulls out three levers with the alignment rollers, which upon contact with the receiving cone provide the coordinated position of the docking assemblies on yaw and pitch. Before the planes of the docking assembly connect, these levers take their initial positions in the docking mechanism movable body. Roll alignment is ensured at a contact of the latches with the guide grooves of the receiving socket. Until retraction, the rotation of the kinematic chain between the friction clutch and the electric motor is blocked by the lock clutch LC.

The docking sequence with the use of probe-cone units can be briefly illustrated by a set of dynamical diagrams, which correspond to different phases of this process. It starts with contacts between the probe head and the receiving cone. The state of the mechanical process upon the first contact is reflected by the dynamical diagram in Fig. 2. The wireframe models of the docking assemblies, numerical parameters of their relative position and motion and contact points are displayed in the upper window.
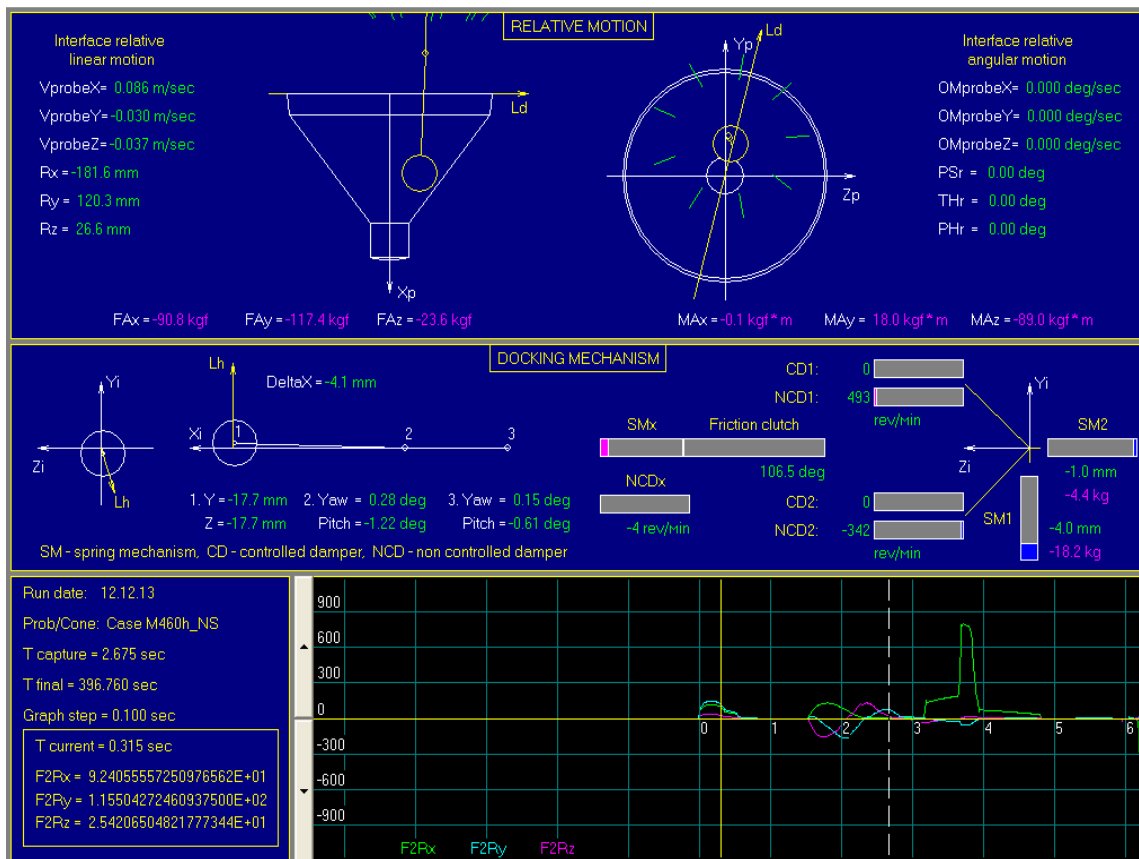
Fig. 2   The first contact between the probe head and the receiving cone.

Also, the numerical values of FAx, FAy, FAz and MAx, MAy, MAz components of the total contact forces and moments applied on the active assembly are duplicated here. The wireframe models are represented by their projections onto the docking plane of the passive assembly and onto the Ld plane, which passes through the longitudinal axis of the receiving cone and the spherical head center.

The middle window displays a simplified diagram of the docking mechanism, movable body rotation angles, probe bends, probe bending plane Lh, compression of the axial SMx, tension of the lateral SM1 and SM2, rotation velocity of the axial and lateral controllable (CD1, CD2) and non-controllable (NCD1, NCD2) dampers. Mnemonic images of absorption devices as bars are supplemented with numerical values of deformations and velocities.

The plots of selected numerical parameters of the docking process (in this case, contact forces and

moments applied on the passive assembly) are displayed in the lower window. The current state of the dynamic diagram corresponds to the plots crossing the current time axis (vertical yellow line). The simulation date, number of cases, time of capture, time increment value of the graphical model state, current time and numerical values of the parameters displayed on the plot are shown on the left of this window.

The vertical dotted line on the plot corresponds to the expected moment of the capture event. All the values in the docking motion equations are expressed in SI, although all the numerical parameters of the graphical model are given in the technical engineer system units for the convenience of docking system designers.

The probe head latches and the receiving socket grooves begin to display in a simplified way in the top window just before the capture event (Fig. 3). The image scale is enlarged for better perception.
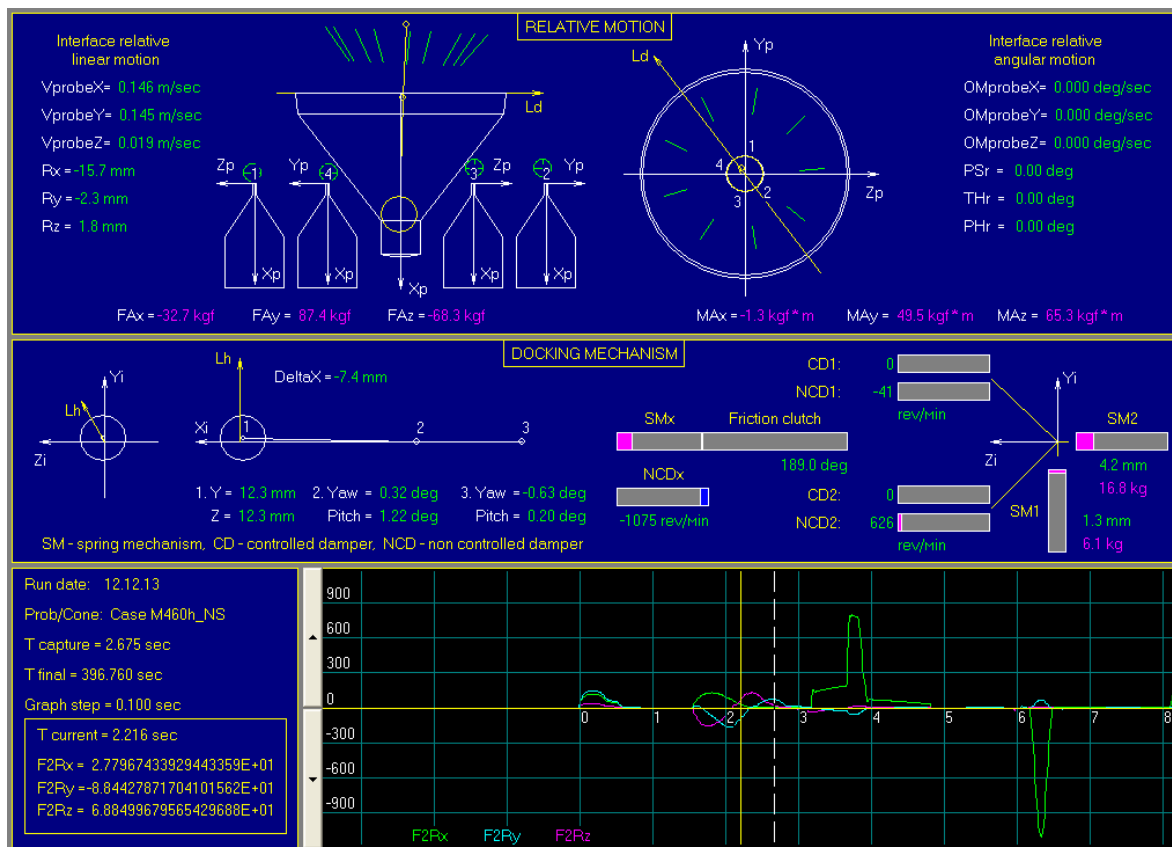
Fig. 3　Appearance of images of the receiving socket latches and grooves before capture.

At this state of the process, the deformation of the lateral SM and rotation velocity of lateral dampers have changed sign to the opposite due to the different position of the probe head relative to the receiving cone. The latches and grooves begin to display before the capture event, because under certain conditions this event may not occur, and in this case an analysis of docking process anomaly reasons is needed.

Fig. 4 displays the probe head hitting the receiving socket after capture. Upon compression, the axial spring mechanism SMx has exhausted its stroke and now transfers rotation to the friction brake with a high resistance moment. This causes a significant increase of the axial contact force applied on the both docking assemblies. Their range rate drops, the probe slumping speed and the axial damper rotation velocity also decrease. After capture, interface loads are mainly determined by the docking spacecraft relative motion energy. That is why the corresponding numerical parameters are displayed in the top window instead of the relative motion parameters of the assemblies.

After the absorption of the kinetic energy of the docking objects, the deformation energy of the compressed axial spring mechanism is released. The docking assemblies start moving in the opposite directions, the probe head leaves the socket bottom and after a while its latches hit the receiving socket grooves or stops. This docking mechanism version does not have devices to damper this hit, therefore, despite the small recoil motion velocity, the contact force amplitude is higher than upon the direct impact. The dynamic diagram in Fig. 5 shows the released state of the axial spring and the accumulated irreversible slump of the friction clutch.

After capture, the probe head and the receiving socket form a joint, which does not prevent relative angular turns of the docking assemblies on yaw and pitch.
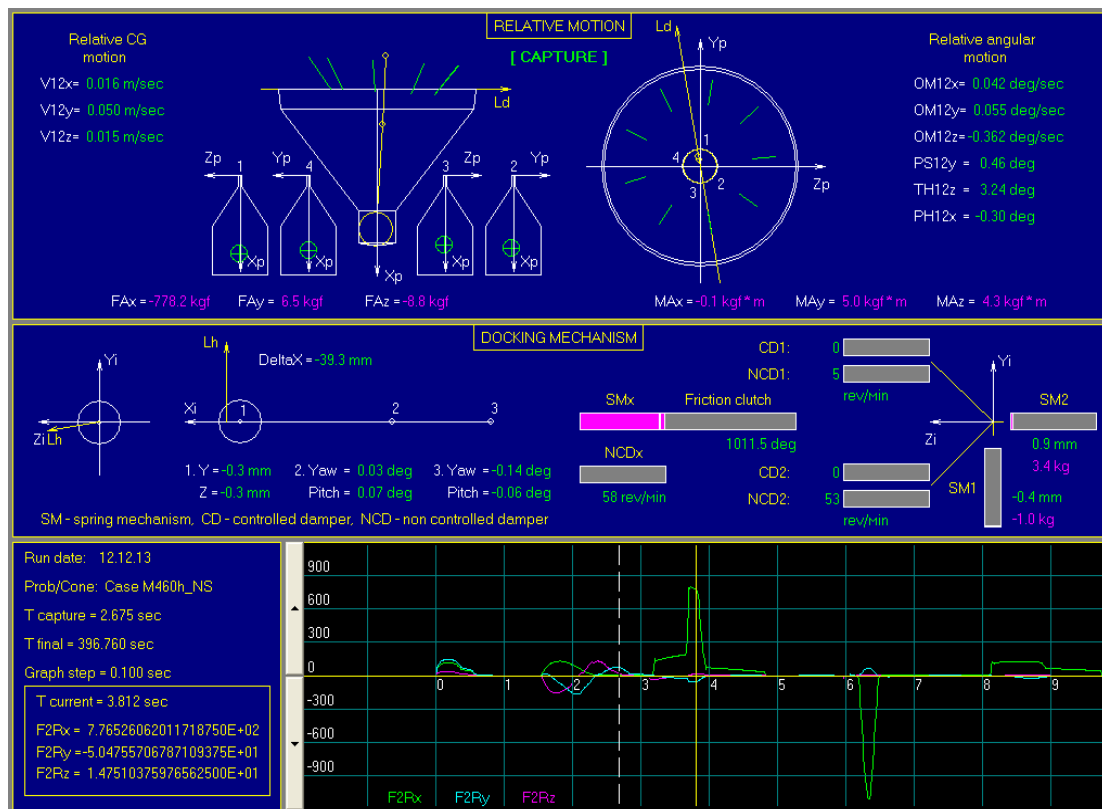
Fig. 4   Exhaust of SMx stroke and FrC activation upon probe head hitting the receiving socket bottom.
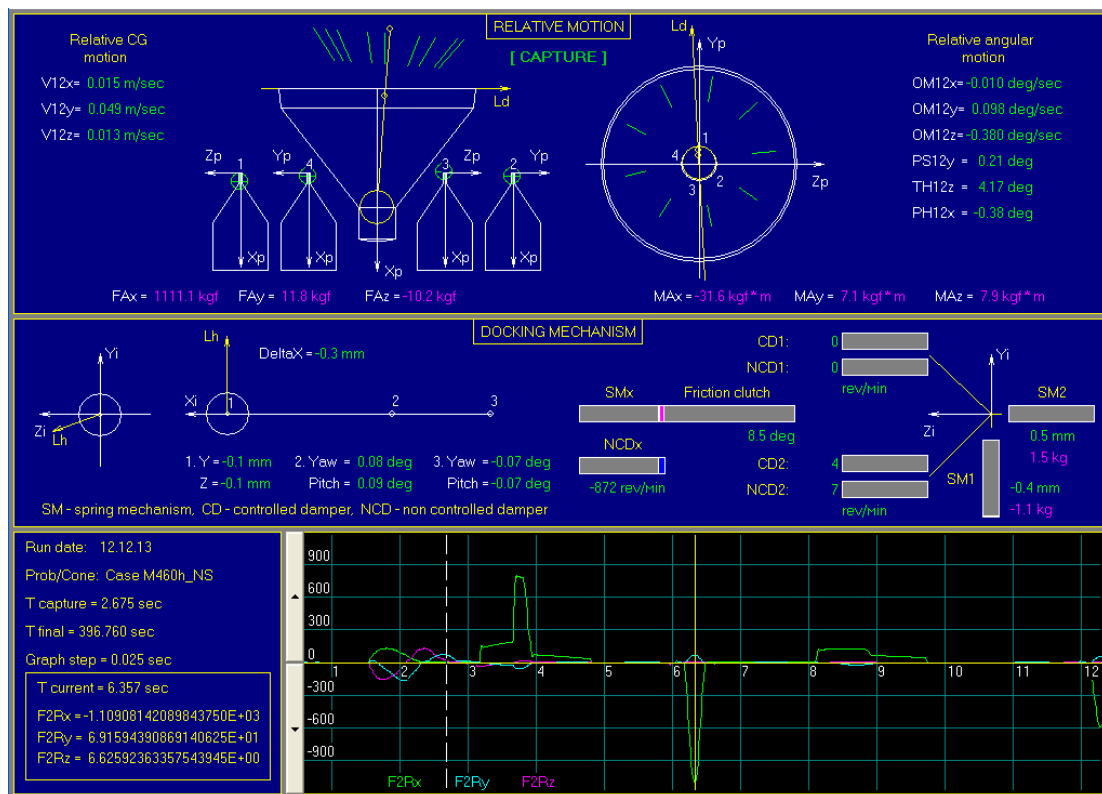
Fig. 5   Undamped impact of the latches on the receiving socket stops.

This is ensured by contacts of the limit devices on the docking mechanism movable body with a face or surface of the receiving cone. One or two of the nine limit devices can contact simultaneously. Presence of the contacts is confirmed in the top window of the graphical model with the corresponding signs—magenta circles. The additional text message informs about the contacting limit device numbers. The graphical model in Fig. 6 reflects the contact of the first limit device with the receiving cone during the 43th second of the process. In this moment, the controllable lateral dampers are already switched off and their rotation velocities are equal to zero. Upon retraction and alignment of the docking assemblies, the probe length exceeding the bounds of the docking mechanism movable body, decreases. The latches of the retracted head contact with inclined faces of the receiving socket grooves and provide roll alignment of the docking mechanism. The aligning rollers that contact with the receiving cone provide approximately co-axial

positions of the passive assembly and the docking mechanism. They are displayed in the top window of the diagram if they exceed the bounds of the limit devices of the docking mechanism movable body. The contacting rollers are shown in magenta, the non-contacting rollers—in green (Fig. 7). Pitch and yaw alignment of the docking mechanism movable body about the receiving cone leaves degrees of freedom in the universal joint, about which angular oscillations of the docking objects occur during retraction. These movements are counteracted by the spring mechanisms and non-controllable magnetic dampers of the lateral shock-absorber of the docking mechanism.

4. Graphical Model of APAS (Androgynous Peripheral Assembly System) Functioning

A kinematic basis of the peripheral assembly mechanisms is usually a Gough-Stewart platform [12, 13]. Controlling kinematic chains of such platform in
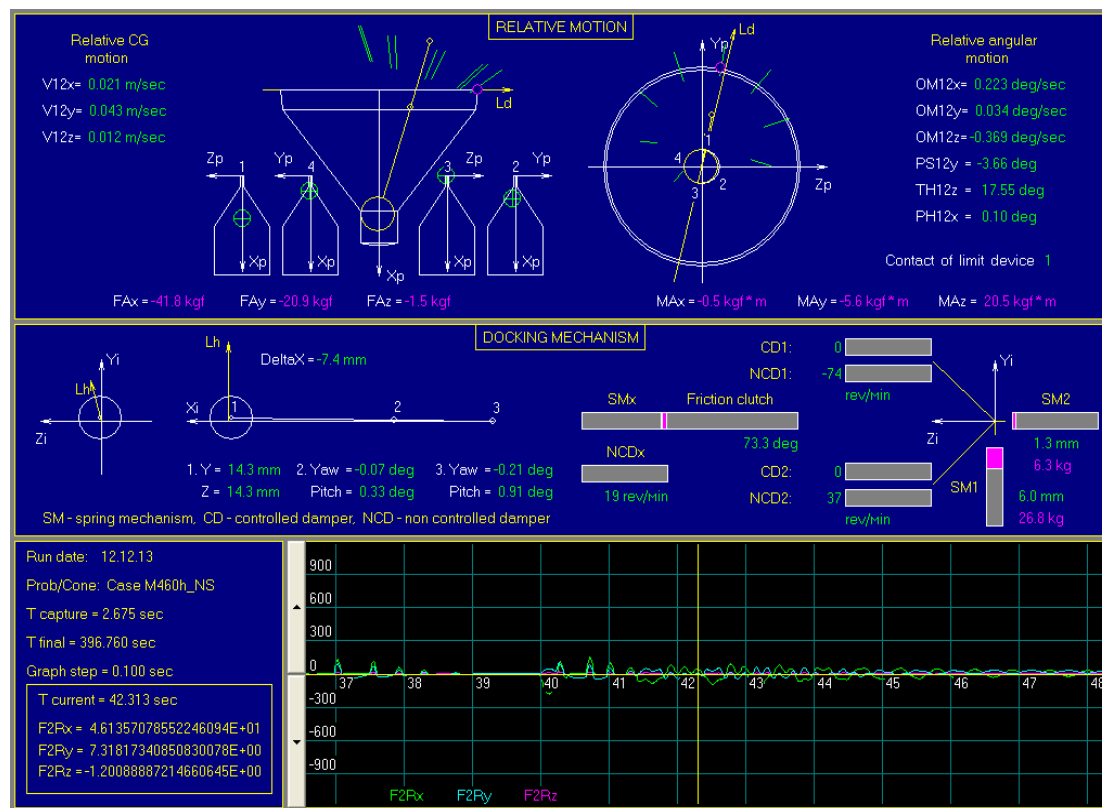
Fig. 6   A special symbol marking the contact of the limit device and the receiving cone during retraction.
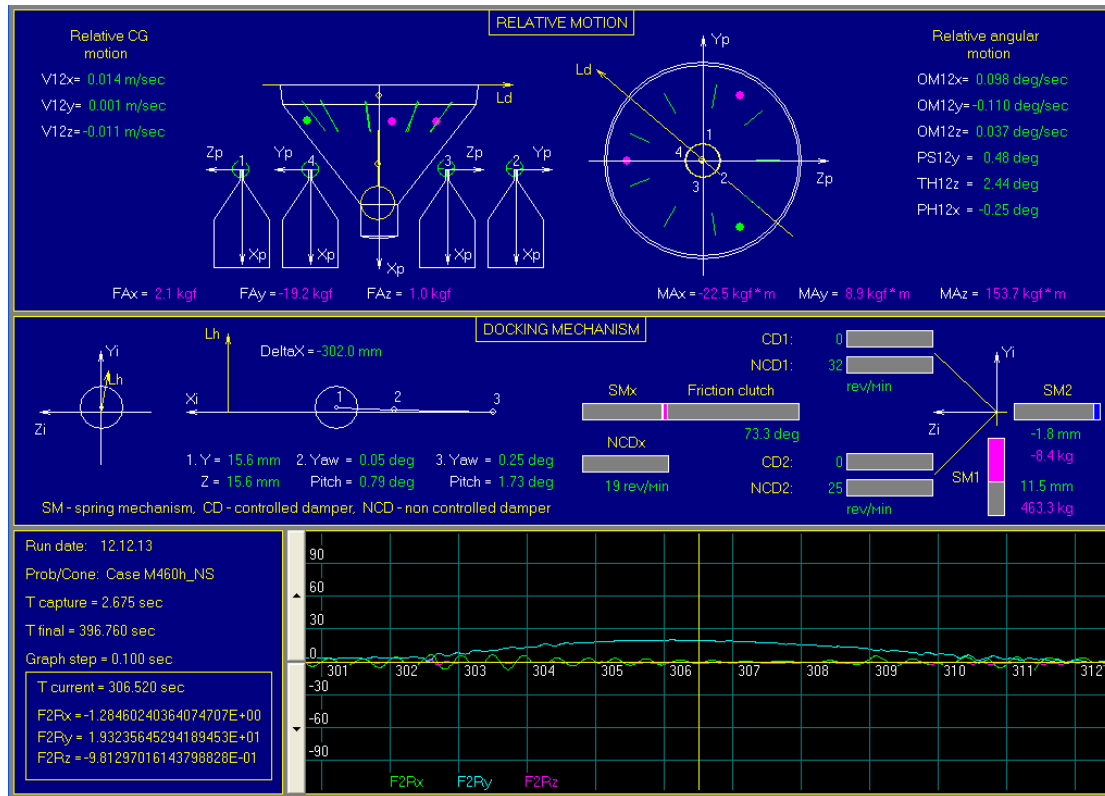
Fig.7   Appearance of images of the aligning rollers upon retraction of the docking objects.

the Russian androgynous peripheral assembly system APAS, which was used for Space Shuttle spacecraft dockings, are coupled in pairs by differential mechanisms. This provides more effective damping of relative motion energy and restriction of the docking mechanism work space. The docking ring with the guide petals acts as a buffer chain and at the same time as a controllable body of the Gough-Stewart platform (Fig. 8). It has spring mechanisms SM1-SM3 and controllable dampers CD1-CD3, which counteract lateral displacements and roll turns, and also capture mechanisms. At the basis of the platform there are the spring mechanisms SM4-SM6 and controllable dampers CD4-CD6, which dissipate the energy of the ring turns on yaw and pitch. The block of three differentials D1-D3 redistributes motion of those pairs of the kinematic chains in the least resistance direction. This leads to ring turns and improves the capture conditions upon wobbling of the assemblies. Besides, the block of differentials sort out the coordinated motion of all three pairs of the controlling kinematic chains. The energy of this motion is dissipated by the friction clutch FrC. Return angular motion of the ring upon decrease of the external load is provided by the spring mechanisms SM7 and SM8. After capture and damping of docking spacecraft relative motion energy, the drive is activated with two electric motors, Mot1 and Mot2, which moments summing up on the differential D4 feed the platform of the docking mechanism through the friction clutch and the block of differentials.

Lock clutches LC1 and LC2 of the drive prevent rotation of the electric motor shafts at the stage of absorption of relative motion energy. The electric drive can pull out the platform to the forward position for the maximal stroke of each controlling kinematic chain. This provides alignment of the docking mechanism, which is detected by the alignment sensors AS1-AS5, which are placed on the ring and in the block of the differentials. The aligned position of the platform upon its retraction by the electric drive is held by the fixators F1-F5, which are switched by the electromagnets
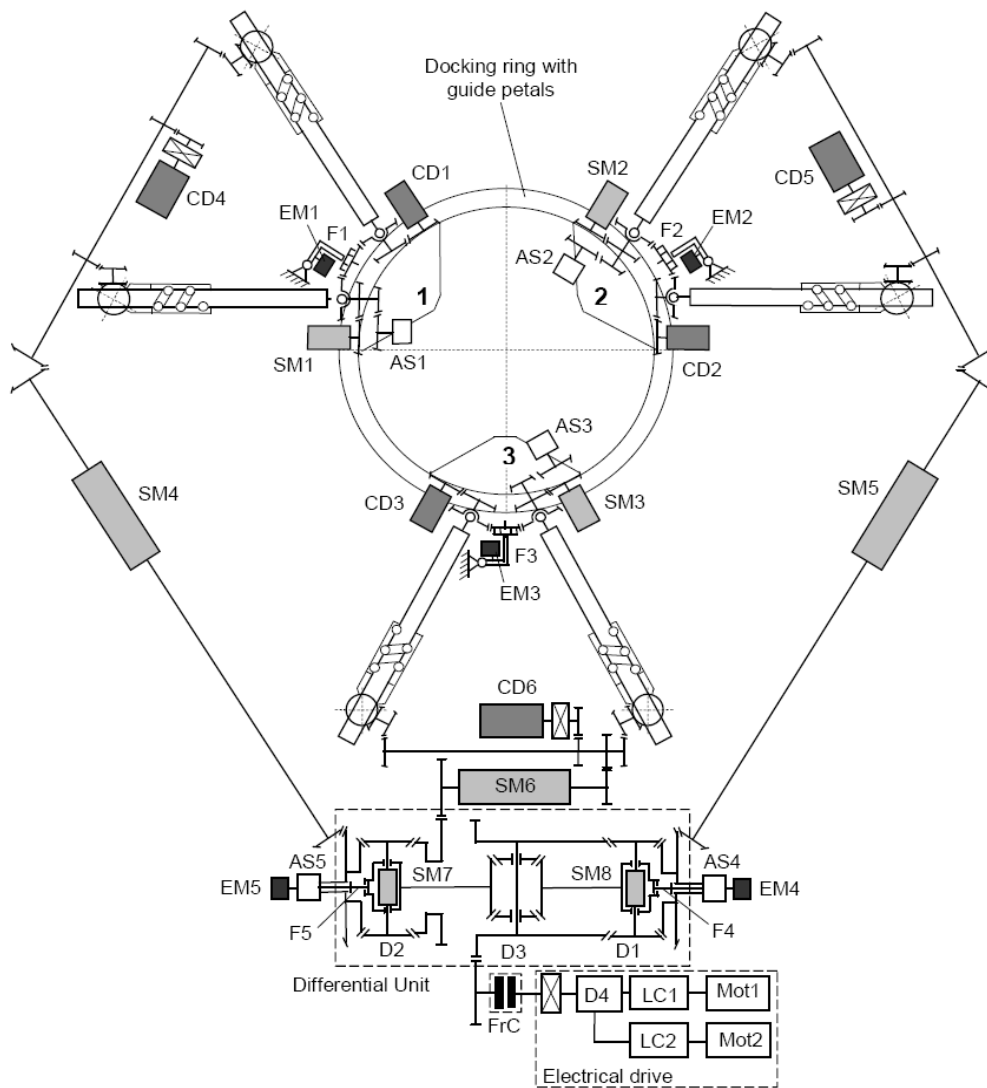
Fig. 8   A simplified kinematic scheme of the peripheral docking mechanism APAS.

EM1-EM5. A more detailed description of the differential links and the functioning of the APAS docking mechanism is given in Ref. [14]. Displacements of the active peripheral assembly ring relative to the ring of the passive assembly after capture are exclusively determined by the magnitudes of gaps and deformations. That is why the contact interaction of the active and passive rings is displayed on the dynamic diagram only before the capture event. After operation of the latches, the docking dynamics is mainly determined by displacements and deformations of the peripheral docking mechanism links, which graphical model is presented in Fig. 9.

It displays the simplified kinematics of the Gough-Stewart platform with differential connections. All the spring mechanisms, dampers, friction clutch and differential mechanisms are rotational type devices. Using their 3D models for the illustration of the docking mechanism functioning is not effective. As before, such devices are shown as vertical or horizontal bars colored with three different colors. Graphical models of the spring mechanisms and controllable dampers located on the docking ring and wireframe image of the 6-degree platform itself are positioned in the top window. Kinematic parameters of the docking ring motion relative to its initial position before the
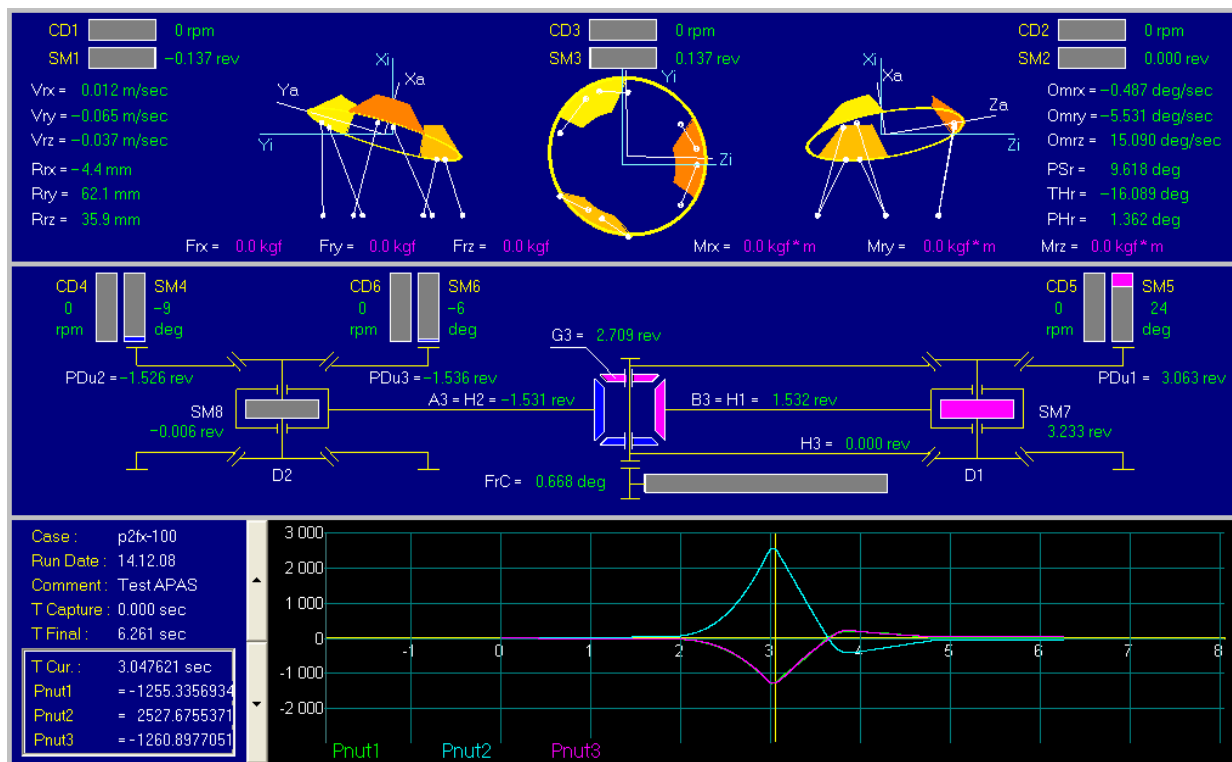
Fig. 9   Dynamic diagram of the peripheral docking mechanism APAS.

docking are also displayed there. The models of the spring mechanisms, dampers, differentials and friction clutch, located at the basis of the docking mechanism, are shown in the middle window and supplied with corresponding indications. Numerical values of turn angles and angular velocities supplement the graphical representation. The purpose and structure of the lower window are described above.

The dynamic diagram in Fig. 9 reflects modelling results of a simple test on determination of friction forces in the docking mechanism. The docking ring was manually tilted at the maximal angle by applying a force to the 2nd guide petal and then returned to the initial position under the action of the spring mechanisms. The controllable dampers were not activated. The time and trajectory of such free motion were fixed with the docking mechanism displacement sensors and with a video camera. Friction moments in the gears and rotation mechanisms in the mathematical model were selected to achieve coherence between the results of the test and the math modelling.

The docking mechanism was displaced under action of an applied external force from its initial position in different directions. This is indicated by the values of the kinematic parameters of the ring displayed in the top window. The ring turn was limited by the maximal twist travel of the spring mechanism SM7 that connects the satellites of the D1 differential. At the same time, the main wheels of the D3 differential made 1.5 turns in opposite directions. The turn angles of the other wheels are displayed in the middle window of the dynamic diagram. Deformations of the spring mechanisms SM1-SM3 are negligible due to small lateral deviations and roll rotation of the docking ring. The turn angle in the gear to the friction clutch corresponds to the gaps and angle deformations. The plots of changing of the turn angles of the nuts in the differential mechanisms that connect the pairwise controlling kinematic platform chains, are displayed in the lower window. They correspond to the average stroke in each pair of chain upon turns of the docking ring. As before, two top windows display the state of the docking mechanism in

the current time moment $T = 3.0476$ s, which is indicated in the lower window by the vertical yellow line. At the same time, the docking mechanism started to return to its initial position (external forces and moments acting on the docking ring are equal to zero).

The presented dynamic diagram allows clearly displaying the correlation between the turn angles in individual devices and the displacements of the platform of the peripheral docking mechanism from its initial position.

5. Dynamic Diagram for Analysis of Berthing

The discussed above probe-cone docking assembly was used in the operation of the MRM1 module berthing to the international space station by the SSRMS manipulator. The manipulator was controlled in the automatic-manual mode. The operator was generating required velocities of module motion using two control handles, which signals were processed by a computer into the required rotation velocities of the manipulator drives. Mathematical modelling of this operation and training of the operators were carried out on the SES (system engineering simulator) in JSC NASA [15]. A hybrid modelling using real docking equipment was implemented on the 6-degree facility of RSC "Energia" [16]. During those tests the indications of the docking system sensors, interface forces and moments, signals from the control handles and manipulator motion parameters were recorded.

The modelling results saved into the binary files were analysed using the dynamic diagram shown in Fig. 10. In its top window, the wireframe models and kinematic parameters of the relative motion of the docking assemblies are displayed. The data of the probe deformation, spring mechanisms and damper rotation velocities, usually obtained from the mathematical
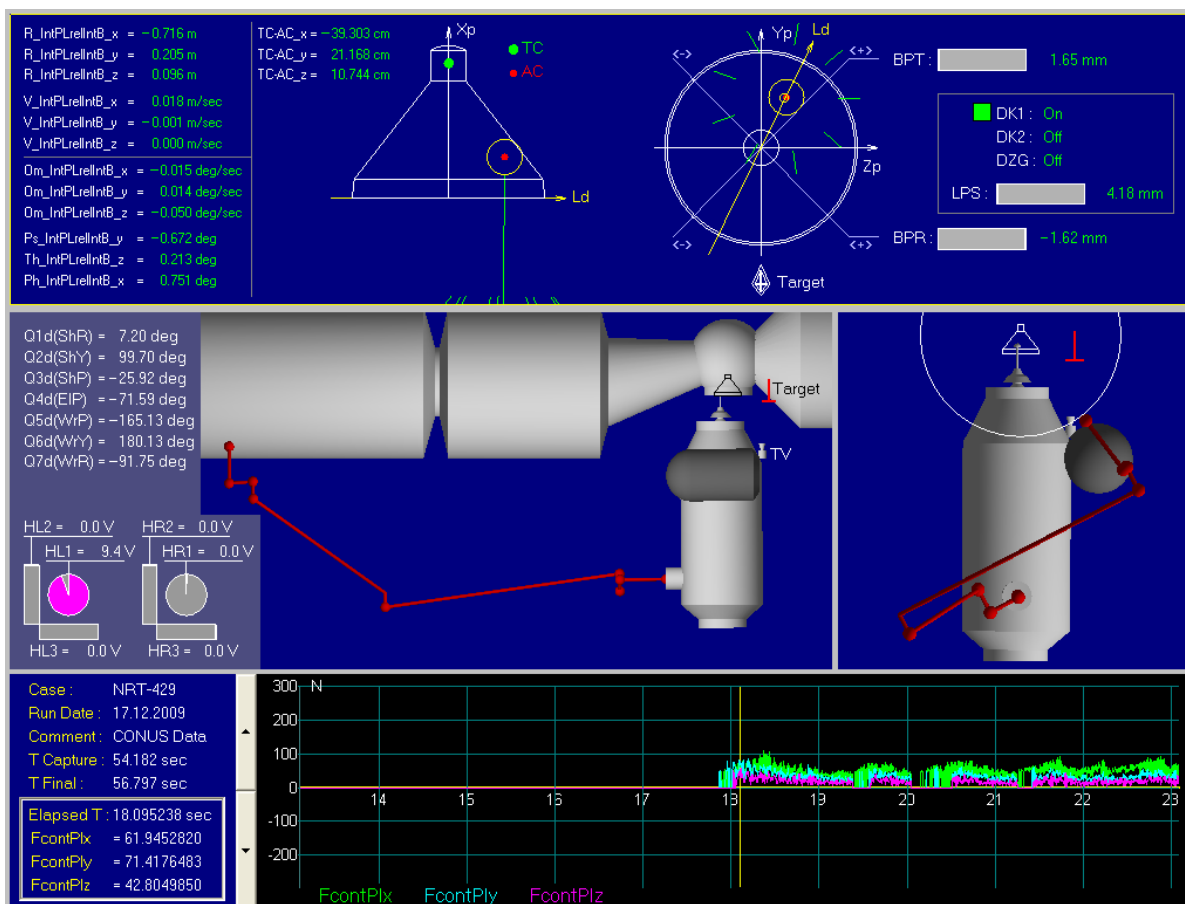
Fig. 10   Dynamic diagram of berthing with the SSRMS manipulator.

model of the docking mechanism, were absent. The position of the docking mechanism in relation to the receiving cone is calculated in the manipulator and docking module motion model neglecting probe bending. Indications of the discrete DK1 and DK2 contact sensors, DSG capture sensors and analogue BPR and BPT sensors, meaning lateral deviations of the probe head, are displayed. The aiming quality controlled by an operator is assessed by the position of the probe head center (AC point) relative to the target point—the receiving socket center (TC point).

Geometry of the manipulator and angle values in its joints, signals from the left and right control handles, which are given at the current time moment by an operator, relative position of the docking objects, assemblies, TV camera and the target are displayed in the middle window of the dynamic diagram. As before, plots of the time-dependent parameters recorded in the tests are displayed in the lower window. Fig. 10 shows forces in N (Newton) measured by the sensors of the facility. All the information changes synchronously when they are scrolling about the current time axis.

This simple geometrical model allows quick restoration and analysis of features for each specific berthing process.

6. Conclusions

The first dynamic diagram was used in 1993 for analysing docking processes with the use of APAS. Different modifications of such graphical models were further elaborated for all designed and modelled docking processes. Their application allowed better understanding of functioning of the designed mechanisms. The representation of the above described graphical models is defined not only by design principles and features of a modelled process, but also by artistic preferences of a developer or designer. Variability and quick modification of dynamic diagram

forms can be provided by specialized software development tool kits. At present, the design of the necessary data models and software tools structure is initiated.

References

[1] MSC Software, http://web.mscsoftware.com/Products/CA E-Tools/Adams.aspx.

[2] Dassault Systèmes, http://www.3ds.com/products-service /catia/capabilities/mechanical-engineering/3d-master/.

[3] LMS, http://www.lmsintl.com/DADS.

[4] PTC, http://www.ptc.com/product/creo-elements-pro/mec hanism-dynamics.

[5] CM Labs Home Page, http://www.cm-labs.com.

[6] Open Dynamics Engine Home Page, http://ode.org.

[7] Politecnico di Milano Home Page, http://www.elet.polimi. it/simecs.

[8] Universal Mechanism Software Lab, http://www/umlab.r u.

[9] V. Boikov, Software package EULER for automated dynamic analysis of multi-component mechanical systems, CAD-Systems and Graphics 9 (2000) 17-20.

[10] V.S. Syromiatnikov, Spacecraft Docking Units, Moscow, Mashinostroenie, 1984.

[11] A.V. Yaskevich, Docking systems and operations, in: G. Musgrave, A. Larsen, T. Sgobba (Eds.), Safety Design for Space Systems, Elsevier Ltd., Amesterdam, 2009, pp. 268-279.

[12] V.E. Gough, S.G. Whitehall, Universal tyre test machine, in: Proceedings of the 9th International Technical Congress, Fisita, May, 1962, pp. 117-137.

[13] D.A. Stewart, Platform with six degrees of freedom, in: Proceedings of the Institute of Mechanical Engineers, London, Jun. 1965, pp. 371-386.

[14] A.V. Yaskevich, A mathematical model of peripheral docking mechanism, Part 1: Motion equations of differential mechanisms, Mechatronics, Automation, Control 7 (2012) 63-70.

[15] Final test report for pilot-in the-loop study and berthing loads analysis for ULF4 SSRMS berthing MRM1 to FGB Nadir/NASA JSC/engineering directorate, Software, Robotics and Simulation Division, Aug. 2010, p. 109.

[16] A.V. Yaskevich, L.N. Ostroukhov, S.N. Egorov, I.E. Chernyshev, An experience of hybrid simulation tests of Russian module to ISS berthing by using SSRMS, in: Proceedings of the 7th International Workshop on Robotics for Risky Environment—Extreme Robotics, Saint-Petersburg, Russia, Oct. 2-3, 2013, pp. 244-250.

Vibration Analysis of Vehicle Floor Panel Using Hybrid Method of FEM and SEA

Kazuhito Misaji[1], Yusuke Suzuki[1], Ayumi Takahashi[1], Fumihiko Ide[2] and Théophane Courtois[3]

1. Department of Industrial Technology, Nihon University, Chiba 275-8575, Japan

2. Honda R&D Americas, Inc., Raymond 43067, America

3. autoneum, Winterthur 43 8406, Switzerland

Abstract: In order to improve the mass efficiency of an automotive soundproof package, it is important to predict the middle to high frequency range of noise and vibration during vehicle operation. A hybrid method of experimental and analytical SEA (statistical energy analysis) has been applied for the prediction of air-borne noise. However, for predicting structure-borne noise, there are no definitive simulation methods that can address the soundproof specifications in an actual vehicle. Thus, in this paper, a FEM (finite element method)·SEA hybrid method is used. The FEM·SEA hybrid method predicts structure-borne noise in the middle to high frequency range. First, we explain the basic concept of the FEM·SEA hybrid method; Second, we describe our experiment to verify the analytical results of the FEM·SEA hybrid method; Third, we provide the details of the FEM model versus the FEM·SEA hybrid model; Finally, we verify the validity and availability of the FEM·SEA hybrid method through comparisons of the FEM analysis results, FEM·SEA analysis results and measured results.

Key words: Vibration, noise, statistical energy analysis, finite element method.

1. Introduction

Electric and hybrid vehicles have grown in popularity from the viewpoint of the global environment and energy conservation. The power plant noise of electric vehicles is quiet, because an electric car is powered by an electric motor instead of a gasoline engine. In addition, the power plant noise of hybrid vehicles is quiet, because the engine noise of hybrid vehicles is reduced. A motor has a high number of revolutions, which creates high frequency noise. Soundproof packages are used as countermeasures for middle to high frequency noise. However, the addition of soundproof packages increases vehicle weight. For fuel efficiency, the mass efficiency of soundproof packages must be improved.

A hybrid method of an experimental and analytical SEA (statistical energy analysis) has been applied for air-borne noise prediction [1, 2]. However, for the prediction of structure-borne noise, there are currently no definitive simulation methods that can consider the soundproof specifications in an actual vehicle. Therefore, a FEM (finite element method)·SEA hybrid method is used. The FEM·SEA hybrid method predicts middle to high frequency structure-borne noise. In order to verify the validity and availability of this FEM·SEA hybrid method, we applied it to acoustic analysis of the dash and floor component, and roof with pillars. The analysis results of the FEM·SEA hybrid model were compared with those of an FEM model and the measured results.

This paper is organized as follows: Section 2 describes the FEM·SEA hybrid method; Section 3 explains the measurement method for the dash and

---

Corresponding author: Kazuhito Misaji, Ph.D., professor, research fields: acoustic analysis and mathematical modeling. E-mail: misaji.kazuhito@nihon-u.ac.jp.

floor component; Section 4 outlines as FEM model and a FEM·SEA hybrid model of the dash and floor component; Section 5 compares of the FEM and FEM·SEA model analysis results and the measured results; Section 6 considers the analysis accuracy of the FEM·SEA hybrid model; and our conclusions are set forth in Section 7. In this paper, we used ESI Group's VA-One.

2. FEM·SEA Hybrid Method

In this section, we describe the basic concept of the FEM·SEA hybrid method [3-7]. Fig. 1 illustrates the FEM·SEA hybrid model, which is composed of two SEA subsystems and one FEM mesh subsystem.
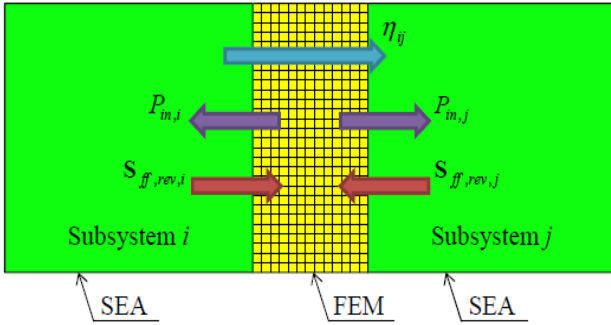
Fig. 1 FEM·SEA model.

where, η_{ij} coupling loss factor between subsystem i and subsystem j; $P_{in,I}$, $P_{in,j}$ input power to subsystem i and subsystem j; $S_{ff,i}$ $S_{ff,j}$ force acting on the FEM mesh model.

D_0 is the dynamic stiffness for the FEM subsystem; and $D_{i,dir}$ is the dynamic stiffness for the SEA subsystem. Eq. (1) is then the relation of displacement vector $\{x\}$ and force vector $\{f\}$.

$$\left[D_0 + \sum_i D_{i,dir} \right] \{x\} = \{f\} \tag{1}$$

Here, R is given by

$$R = \left[D_0 + \sum_i D_{i,dir} \right]^{-1} \tag{2}$$

S_{xx} is the power spectrum of response due to excitation in Eq. (3).

$$S_{xx} = xx^H = RS_{ff}R^H \tag{3}$$

$P_{in,i}$ is the input power to the i'th direct field related to the power spectrum of response in Eq. (4).

$$P_{in,i} = \frac{\omega}{2} \text{Im} \left\{ \sum_{mn} (S_{xx})_{mn} (D_{i,dir})_{mn} \right\} \tag{4}$$

The coupling loss factor between subsystem i and subsystem j is given by

$$\eta_{ij} = \frac{P_{in,j}}{\omega E_i} \tag{5}$$

From the coupling loss factor in Eq. (4) and the input power in Eq. (5), we obtain the SEA power balance equation in Eq. (6) [8].

$$\omega \begin{bmatrix} \eta_1 n_1 + \eta_{12} n_1 & -\eta_{21} n_2 \\ -\eta_{12} n_1 & \eta_2 n_2 + \eta_{21} n_2 \end{bmatrix} \begin{bmatrix} \dfrac{E_1}{n_1} \\ \dfrac{E_2}{n_2} \end{bmatrix} = \begin{bmatrix} P_{in,1}^{(0)} \\ P_{in,2}^{(0)} \end{bmatrix} \tag{6}$$

where, n_i, n_j—mode numbers of subsystem i, j; E_i, E_j—energy of subsystem i, j.

By solving Eq. (6), we obtain the vibration behavior of subsystem i and subsystem j.

3. Measurement Method of the Dash and Floor Component

3.1 Dash and Floor Component

In order to verify the validity of the FEM·SEA hybrid method, the dash and floor component was cut out from the white body of an actual vehicle in Fig. 2.

Fig. 2 Dash and floor component.

The vibration response of the panel was measured using a laser Doppler displacement meter. The white points in Fig. 2 are reflecting plates.

3.2 Measurement Method

The test structure was excited with a shaker applied at one of the engine sub-frame attachment points, as shown in Fig. 3. Response points were located on the rear floor, left panel, as shown in Fig. 4. There were 60 response points.

4. Analytical Model of the Dash and Floor Component

4.1 The FEM Model

Fig. 5 shows the FEM model of the dash and floor component. The FEM model had an average mesh size of 15 mm and a damping equal to 1% was used.

The excited node on the FEM model is shown in
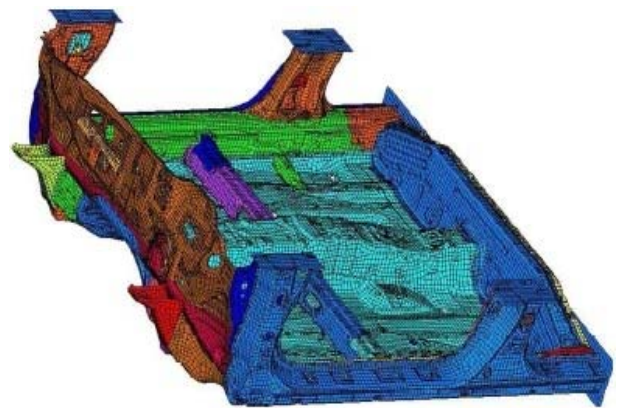
Fig. 5   FEM model.

Fig. 6. Fig. 7 shows the velocity response nodes on the FEM model. The excitation node and the response nodes were chosen to correspond, as far as possible, to the experimental points.

4.2 The FEM·SEA Hybrid Model

Fig. 8 shows the FEM·SEA model of the dash and

Fig. 3   Force point.
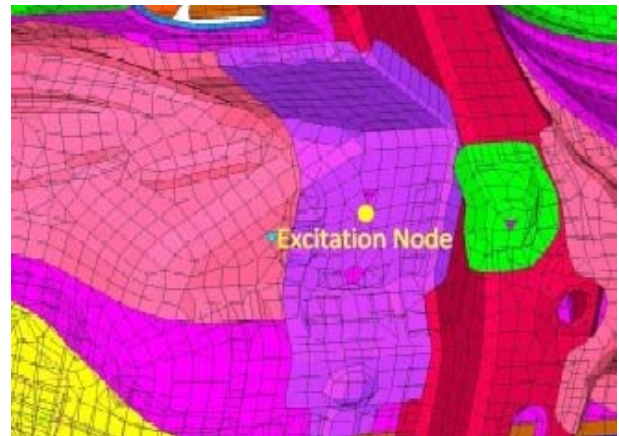
Fig. 6   Excitation node (FEM model).

Fig. 4   Response points.
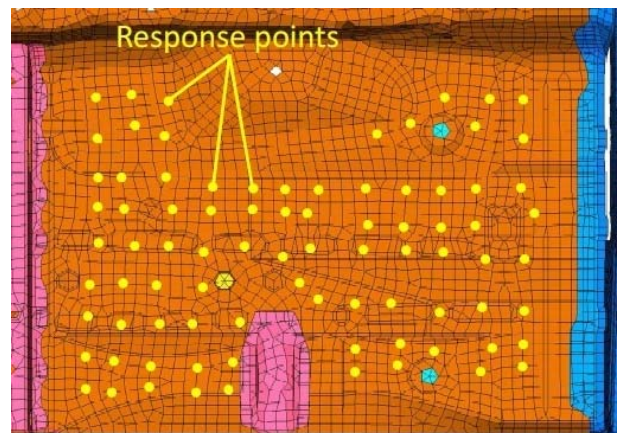
Fig. 7   Response points (FEM model).

Fig. 8   FEM·SEA hybrid model.

floor component. The flat panels of the dash and floor were modeled by SEA and the other structures were modeled by FEM. The FEM structures had an average mesh size of 15 mm and used damping equal to 1% was used. The hybrid junction between the FEM panel and the SEA panel was a line junction.

5. Comparisons of the FEM and FEM·SEA Hybrid Model Analysis Results and the Measured Results

The RMS (root-mean-square) velocity of each panel was calculated using the constructed models in Section 4. The analysis results of the FEM floor model and the analysis results of the FEM·SEA hybrid floor model were compared with the measured results.

The comparisons of the FEM and FEM·SEA hybrid model analysis results and the measured results for "Front Floor Right Inner" (Fig. 8, FrFloor R In) are shown in Fig. 9. The horizontal axis of Fig. 9 expresses the frequency and the vertical axis expresses the RMS velocity. The FEM model analysis result for "FrFloor R In" was approximately consistent with the measured result shown in Fig. 9. However, the FEM·SEA hybrid

model analysis result overestimated the FEM model analysis result and the measured result.

The comparisons of the FEM and FEM·SEA hybrid model analysis results and the measured result for "Front Floor Right Center" (Fig. 8, FrFloor R Ctr) are shown in Fig. 10.

The FEM model analysis result was approximately consistent with the measured result, as was the FEM·SEA hybrid model analysis result.

Fig. 11 comparers the FEM and FEM·SEA hybrid model analysis results and the measured result for "Rear Floor Right Outer" (Fig. 8, RrFloor R Out). The FEM model analysis result was approximately consistent with the measured result. However, the FEM·SEA hybrid model analysis result overestimated the FEM model analysis result and the measured result.

Fig. 12 compares the FEM and FEM·SEA hybrid model analysis results and the measured result for "Rear Floor Right Inner" (Fig. 8, RrFloor R In). The FEM model analysis result was approximately consistent with the measured result, as was the FEM·SEA hybrid model analysis result.
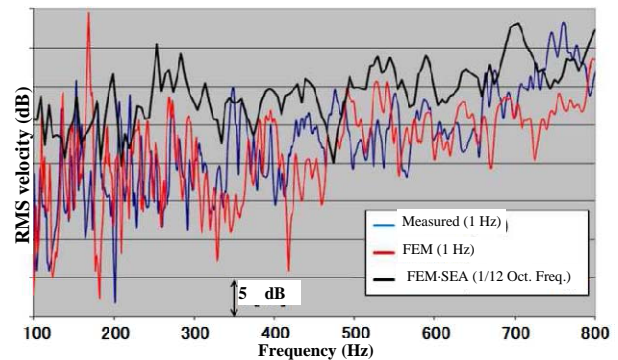
Fig. 9   RMS velocity (FrFloor R In).
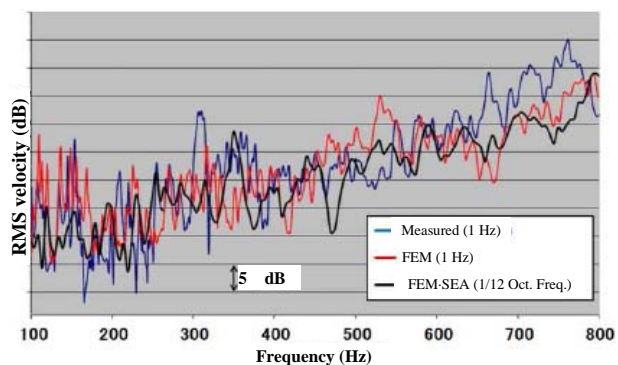
Fig. 10   RMS velocity (FrFloor R Ctr).
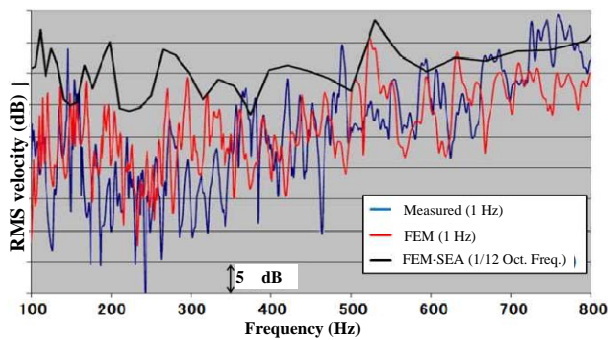
Fig. 11   RMS velocity (RrFloor R Out).
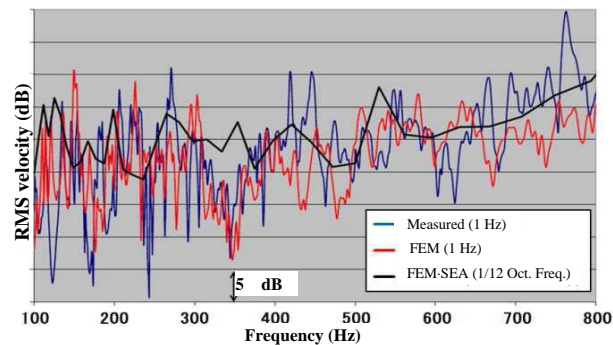
Fig. 12   RMS velocity (RrFloor R In)

The SEA panel of "RrFloor R In" can be considered to be a diffuse field because the area of "RrFloor R In" is larger than the area of other SEA panels.

6. Considering the Analysis Accuracy of the FEM·SEA Hybrid Model

The analysis accuracy for the velocities of the SEA model in the FEM·SEA hybrid model is lower than the analysis accuracy for the FEM model in the FEM·SEA hybrid model. This may be because the condition to which SEA can be applied was not satisfied. To prove this hypothesis, we created a FEM model and FEM·SEA hybrid model of the roof panel and pillars, shown in Fig. 13, because the roof panel is a diffuse field, whereas the pillars are stiff structures. The roof panels were modeled by SEA and the pillars were modeled by FEM. The roof panels were divided into two subsystems (front roof panel and rear roof panel, shown in Fig. 13). The FEM panels had an average mesh size of 15 mm and a damping equal to 1% was used.

Next, the FEM model analysis results when point force acted on the B-pillar were compared with the FEM· SEA hybrid model analysis results.

Fig. 14 shows the comparisons of the FEM and FEM·SEA hybrid model analysis results for the "Front Roof". The FEM·SEA hybrid model analysis result was approximately consistent with the FEM model analysis result.

Fig. 15 shows the comparisons of the FEM and FEM·SEA hybrid model analysis results for the "Rear Roof". The FEM·SEA hybrid model analysis result was approximately consistent with the FEM model analysis result.

Mode numbers are one of the conditions in which SEA can be applied. Fig. 16 shows the comparison of the mode numbers for the SEA subsystem (roof panel and floor panel).

There are ten times more mode numbers for the roof panel than the floor panel, establishing a condition in which SEA can be applied. From these
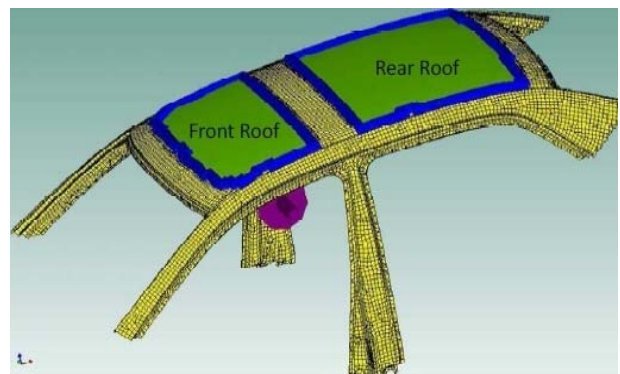
Fig. 13   Roof with pillar (FEM·SEA model).
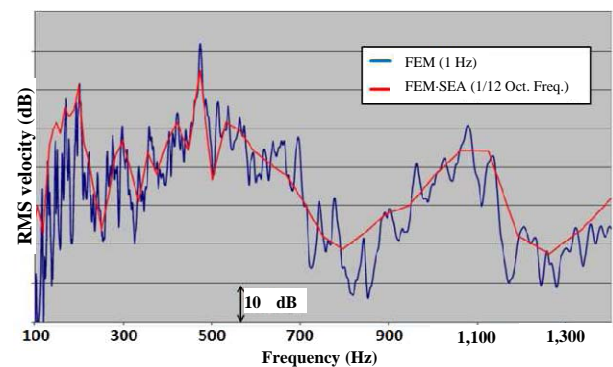
Fig. 14   RMS velocity (front roof).
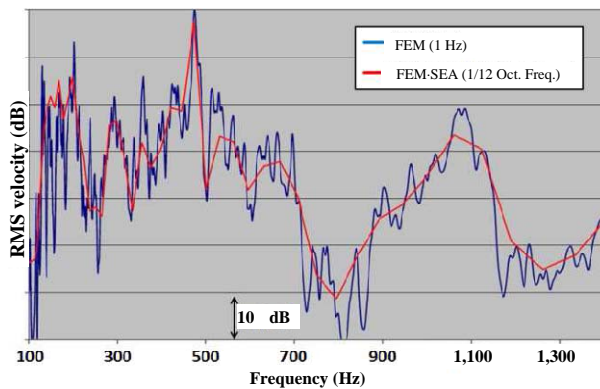
Fig. 15   RMS velocity (rear roof).
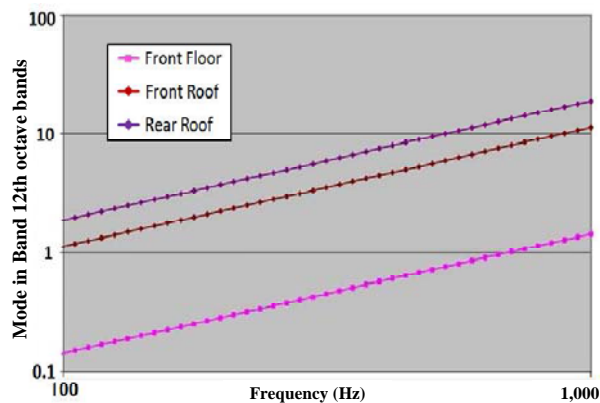
Fig. 16   Modes in Band 12th octave bands.

comparison results, we could prove that the conditions for which SEA can be applied affect the analysis accuracy of the FEM·SEA hybrid model.

7. Conclusions

The following conclusions were drawn from these results:

• The analysis accuracy for the velocities of the FEM model in the FEM·SEA hybrid model matches that of the measured and FEM model prediction;

• The conditions in which SEA can be applied affect the analysis accuracy of the SEA model in the FEM· SEA hybrid model;

• As a method of predicting structure-borne noise, we could verify the validity of the FEM·SEA hybrid method. However, we could not confirm an advantage for the analytical accuracy of the FEM·SEA hybrid method.

In future activities, we will verify the validity and usefulness of the FEM·SEA hybrid method for the acoustic cavity and soundproof package.

References

[1]   K. Misaji, H. Tada, T. Yamashita, S. Kokabu, S. Koshigoe, Hybrid SEA modeling scheme for analysis of high frequency noise in passenger cars, Review of Automotive Engineering JSAE 26 (1) (2005) 3-8.

[2]   A. Takahashi, S. Kokabu, K. Misaji, Vehicle interior acoustic analysis by a hybrid method of the experimental and analytical SEA, Journal of the Society of Automotive Engineers of Japan 42 (1) (2011) 31-36.

[3]   P.J. Shorter, R.S. Langley, On the reciprocity relationship between direct field radiation and diffuse reverberant loading, J. Acoust. Soc. Am. 117 (1) (2005) 85-95.

[4]   P.J. Shorter, R.S. Langley, Vibro-acoustic analysis of complex systems, Journal of Sound and Vibration 288 (3) (2005) 669-699.

[5]   R.S. Langley, On the reciprocity relationship and vibrational energy variance in a random subsystem at high frequencies, J. Acoust. Soc. Am. 121 (2) (2007) 913-921.

[6]   V. Cotoni, P.J. Shorter, R.S. Langley, Numerical and experimental validation of a hybrid finite element-statistical energy analysis method, J. Acoust. Soc. Am. 122 (1) (2007) 259-270.

[7]   R.S. Langley, J.A. Cordiolib, Hybrid deterministic-statistical analysis of vibro-acoustic systems with domain couplings on statistical components, Journal of Sound and Vibration 321 (3-5) (2009) 893-912.

[8]   R.H. Lyon, Statistical Energy Analysis of Dynamical Systems, Theory and Application, MIT Press, Cambridge, Massachusetts, 1975.

Advanced Industrial Engineering in Next Generation of Manufacturing Systems

Branislav Mičieta, Vladimíra Biňasová and Michal Haluška

Department of Industrial Engineering, Faculty of Mechanical Engineering, University of Zilina, Žilina 010 26, Slovak Republic

Abstract: The article deals with possible approaches to the development trends in the industrial engineering in manufacturing organizations. The authors emphasize the need for integration of advanced industrial engineering in the next generation of manufacturing systems, which responds to new trends of production, innovation and advanced technology. This integration represents a sustainable development, so that humanization of work are increased, more effective use of natural and energy resources are achieved and production costs are reduced. Trends in the products manufacturing must meet both industrial engineering as well as production management. The development trends in the industrial engineering in manufacturing organizations must use methods and tools of advanced industrial engineering to achieve competitiveness. The second part of this article deals with specification of these approaches in next generation of production systems.

Key words: Advanced industrial engineering, development trends, manufacturing enterprise, intelligent agent, autonomous control.

1. Introduction

For nowadays production organizations, it is not enough just to do things more effective. They must be unique in something. The advantage and higher chance for success could be achieved by substantial competitive advantage through innovations. Advanced industrial engineering must be able to use the opportunities of information technology and scientific methods of industrial engineering. Currently, enterprises are unable to adapt to rapidly changing market and to increasing demand requirements, therefore we focused on clarifying the possibilities for further development of today's modern techniques AIE. Industrial Engineering will be recognized as the leading profession whose practitioners plan, design, implement, and manage integrated production and service delivery systems that assure performance, reliability, maintainability, schedule adherence and

Corresponding author: Vladimíra Biňasová, Ph.D. student, Ing., research field: energy-efficient manufacturing. E-mail: vladimira.binasova@fstroj.uniza.sk.

cost control. These systems may be sociotechnical in nature, and will integrate people, information, material, equipment, processes, and energy throughout the life cycle of the product, service or program.

The profession will adopt as its goals profitability, effectiveness, efficiency, adaptability, responsiveness, quality and the continuous improvement of products and services throughout their life cycle. The humanities and social sciences (including economics), computer science, basic science, management science, highly developed communications skills along with physical, behavioural, mathematical, statistical, organizational, and ethical concepts will be used to achieve these ends. Both definitions are clearly aligned with the engineering profession as a whole. The key ingredients that make IE unique in both definitions concern the human and organizational perspectives as bodies of knowledge to be used in developing the desired systems.

In this paper, we analyze the advanced industrial engineering in next generation of manufacturing systems. The paper is organized as follows: Section 2

discusses the standard industrial engineering; Section 3 introduces the advanced industrial engineering; Section 4 introduces the holistic production system; Section 5 presents results integration of advanced industrial engineering to the next generation of manufacturing companies and future work; Section 6 gives conclusions.

2. Standard Industrial Engineering

Standard industrial engineering (Fig. 1) deals with the rationalization of production processes. The process of improving deals with the means and methods of social production in order to improve production efficiency [1, 2]. The rationalization of production includes an improvement in equipment, production processes, and the organization of labor, production, and management [3]. The rationalization of production is carried out on the basis of objectively operating laws concerning the development of technology and the productive forces as a whole. It is also influenced by the production relations of one or another socioeconomic formation with the forms of ownership of the means of production inherent to that formation [4].

The basic concepts and methods of the capitalist rationalization of production were formulated in the early 20th century by the American engineers F. Taylor, G. Emerson, and F. Gilbreth. Capitalist rationalization of production is aimed at obtaining a maximum profit for the entrepreneur, which, combined with an improvement in equipment and methods and organization of production, inevitably leads to further exploitation of the workers, an excessive increase in the intensity of labor, a deterioration of working conditions, and a rise in unemployment.

3. Advanced Industrial Engineering

AIE (advanced industrial engineering) is based on the standard industrial engineering and pursues a goal and change companies by using new methods and approaches. It deals with the implementation of these

systems and the approaches to manufacturing [5].

The significant way in advanced industrial engineering is (Figs. 2 and 3):

• The first such a significant way that can be expected in advanced industrial engineering is the development of information and communication technologies that will continue to influence all engineering disciplines, including the education of industrial engineers [6];

• The second direction is the AI (artificial intelligence) in combination with robotics create a space for the development of adaptive manufacturing [7], intelligent devices, and for the development of intelligent manufacturing systems;

• AIE will more and more move into consulting and service area at the expense of traditional production (research and development services, services related to the use of information and communication technology, management consulting, services related to enterprise management);
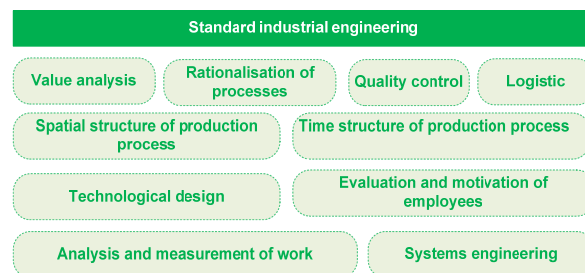
Fig. 1 Standard industrial engineering.
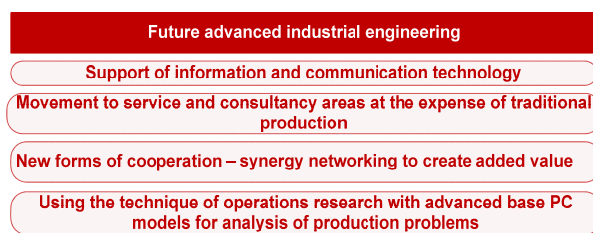
Fig. 2 Future advanced industrial engineering—Part 1.
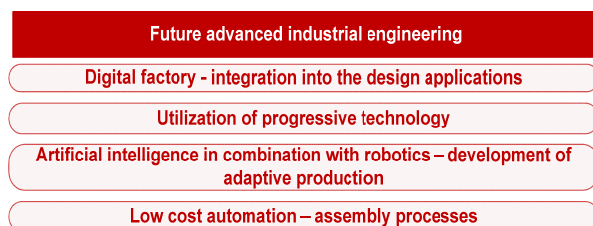
Fig. 3 Future advanced industrial engineering—Part 2.

• Significant development of virtual reality and digital factory and their integration into design applications and make process optimization in laboratory conditions and the following implementation in an industrial environment is then very fast. This is a major competitive advantage;

• Another change or direction, which is to be expected and advised him to problems AIE is a question of a new form of cooperation. They should use the knowledge of supply chain management in virtual enterprises. Get in the virtual factory knowledge of all partners to work together in future production;

• It will require a synergy of networking to create added value;

• In the future, more use of operations research techniques to advanced of the Base PC models for the analysis of manufacturing and service problems [8];

• With the expansion of e-business, companies will need more advanced and accurate techniques for predicting the outputs. These techniques are based on computer simulation [9];

• Modern IE must be able to use the opportunities of information technology and scientific methods of IE. It also must be able to work with the principles of the new Taylorism—human knowledge base and its manufacturing expertise. We also realize a new paradigm of development of industrial engineering;

• The integration of man and his knowledge base in manufacturing processes.

That's the premise of its success in the future.

If we expect new directions in relation to the technology platform that is being developed in Europe as a distinct area covers advanced industrial engineering. The idea advanced industrial engineering was well developed by the German professor Westkamper. Advanced industrial engineering is focused mainly on subgroups (Fig. 4). They form the core of the changes through which the European Union intends to increase its competitiveness [10].

Decisive role of the rapid adaptation of production is
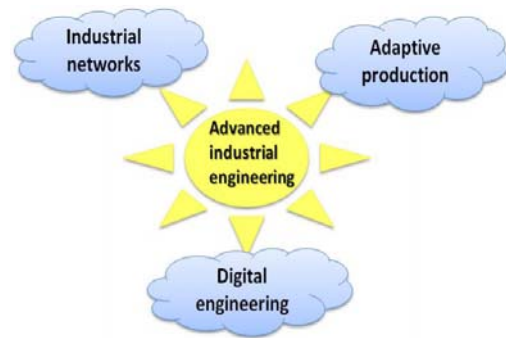
Fig. 4 Subgroups of advanced industrial engineering.

depending on the production variability and reduced the time for outsourcing. Requirement for adaptive production requires a high degree of control complexity composed into the company network.

4. The Holistic Production Systems

The systems approach is based on the view that managers should focus on the role that each part of an organization plays in the whole organization, rather than deal separately with each part. It takes into account the different needs of various functional management areas, such as production, marketing and finance. For example, the marketing department might want to be able to sell a large variety of products, while the production unit would prefer to have long production runs of a few items, and financial managers might be mainly concerned with keeping costs as low as possible. The systems approach means that managers have to discuss their various requirements in terms of the needs of the whole organization. Production scheduling, for example, would only be completed once marketing and finance were in agreement with the plans [11]. This interaction requires a high degree of communication between the various departments and functions of an organization. The emphasis is on management awareness of:

• Subsystems—the individual parts that make up the whole organization, for example a unit, department, company or industry;

• Synergy—emphasizes the interrelationships between all the parts of an organization. It also reflects the concept that the whole is greater than the sum of its

parts. This suggests that departments and units in a business are more productive when they work together than when they operate separately;

• Open and closed systems—reflect the extent to which an organization interacts with its environment. Companies providing services to the public will normally $t > e$ open systems, while those working within a larger organization, such as component part manufacturers, will be more closed;

• Boundaries—in a closed system will tend to be more rigid than those in an open system, where boundaries with the outside environments are constantly changing;

• Flows—of information, materials and human energy which move through a system and they are transformed in the process into goods and services.

The current trend in optimizing the business processes is to implement holistic production systems. In the past decade mainly individual strategies such as Kaizen, Team Work, Just in Time, etc., were adopted. But by integrating the individual strategies into a holistic system (Fig. 5), success is optimized and savings are achieved in the business process.

The organization must always be ready for the future, look for technological trends, which are perspective to include to their policies, early prepare for the development and production in order to minimize time needed to introducing of the product to market and to allow customer start using it at the right time [12]. The goal of the holistic production system is especially high added value, competitive ability and creative innovation and share knowledge in manufacturing organizations [13]. In enterprise, management are needed to be considered the methodologies, processes and governance structures that are currently in place and then are proposed measures for improvement. Management therefore addressed the role of the strategic, tactical, operational and disposition level. Transferring this holistic view on a production plant leads to main partial systems that have to be considered:
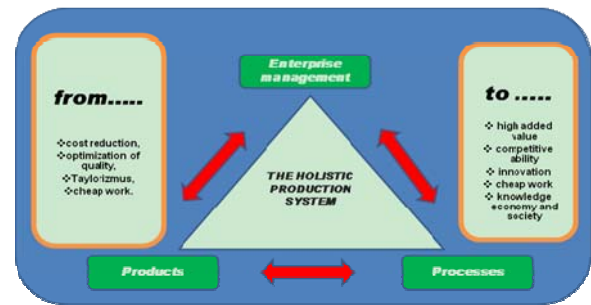
Fig. 5   The holistic production system.

product design, process planning (with interlinked machines and personnel controlled through production management), energy model (the technical building services and the building shell). Having in mind the integrated process model, all involved input and output flow result in a complex control system with dynamic interdependencies between these subsystems via different internal and external influencing variables.

5. Integration of Advanced Industrial Engineering to the Next Generation of Manufacturing Companies

Importance is placed on the ability to adjust quickly to the new production of existing requirements and the turbulent states, which may be internal or external. The aim of the system is the ability to maintain their competitiveness in the market through the production of sufficient quantities of low-cost, high products quality that meet customer demand. Due to the fact it is necessary that future generations of manufacturing companies could autonomously react to generating changes.

Enterprises need to have an integrated telecommunications network and information technology through which they can transmit the necessary information and dates within the organization [14]. Customers require specific and innovative products, which can have adverse effects on the environment (Fig. 6). Due to the fact for the development of new product platforms, it is necessary to ensure mutual cooperation with partner companies to provide the necessary knowledge to develop the new
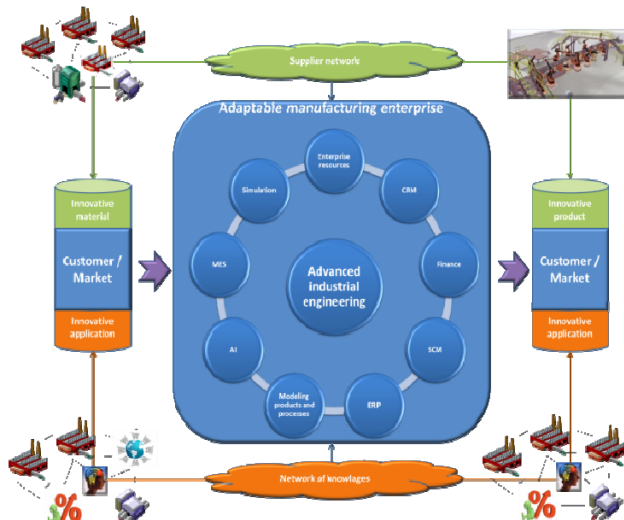
Fig. 6 Network architecture of future manufacturing enterprises.

product and solutions on base of sharing experience [15, 16]. At the same time, the intention is the development of advanced materials and new approach for analysis. Simultaneously, the customer must specify requirements through communication interface over which will enterprise obtain documents on draft products:

• Implementation of unique information technology;

• Reliable modelling, monitoring and simulation of manufacturing processes;

• Reliable detection of abnormalities;

• The sustainability of production;

• Fast reconfiguration depending on the external environment.

The development of sophisticated information technology and intelligent control of business processes is the key to the humanization of human labour. The trend will accelerate depending on the production environment. In production, it is necessary to use a number of information technology with support of digital engineering (control systems), modelling and monitoring systems.

In view of turbulent external environments, it is requires a high complexity of supply chain management, which affect the development of software platforms for enterprise resource planning,

management of finances and time efficiency performance the contracts.

5.1 Digital Manufacturing

The turbulent market and global competition affect the requirement for shorting innovation cycle. As a result of aspects and complexities of inter-network, cooperation causes the growing numerous of enterprise tasks. Disposition of product models allow more simultaneous realization of product development and manufacturing [17]. By the way, it will reduced construction time of the required dose and it is possible to performer simulation procedures.

Digital manufacturing (Fig. 7) provides effective support to business process in manufacturing companies. New product development and meeting deadlines of orders forms an essential application area of supporting tools for digital production.
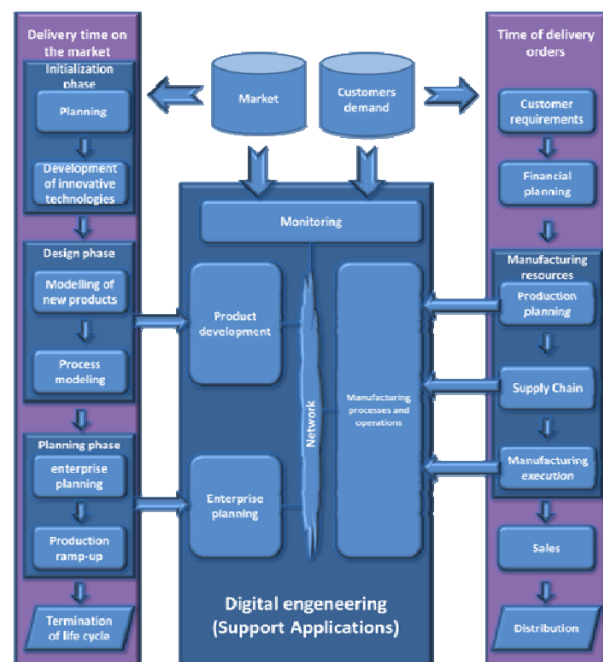
Fig. 7 Digital manufacturing in enterprises processes.

5.2 Integration of Artificial Intelligence

In an enterprise-wide system, it should integrate an artificial intelligence that ensures autonomous tasks directionally through the agent communication.

Individual agents can transmit tasks and in the frame of interactive activities conduct evaluation activities. Mutual communication is based on priority rules for the realization the current transformational needs of the defined roles in meeting of corporate goals. To build adaptable manufacturing enterprise with embedded intelligence, the key technology is needed, which can be achieved through the establishment of transparent agent's infrastructure.

Intelligent control mechanism should ensure the transfer of data and information which subsequently performs analytical procedures, evaluation action and remedial activities (Fig. 8). The aim of the integrated control system is the sustainability of the production company in a competitive environment, which includes the prerequisites.
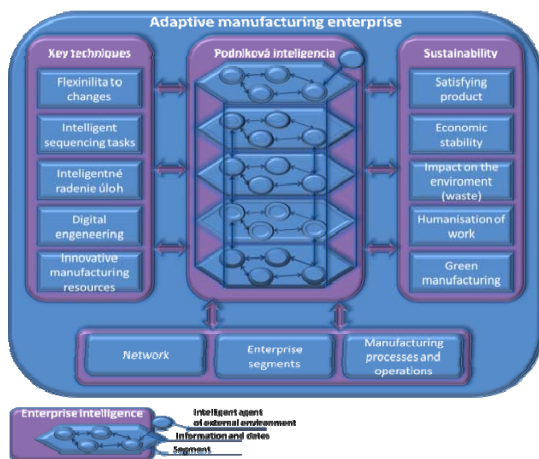
Fig. 8   The integration of artificial intelligence into enterprise infrastructure.
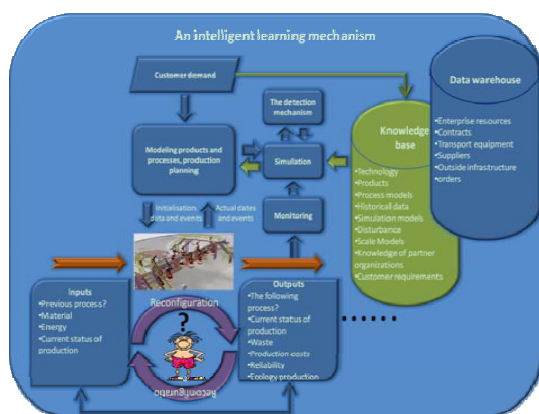
Fig. 9   Intelligent learning mechanism of manufacturing resources.

5.3 An Intelligent Learning Mechanism

The mechanism is designed to educate the manufacturing facility for the purpose of autonomous operation (Fig. 9). The emphasis is on acquiring knowledge from external and internal environment, which is necessary for optimization the design of products, manufacturing processes, operations and production plan [18, 19]. Output parameters are monitored by the sensory disposition which converts the signals into actual data values and initializes activity of detection mechanism for detect abnormalities through simulation model. The increasing complexity of system architecture may result in adverse effects on the autonomous control system tasks and system reliability. In view to the fact that manufacturing or assembly system must be equipped with reconfigurability, which provide quick configuration of maintenance system and switch generating variants by switching generating tasks depending on the need of production of a particular family of work pieces and subassemblies parts by adding or removing functional elements.

The purpose of the reconfiguration is to change system functionality and ensure the scalability of production capacity. Through reconfiguration activities can independently add, delete, modify and convert machines (handling units) based on rapid response to changing requirements and the actual behaviour of the system. System with given ability may increase life of production and should offer a cost-beneficial solution in the long term.

6. Conclusions

In conditions of the debt crisis is necessary to promote advanced industrial engineering, which is leading to greater efficiency, reducing environmental impact, achieving a more efficient use of natural resourcing and production costs. Advanced industrial engineering cannot function without the excellence industrial engineers. As a result of the competitive struggle it is necessary for existing enterprises rapidly

and flexibly adapt to the changing requirements of the current market environment. Through approaches AIE. In view of the fact it is necessary to rebuild the thought architecture of today's manufacturing companies.

References

[1] M. Gregor, M. Bugan, M. Botka, Goals and metrics within lean manufacturing, in: InvEnt 2006, Strečno, 2006.

[2] M. Rakyta, P. Bubeník, The economic crisis, the time to develop new approaches of technological development, Technique: Magazine of Industry, Science and Technology 8 (5) (2010) 50-51.

[3] M. Gašo, H. Tureková, Management of innovation projects, in: InvEnt 2009, Žilina, Jan. 24-26, 2009.

[4] L. Dulina, M. Bartánusová, Ergonomics and preventive medicine in companies in Slovak republic and the EU, in: 2nd International Conference on Ergonomics, Zagreb, 2013.

[5] B. Mičieta, H. Tureková, Innovation management: support for creating of innovations, in: InvEnt 2010, GEORG, Žilina, 2010.

[6] P. Magvaši, M. Gregor, Advanced Industrial Engineering and Quality of Industrial Enterprises, Technická Univerzita, Košice, 2013, pp. 38-42.

[7] B. Borsíková, B. Jelenčík, I. Meňovský, Post-Crisis Trends in Personnel Management, RAABE Slovensko s.r.o., Slovakia, 2010.

[8] J. Staszewska, J. Barglik, R Considerations on the Cluster Concept As A Tool Improve the Efficiency of the Logistics Process, Politechnika Śląska, Poland, 2008.

[9] R. Kohár, S. Hrček, Dynamic analysis of rolling bearings with elastic cage, in: Proceedings of the 54th International Conference of Machine Design Departments, Hejnice, Czech Republic, Sept. 10-12, 2013, pp. 211-216.

[10] M. Krajčovič a kol., Intelligent Manufacturing Systems in concept of digital factory, Communications: Scientific letters of the University of Žilina 15 (2) (2013) 77-87.

[11] E. Slamková, Ľ. Dulina, M. Tabaková, Ergonómia v priemysle, Ergonomy in industry, in: InvEnt 2010, GEORG, Žilina, 2010.

[12] A. Mičietová, M. Čilliková, Technology—Machining, University of Zilina, Žilina, 2009.

[13] A. Mičietová, M. Čilliková, J. Salaj, Influence of some selected factors on surface quality when cutting by plasma and laser beam, Journal of Machine Manufacturing: Design and Manufacturing 49 (E3-E5) (2009) 104-106.

[14] Z. Bi, Revisiting system paradigms from the viewpoint of manufacturing sustainability, Sustainability 3 (2011) 1323-1340.

[15] J. Su, Component-based intelligent control architecture for reconfigurable manufacturing systems, Ph.D. Thesis, Virginia Polytechnic Institute and State University, 2007.

[16] V. Vyatkin, Function Blocks for Embedded and Distributed Control Systems Design, ISA, New Zealand, 2011.

[17] D. Mavrikios, N. Papakostas, G. Chryssolouris, D. Mourtzis, G. Michalos, K. Georgoulias, Digital manufacturing: History, perspectives, and outlook, Journal of Engineering Manufacture 223 (5) (2008) 451-462.

[18] V. Botti, A. Giret, A Multi-agent Methodology for Holonic Manufacturing Systems, Springer, London, 2008.

[19] A. Geyer, The challenge of sustainable manufacturing, in: International Summer Academy on Technology Studies—Corporate Sustainability, IPTS, 2010.

Structural Aerospace Composite/Metallic Samples under Fatigue Loads: Experimental Activity on Three Case Studies

Giacomo Frulla and Giulio Romeo

Department of Mechanical and Aerospace Engineering, Politecnico di Torino, Torino 10129, Italy

Abstract: The use of composite materials in aerospace engineering is ever increasing. Properties such as low weight, high performance, high stiffness and the ability for it to be tailored specifically for different structural uses has increased its importance in recent years. Specific experimental/numerical activities were developed in the last decade at the aerospace department of Polito and are under consideration in recent years regarding the analysis of fatigue behavior of composite/metallic structural samples under cyclic loading condition. A review of the main significant results connected to three case-studies is presented in the paper. The first is related to the definition and analysis of innovative joint for composite high aspect ratio aircraft structures. The modular design oriented to limit component dimensions for transportability requires the presence of a removable joints able to overcome the typical low bearing failure level of composite pin-loaded joint under static and fatigue loading distribution according to airworthiness requirements. The static experiments demonstrate the consistency of the proposed advanced joint configuration that postpones the joint failure to high load level according to the structural requirements. The cyclic loading phase takes as reference point the failure load of the initial configuration and defines a loading cycle with a maximum higher than the failure load of the initial configuration. The fatigue behavior of the advanced joint also demonstrates a substantial consistency with expected duration of 1e6 cycles as required by the structural design for operating reasons. Specific indication on fatigue limit with respect to critical amplitude is reported. The second is related to the presence of specific damaged situation in thin-walled flat/stiffened composite plate. Stiffened configurations are frequently used to increase buckling load level. Unexpected events on solid/stiffened composite panels can introduce a certain level of damage, typically delamination, that can cause reduction in buckling design level and reduction in global strength. The presence of cyclic load and fatigue effect can have an important consequence on damage propagation and structural integrity. The damaged area determined by the skin-stiffener de-bonding of a certain dimension is investigated under static compression and cyclic compression. Local buckling of damaged area is determined and pointed out by tests in uniaxial compression. The experimental static behavior points out the presence of a snap-effect during loading and un-loading. Fatigue loading configuration is applied in the range of post-critical local configuration considered as the most effective situation. Preliminary fatigue results are presented and discussed. The third is related to preliminary investigation on the effect of fatigue life reduction of 2024 Al alloy in corrosive (exfoliation) environment. The effect of corrosion is taken into consideration introducing specific concentration factors into the life estimation relationship. Differences between fatigue in prior corroded specimens and fatigue in presence of corrosive environment are emphasized. No crack propagation is considered. Related concentration factors are derived and compared by the few experimental results in order to define some guidelines for design process and to improve aircraft better evaluation of component structural integrity in operative situations. A preliminary approach is presented in the paper in order to correctly identify the contribution of corrosive environment in coupled fatigue loading phase. The results are discussed and future improvements are suggested.

Key words: Aerospace structures, composites, fatigue, corrosion, experimental activity.

1. Introduction

The presence of composite materials in aerospace

Corresponding author: Giacomo Frulla, Ph.D., associate professor, research fields: aerospace structural design and construction, composite and aeroelastic analysis of slender structures. E-mail: giacomo.frulla@polito.it.

engineering applications has grown steadily in recent years. Tailoring characteristics and properties such as low weight and high strength/stiffness have pushed the designer to their introduction in high performance structural configurations and challenging components.

Integrated manufacturing processes have reduced the presence of traditional joining methods with some advantages in assembling procedures, weight and maintenance. On the other hand, more efforts have to be dedicated in the investigation of the effect of new types of anomalies, defects and different behavior of such structures under loads. Since the behavior of composites is quite different if compared to the traditional aerospace metals, the knowledge of their behavior in specific different situations, in which different problems could arise, has been required. Specific activities have been developed at the aerospace department of Politecnico di Torino in order to give a contribution to a better understanding of the behavior of composites in different structural configurations.

Fatigue behavior of simple composite/metal samples, that are representative of operating configurations, has been studied by means of analytical/numerical approach and experimental correlations. The paper gives an overview of the main significant results that have been obtained during the activity cited above. The activity has been focused on the following three case-studies: (1) design and analysis of an advanced joint for composite high aspect ratio aircraft structures; (2) the presence of specific damaged situation in thin-walled stiffened composite plate; (3) a preliminary investigation on the effect of fatigue life reduction of 2024 Al alloy in corrosive (exfoliation) environment.

2. Innovative/Advanced Joint Results

The huge dimension of innovative HALE (high altitude long endurance) aircraft [1, 2] needed the application of advanced composites in order to cope with their specific stringent weight/strength requirements. High aspect ratio structures for such kind of aircraft required a "modular" design both because of manufacturing limits and for transportability reasons. Two methods are frequently used in assembling different "modular" elements: bonded joints and mechanical fastened joints. The first is preferred when

the members remain connected during the whole operating life. The second is preferred when the members have to be disconnected for inspection, transportation and so on, as in the present case. The main requirements of such a removable platform connections concerned: (1) transmitting of loads between different primary structural parts of the wing spar with a sufficient safety level according to the normative; (2) guaranteeing of fast assembly and dismounting without any permanent effects on the materials; (3) positioning of the connected structural parts with the correct clearance. Removable connections succeed if mechanical bolted joints are used, but, in the case of composite structures CFRP (carbon fibre reinforced plastic), the joint has to be properly designed to reach the maximum bearing failure level and in order to avoid net-tension, shear-out or cleavage failures. The introduction of a bolted joint connection in composite aircraft primary structures reduces the load carrying efficiency of the structure by around 50% even when the joint has been properly designed and manufactured [2-5].

The definition of an advanced joint able to overcome the indicated weakness and increase the strength was considered in innovative aircraft design [4, 5] and summarized in this section. An experimental assessment on the static properties of the advanced joint was reached by means of a test campaign [4, 5], while some fatigue experimental results were obtained in order to have a validation of the behavior of the advanced configuration in assumed operative condition. The considered joint configuration, as reported in Ref. [5], is a pin-hole connection based on a solid or sandwich CFRP laminate with the same lay-up. The laminate is reinforced with two 80 mm external diameter steel flat plates, and an internal connected cylindrical appendix which provides the loading transmission and the pin site (20 mm in diameter). A UD (uni-directional) M40J/epoxy material was used with the following mechanical properties: $E1 = 215$ GPa, $E2 = 66.7$ GPa, $G12 = 4.303$ GPa, $nu12 = 0.27$.

A 9 mm thick core of standard Rohacell 51 rigid foam reinforced with micro-spheres was inserted into the sandwich configuration. The laminate orientation was chosen in order to obtain maximum bearing strength [4] with the following percentages: 25%(UD ± 20), 25%(UD90) and 50%(UD ± 45).

More details can be obtained in cited references. The joint was adapted for installation in the main tubular spar of the Heliplat prototype structural connection, as reported in Fig. 1a [2, 3], for transmitting the load in a shear-bearing way. The preliminary joint static performances were assessed during the full-scale shear bending tests performed on the prototype. Satisfactory static behavior [2] was obtained. The definition of the joint as the main connecting element in Heliplat prototype has pointed out the necessity of a preliminary evaluation of its fatigue behavior. A fatigue test campaign has been arranged on advanced configuration. The test equipment consisted in a typical load/displacement tension-compression machine (100 kN max) with both static and fatigue capability. A fixed frequency and constant amplitude sinusoidal load (10 Hz), assessed in Ref. [4], has been applied to each test sample up to about 10^6 cycles (EL) or until failure.

2.1 Static Behavior

Typical static test results are summarized in Table 1 as derived from Refs. [4, 5]. Typical static failures are shown in Figs. 1b and 1c, as a confirmation of previous described criticality of CFRP joint: an important degradation of the contact area due to bearing failure is evident. The new advanced joint configuration postpones the failure to higher loads in a static tension failure mode as expected from the design. The simple configuration demonstrates a very poor capacity to overcome the typical 20 kN pin load (solid) even though the joint has been correctly designed in order to avoid net-tension/shear-out failures and to maximize the bearing strength with a specific lay-up. The average failure load of the pure composite joint is about 20,481 N in the solid case and about 39,481 N in the sandwich

(a)   (b)   (c)
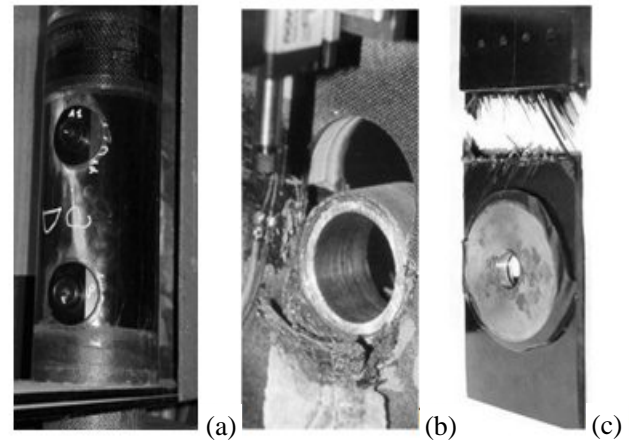
Fig. 1   (a) Heliplat prototype joint configuration; (b) failure mode for initial configuration; (c) failure mode for advanced configuration.

Table 1   Static results for solid and sandwich (S.s.) configuration (A = advanced; ave = average; not-A = initial).

Solid	(not-A) /ave	(A) /ave	(not-A) /(A)
a	1.041	0.996	0.227
b	1.045	0.993	0.229
c	0.914	1.011	0.196
S.s.	(not-A) /ave	(A) /ave	(not-A) /(A)
d	0.996	0.996	0.401
e	0.950	1.006	0.379
f	1.054	0.998	0.424

one. The advanced configuration average failure load is about 94,267 N for the solid case and 98,363 N for the sandwich case, with a slight difference due to possible manufacturing imperfections.

2.2 Fatigue Behavior

Fatigue tests and fatigue results are summarized in Table 2 [5]. Five sandwich samples are considered in this case. The definition of fatigue properties cannot be obviously based on only five samples. However, it is possible to point out some design indications useful for the Heliplat prototype. The average fatigue load has been maintained constant for each test and close to, or higher than, the static failure load for the pure composite sample, while the maximum load has been assumed higher. The first three samples have been subjected to quite homogeneous conditions (average

Table 2   Fatigue results on sandwich configuration.

	P^*_{max} (N)	R^* (P^*_{min}/P^*mx)	Ra (P^*a/P^*mx)	Note (Cyc./EL)
Ave on three	4.78e4	0.55	0.23	Run-out
N-11bs	4.23e4	0.23	0.39	Failed-ST (0.634)
N-3bis	4.17e4	0.25	0.38	Failed (1.44)

load and amplitude) with a mean loading ratio R^* of about 0.55. The other two failed samples have given one critical load combination with a mean R^* parameter of about 0.24. These loading conditions followed the preliminary design indications in order to check the joint fatigue limits. One specimen was tested under a ST (step test) condition. The failure load amplitude ratio ARL (ALR = Pa/Pu, Pu being the average static failure load and Pa the amplitude) was empirically determined of about 0.16 [5]. The same ARL, applied to a second sample (N-3bis—the same condition) has confirmed the preliminary assumption. The amplitude load ratio vs. the MLR (maximum load ratio) is presented in Fig. 2a. It is possible to note that, for an R^* value of about 0.24, a conventional fatigue limit is reached for ALR of about 0.16; while for $R^* = 0.55$, ALR = 0.1 can be considered to be under the fatigue limit. The load amplitude that produces failure is close to 15 kN with an average of 26 kN. It is interesting to observe that no failure is obtained for a load amplitude of about 10 kN, even though the average load is about 1.5 times the previous one. The experiments have confirmed the expected joint endurance under operating condition. A typical fatigue failure of the reinforced specimen is reported in Fig. 2b. A de-bonding of the adhesive on the two faces in the upper part of the reinforcement, without apparent separation of the carbon layer (except in the short part near the hole edge) and a net-tension failure at the hole edge sandwich faces can be observed. A first ply failure can be observed near the hole edge, probably induced by a local concentration, as the reinforcement loses its loading distribution effect after cycling. A degradation in the adhesion properties could also have occurred with cycles together with not perfect hand-bonding of the junction.

(a)

(b)
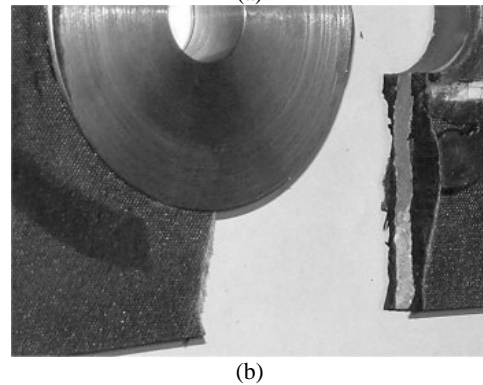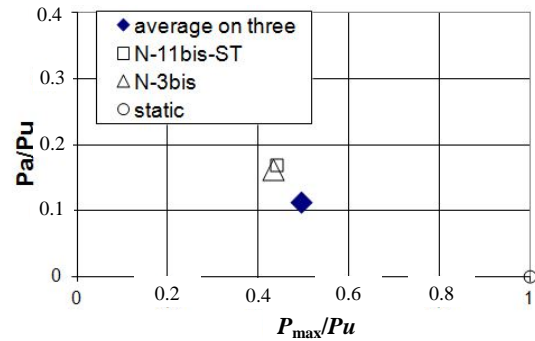
Fig. 2   (a) Fatigue results for sandwich samples: amplitude load ratio vs. maximum load ratio; (b) Failed sample.

3. Damaged Stiffened Plates Loaded by Cyclic Compression

The behavior of composites in the post-buckling regime, especially with occurrences of delamination and micro-cracking, is still not very established connected to the presence of cyclical loading and fatigue effect on damage propagation and structural integrity [6, 7]. Delamination is one of the most common damages in laminated composites that may occur due to different reasons, such as low energy impact, manufacturing events, high stress concentrations or material discontinuities (free edge effects, etc.). Delamination is known to degrade the overall stiffness and strength of the structures, severely reducing the load-carrying capacity of the laminate under compressive loads [8]. A skin delamination or a stiffener de-bonding in a stiffened panel can cause buckling prior to the designed critical condition. The ability to evaluate this effect is essential for predicting composite performance and developing more safe/reliable structures [8, 9]. Stiffening concepts are

used to increase buckling characteristics of a thin plate. Several type of buckling have to be taken into account such as: overall buckling, skin buckling, stiffeners buckling and torsional or twisting buckling [9, 10]. Local/global critical behavior is modified as a damage effect in terms of de-bonding between skin and stiffeners, delamination between skin layers and between stiffeners layers and so on. In these cases it is important to assess and characterize damage, as well as how to identify the progression of damage and the convenient design procedures.

Experimental activity is fundamental in this phase due to the nature of different empirical coefficients included in typical Paris-law formula. On this basis, an anisotropic stiffened panel has been arranged and tested under static compressive loading and fatigue. The presented results are derived from Ref. [11] and summarized here as a first step analysis of the fatigue behavior of this configuration. A flat panel with four T-type stiffeners has been prepared with stiffener width and height of 30 mm. M40/epoxy material with standard properties and the following laminate lay-ups are introduced: $[(\pm45)2/0/(\pm45)/90]S$ for the panel, $[(\pm45)2/06/(\pm45)/0]S$ for the stiffener cap and $[(\pm45)2/06/(\pm45)/05]S$ for stiffener web.

Panel average thickness of 2.8 mm is determined. Overall panel dimensions, 1,000 × 700 mm, were reduced according to the assumed clamping condition adopted for the experimental phase (Fig. 3a). The panel was designed with an artificially induced damage consisted in a skin-stiffener de-bonding that was assumed to be critical for stiffened structures.

Damage position and dimension was chosen according to preliminary numerical analysis [11]. Several SG (strain gages) are bonded back-to-back along mid-line and quarter-line panel position. Fig. 3a shows the stiffened plate side while SG positions are reported in Fig. 3b. Dashed and dotted lines indicate damage (253 mm wide) position and back SG position respectively. Uniaxial and Bi-axial static loading cases were previously analyzed by FE and compared to

(a)

(b)

(c)
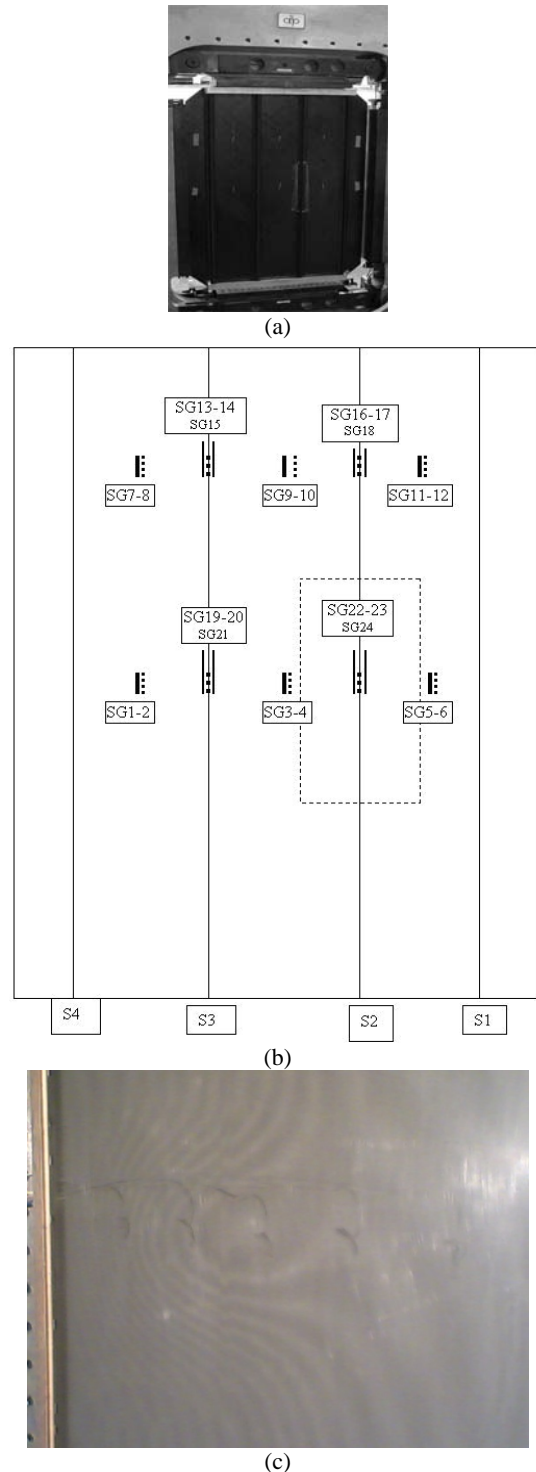
Fig. 3 (a) Damaged panel (stiff-side); (b) SG (strain-gage) scheme; (c) Experimental local buckling.

undamaged situation in order to determine strain distribution under critical and post-critical (local-global) conditions [11, 12]. See Ref. [11] for more details. Few static results for the uniaxial

compression are collected in Fig. 4a. It is possible to see that the skin-stringer de-bonding induces a local buckling on the skin portion at a load level lower than the global critical condition. The experimental curves also demonstrate the presence of a snap-wise behavior of the damaged portion, probably due to interaction with global deflections/imperfections. Fig. 3c presents the local buckle as experimentally determined.

A low frequency (0.1 Hz) compressive loading condition has been performed in order to evaluate damage behavior. The load cycle is characterized by a maximum load ratio of about 0.6, a minimum load ratio of 0.5 and an amplitude of 0.05. The cycling curves follow the "after snap" path as indicated during static phase. A first loading phase is presented in Fig. 4a showing the "snap" effect at about 0.52 load level ratio. The damage buckling is quite evident following SG24 curve. The SG5, SG6 and SG24 are retained during fatigue test as the most representative of the situation.

The preliminary analysis of experimental strain behavior is reported in Fig. 4b in not dimensional form. Fig. 4b presents the initial detected data after cycling. The damage demonstrates an increase in post-buckled local strains after cycling probably due to damage growth. The analysis of the fatigue results is in progress following the previous one as in Ref. [11]. More updated details are reported in Ref. [13].

4. Fatigue Behavior of Al-Alloy in Corrosive Environment

The so-called "life extension" programs are becoming of interest between big aerospace companies and main end-users as a consequence of investment reduction in developing new generation aircrafts. This means that the aircraft fleet has to be maintained in operations with an increased service life with respect to the designed one. Only the most recent designs have incorporated significant improvements in corrosion prevention and control in design and manufacturing [14]. The ability to maintain the requested efficiency is based both on the upgrade of avionics equipments and

Experimental behavior—uniaxial

(a)

Fatigue behavior

(b)
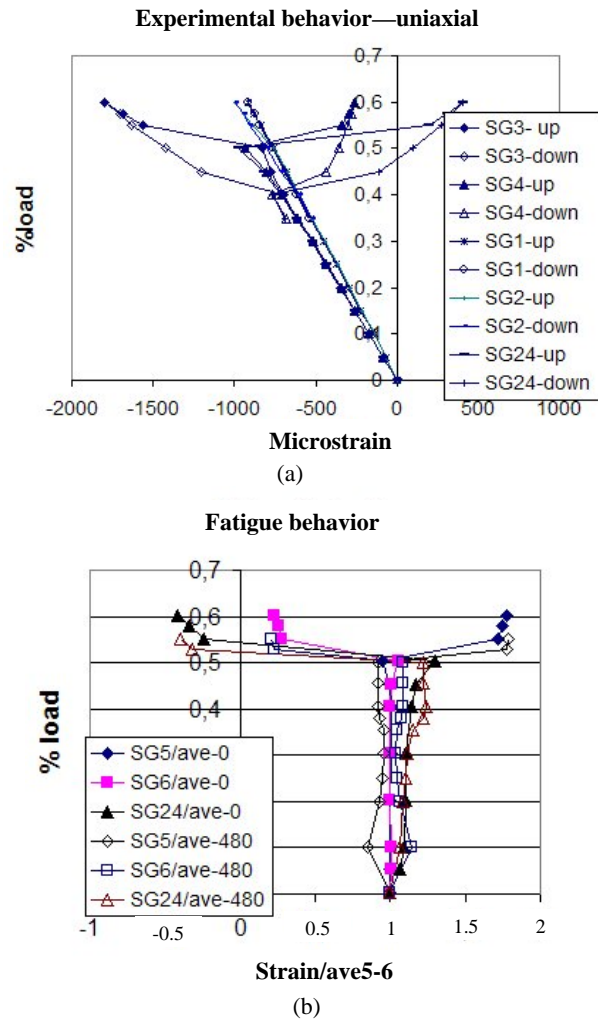
Fig. 4   (a) Experimental static snap results; (b) Experimental fatigue behavior (SG 5-6) at different number of cycles.

with the application of specific structural maintenance plans in order to cope with "ageing". The problems connected to structural aircraft ageing can be considered as a combination of: (1) fatigue (operational use); (2) corrosion (environmental conditions); (3) wear (operating cycle and usage time). They can be present sometime alone but more commonly in dangerous combinations such as corrosion and fatigue. In this particular case, the well known fatigue effect can be superimposed to the effect of hidden corrosion due to the operating environment. A better understanding of such combined effect results in a more rational approach to the management of aircraft/component life [15, 16]. Fatigue load due to

operating envelope acts on a damaged structure combining with corrosion and producing unpredictable effects on structural integrity especially if components are positioned in not easily accessible point for inspections. The combination of such two effects tends to be different from the simple application of fatigue on prior corroded parts.

A preliminary experimental investigation is summarized in the paper referring to the activity partially developed in Ref. [17] and continued in Polito-lab, in order to point out few main trends about the fatigue/corrosion combination on a typical 2024 Al aerospace alloy, in particular when fatigue is applied in corrosive environment. The few experimental results are approached assuming that corrosion is accelerating fatigue damage in a manner similar to that for notched fatigue configurations. For this reason, specific concentration factors, that take into consideration the life reduction of prior corroded samples and combined corrosion-fatigue ones, have been derived. No crack propagation is evaluated within the paper. Simple specimens geometry are considered for tests with low and high shape concentration factor (K_t) representative of typical aircraft application. The samples are initially corroded and then subjected to fatigue load in two conditions: (1) simple fatigue applied in air on prior corroded samples and (2) fatigue in corrosive environment. The stress level assumed in the identification of fatigue damage is determined on the basis of the net initial section before corrosion. In condition (1), the experiments are related to C-type samples that are rectangular with central hole, while in the condition (2), X-type (dog-bone shape) samples apply. The basic fatigue behavior of aluminum alloy is determined by means of some data available in Ref. [18] with the aid of the related stress equation and modified by the effect of surface characteristics with the application of selected concentration factors.

$$N_{unnotched} / N_{notched} = k_t^4 \qquad (1)$$

The rule of four power function of the K_t is considered for the determination of the life in these new conditions according to Eq. (1). Typical tension-compression machine was used for the test activity. The fatigue load was defined in order to remain in the definite duration part of the S-N plot. A frequency of 1 Hz has been considered during tests in order to avoid frequency effect and emphasizing the corrosion effect. All these samples have been subjected to corrosion before fatigue by an immersion in corrosive solution according to ASTM G-34 and G-36 (corrosive solution: -NaCl (4.0 M); -KNO$_3$ (0.5 M); -HNO$_3$ (0.1 M)). X-type samples have required the presence of corrosive solution during the fatigue loading phase. A specific test equipment has been arranged in order to have a continuous immersion of the test sample in the corrosive solution. Taking into consideration the short duration of the fatigue loading tests, the variation in solution concentration has been assumed as negligible. Samples average geometrical data for C-type (a variation of less than 0.3% was determined) and geometric dimensions for X-type samples are reported in Table 3. In the present preliminary evaluation, an apparent K_t due to corrosion is determined and reported in Table 4. The C-type sample gives a value of 2.17, while the value determined on X-type sample is about 6.03 with a certain difference if compared to previous data [17]. It is possible to observe that the X-type sample reveals more corrosion with respect to the C-type one. For this reason, a typical K-t due to section reduction could be applied in the two cases. The last column in Table 4

Table 3   C-type and X-type geometrical data before fatigue.

Sample	Initial section (mm^2)	Initial thick. (mm)	Corroded thickness (mm)	Residual thickness (mm)	Residual section (mm^2)
C	144.3	6.0	0.4	5.6	134.68
X	120.0	6.0	1.5	4.5	90.0

Table 4   Preliminary K_t identification ($R = 0.1$, 1 Hz).

Sample	S-max[a] (MPa)	N basic	N exp	K_t exp[a]	K_t corr (I)	K_t corr (II)
C2	149.56	1.265e8	7.02e4	6.515	2.17	1.656
X1	147.15	1.694e8	1.0995e5	6.265	6.03	2.08

gives such a second evaluation of the K_t. The value related to C-type is quite consistent to the expected value while the value determined on X-type seems demonstrating a certain effect of the corrosive environment. Other updated details are reported in Ref. [19]. A more deeper investigation is deemed necessary in order to evaluate the effect of corrosive environment with respect to the fatigue on prior corroded sample with the aid of more experimental results. The activity is in progress and new analyses and experiments will be performed on this subject in order to have a better evaluation of the phenomenon.

5. Conclusions

The activity of the Polito department in the field of fatigue is summarized in the paper considering three case studies. The advanced joint design and tests demonstrate the ability of the junction to overcome the weakness of composite laminate if loaded by pin-hole configuration. This satisfactory result gives the possibility to apply advanced joint design to Heliplat scaled prototype for full-scale test. The junction demonstrated a good behavior. The effect of skin-stringer de-bonding in a flat stiffened plate is analyzed in the second case. The static behavior demonstrated a local damage buckling that causes a reduction in global strength of the panel. The local buckling has also caused a snap effect in the strains. This configuration can be seen as a combination of local/global deformation. Fatigue compressive load has been then applied to the damaged site. Some preliminary results demonstrate a certain level of propagation due to the increment of strains after repetitions. The analysis is in progress in order to check for damage growth. The third case is referred to the effect of corrosive environment in typical aerospace light alloy. It has been analyzed by means of specific concentration factors. Original analytical relation has been introduced in a preliminary analysis demonstrating a certain difference with respect to prior corroded configuration. A refined analysis and new

experiments are necessary in order to better understand the situation. The activity is in progress.

Acknowledgments

References

[1] G. Romeo, G. Frulla, HELIPLAT: Aerodynamic and structural analysis of HAVE solar powered platform, in: 1st AIAA Unmanned Aerospace Vehicles, Portsmouth, Virginia, May 20-23, 2002.

[2] G. Romeo, G. Frulla, E. Cestino, G. Corsino, HeliPlat: Design, aerodynamic structural analysis of long-endurance solar-powered stratospheric platform, Journal of Aircraft 41 (2004) 1505-1520.

[3] G. Romeo, G. Frulla, Bearing strength of bolted joints in CFRP wing fittings, in: 23rd International Conference of Aeronautical Sciences (ICAS2002), Toronto, Canada, Sep. 8-13, 2002.

[4] G. Romeo, G. Frulla, Experimental behavior of composite advanced joint under cyclic loads, in: International Committee on Aeronautical Fatigue (ICAF2005) Symposium, Hamburg, Germany, June 8-10, 2005.

[5] G. Frulla, G. Romeo, Numerical/experimental structural characterization of composite advanced joints for HALE-UAV platforms, Composites: Part B 39 (2008) 656-664.

[6] J.D. Withcomb, Predicted and observed effects of stacking sequence and delamination size on instability related delamination growth, J. of Composite Technology & Research 11 (1989) 94-98.

[7] H.A. Whitworth, Evaluation of the residual strength degradation in composite laminates under fatigue loading, Composite Structures 48 (2002) 261-264.

[8] J.W.H. Yap, M.L. Scott, R. Thomson, D. Hachenberg, The analysis of skin-to-stiffener de-bonding in composite aerospace structures, Composite Structures 57 (2002) 425-435.

[9] G. Romeo, G. Frulla, Postbuckling behaviour of graphite/epoxy stiffened panels with initial imperfections subjected to eccentric biaxial compression loading, Intl. J. of Non-linear Mechanics 32 (6) (1997) 1017-1033.

[10] G. Frulla, Buckling and postbuckling behavior of anisotropic rectangular panels under linearly varying combined loads, Intl. J. of Mechanics and Control 6 (1)

(2005) 13-20.

[11] G. Frulla, Structural behavior of damaged anisotropic stiffened panels under compressive loads, in: 25th ICAS Congress, Hamburg, Germany, Sept. 3-8, 2006.

[12] C. Bisagni, V. Giavotto, G. Romeo, G. Frulla, D. Fanteria, A. Lanciotti, Research activities on buckling of composite structures in Italy, In: 50th AIAA/ASME/ASCE/AHS/ASC Structures, Structural Dynamics, and Materials Conference, CA, USA, May 4-7, 2009.

[13] G. Frulla, Static/fatigue structural behaviour of damaged stiffened composite plates for UAS applications, in: SAE 2013 AeroTech Congress & Exhibition, Montreal, Canada, Sept. 24-26, 2013.

[14] G.H. Koch, M.P.H. Brongers, N.G. Thompson, P.Y. Virmani, J.H. Payer, Corrosion Cost and Preventive Strategies in the United States, Technical Report FHWA-RD-01-156, Office of Infrastructure Research and Development Federal Highway Administration, VA, 2001.

[15] Department of Defence Handbook: Aircraft Structural Integrity Program General Guidelines for, MIL-HDBK-1530A, Jan. 2002.

[16] Department of Defence, Materials and Processes for Corrosion Prevention and Control in Aerospace Weapons System, MIL-HDBK-1568B, July 1996.

[17] R. Riili, Numerical/Experimental evaluations of fatigue behaviour of aluminium alloy components in corrosive environment, Final project in Aerospace Engineering, Politecnico di Torino, Italy, 2010.

[18] Department of Defence, Metallic Materials and Elements for Aerospace Vehicle Structures, MIL-HDBK-5H, 1998.

[19] G. Frulla, G. Avalle, V. Sapienza, Preliminary evaluation of the fatigue behaviour of aluminium alloy in corrosive environment, Submitted to: Aircraft Engineering and Aerospace Technology (under publication in press)

Introduction to the Turbulent Flows Theory—An Axially-Symmetric Non-peaceful Flows

Tomasz M. Jankowski

Water Production, Water Supply and Sewerage Enterprise AQUANET SA, Poznan 61-492, Poland

Abstract: In fluid mechanics, there is lack of turbulent flows theory. The theory of laminar flows is also not completed. Therefore, the aim of this paper is to fill in the gaps in the theory of laminar flow. First time in the history of fluid mechanics, it shows that the value of the boundary Reynolds number, dividing the flows of Newtonian fluids into laminar and turbulent, can be calculated theoretically. The very existence of this boundary has been known to researchers over a century ago, but all knowledge in this area so far comes only from experimental physics. This paper marks a turning point, as it not only explains the theory of the said phenomenon, but also presents the methodology of its analytical description. It should be noted that the said description refers to the type of flow which is best understood by scientists, i.e., steady axially-symmetric laminar flow through a straight-axis duct of a circular cross-section of the radius R under the action of constant natural gravitational forces. This paper comes second in a series of papers aimed at eliminating chaos from fluid mechanics and replacing it with harmony and mathematical order.

Key words: Dualism theory, primary motion, secondary motion.

Nomenclature

a—Dynamic field intensity, directional acceleration (m/s^2)

d—Differential symbol

f—Function denotation

g—Gravitational, steric acceleration ≈ 9.81 m/s^2

h—Distance on transverse direction to the fluid flow direction, where, $0 \leq h \leq H$ (m)

m—Mass of the fluid in motion (kg)

t—Time (s)

z—Sense intensity of the gravitational field ≈ 2.45 m/s^2

B—Division coefficient

C—Cycloidal motion participation

F—Cross section area (m^2)

G—Graviton

H—Height (thickness) of the analyzed layer of fluid, measured on transverse direction to the flow direction, where $H \geq 0$ (m)

J—Resistance to motion

L—Laminar motion participation

N—Perpendicular (normal) to the fluid flow direction

P—Force (N, kg)

R—Duct radius

$R1$—Core radius

Re—Reynolds number

U, $U1$—Fluid structure state coefficients

V—Fluid velocity (m/s), fluid capacity (m^3)

X—Parallel direction to the fluid flow direction

α—Density coefficient

λ—Linear resistance coefficient (lambda)

ν—Fluid kinematic viscosity (ny) (m^2/s)

ρ—Fluid mass density (ro) (kg/m^3)

Subscripts

gr—Terminal, boundary

max—Maximal

pr—Threshold

sr—Average

x—On parallel direction to the fluid flow direction

A—Core phase subspace

B—Annular boundary layer phase subspace

C—Semicycloidal, active, centripetal

G—Free (natural, primary) gravitation

$G1$—Freed (secondary) gravitation

K—Cumulated, opposition, centrifugal

L—Semilaminar

N—Perpendicular (normal) to the duct axis

R—Primary motion

$R1$—Secondary motion

Corresponding author: Tomasz M. Jankowski, M.Sc. Eng, senior technologist, head of problem task titled "turbulent flows theory". E-mail: tomasz.jankowski@aquanet.pl.

1. Introduction

The fundamental flows division of Newtonian (viscous) liquids on laminar and turbulent has been known in fluid mechanics since long. Those flows are separated by the so-called boundary Reynolds number Re_{gr}. The said division was discovered empirically approximately in 1883 by Osborne Reynolds (1842-1912), a British physicist and engineer, author of brilliant works on hydraulics and lubrication. He monitored in his experiments the behavior of a marker (colorant) in water flowing in a tube. When $Re \leq Re_{gr}$, the colored streak moved alongside the tube's axis and continued to be coherent and well visible. As soon as $Re > Re_{gr}$, the streak dissolved and disintegrated quickly, as a result of mixing with the surrounding mass of fluid. Thus far, Reynold's discovery did not have a theoretical interpretation which means that underlying cause and the mechanism of the said phenomenon is still not understood [1].

To change this state of affairs, the enlargement of recently discovered basis of dualism theory of Newtonian fluids motion [2] will be presented below. This enlargement introduces, inter alia, the principle of constancy and uniformity of internal opposition forces field to fluid state physics (fluid mechanics). It establishes that the intensity of opposition forces field is always stable and equal to the intensity of gravitational forces field. The said principle provides a basis for the theoretical formulation of a general description of the mechanism of creation of the boundary between laminar and turbulent flows, as presented in this paper. The said mechanism is presented below using the example of a steady, axially-symmetric laminar flow of Newtonian fluid through a straight-axis duct of a circular cross-section and the radius R, under the action of natural gravitational forces.

In following deliberations, particular importance is attributed to the effect of the natural terrestrial gravitational field on fluid. It is shown that this effect determines the division of fluid flows into peaceful and non-peaceful, and further into laminar and turbulent. A new physical interpretation of the notion of "graviton" is introduced, and the action of internal forces in fluid in motion is described. To visualize and mathematically describe internal friction forces, the classical model of laminar flows proposed by Poiseuille (Jean Louis Marie Poiseuille, 1797-1869) is used. The key point of the paper is a precise, theoretical calculation of the boundary Reynolds number, resultantly determined as 2,268.

This paper is the second one in a series of papers describing the possibilities of the theory of dualism in fluid mechanics. The deliberations presented here are a continuation of those contained in Ref. [1]. The dependencies assumed therein are accepted as true here. Therefore, the author wishes to remark that in order to fully understand the content of Ref. [2], it is necessary to have read Ref. [1].

The paper is divided into the following parts: Sections 2 and 3 contain a review of and additional information to issues presented in paper No. 1 [2]; Sections 4 and 5 present a systematic discussion of notions used to describe internal motion; Sections 6 and 7 describe the phenomenon of primary cycloidal motion in a field of active forces; Sections 8-11 deal with a completely new phenomenon of structural instability of the primary field of active forces; Section 12 describes the primary laminar motion in a field of opposing forces; Section 13 explains the notion of secondary gravitational field; Section 14 presents secondary motion; Section 15 summarizes non-peaceful flows and their characteristic values; Section 16 contains conclusions; Section 17 presents issues to be discussed in further papers in the series.

2. Peaceful Flows—Selected Issues Presented in Ref. [1]

(1) T. Kowalewski, et al. [1] introduced to fluid state physics (fluid mechanics) a new interpretation of physical phenomena taking place in fluid in motion. It introduced the basis for the new dualism theory which

says that each flow has its own internal motion structure, which means clearly defined organization of phase space of fluid in motion, not "molecular chaos", known from static conditions. The paper also introduced the concept of organization of vector fields of velocities (momentums) and accelerations (internal forces). It showed that each Newtonian fluid flow is the result of transforming work induced by external forces into work induced by internal forces. Internal forces in peaceful flows have been divided into active forces (C) and opposition forces (L), which are equal to one another.

(2) The dualism theory introduces to fluid mechanics improvements of Poiseuille's classical model of laminar flows (L). It also introduces a new model of cycloidal motion (C). The dualism theory shows that the model, dual description of physical phenomena in fluid in motion makes it possible to develop a full, theoretical description of the orientation of motion structures and forces that create motion and induce fluid flow.

This theory has been described by an example of a steady, axially-symmetric peaceful flow of homogeneous Newtonian fluid through a straight-axis duct of a circular cross-section under the action of constant natural gravitational forces.

The basic dependencies of the dynamic vector field resulting from the model are as follows:

$$V_{\max} = 2\omega \frac{H}{2} = 2V_{\acute{s}r} = \frac{gJH^2}{4v} \qquad (1)$$

$$\omega = \frac{V_{\max}}{H} = \frac{2V_{\acute{s}r}}{H} = \frac{gJH}{4v} \qquad (2)$$

$$a_{\max} = \omega^2 \frac{H}{2} = \frac{V_{\max}^2}{2H} = \frac{2V_{\acute{s}r}^2}{H} = \frac{g^2 J^2 H^3}{32v^2} \qquad (3)$$

(3) The previous paper described the effect of constant external natural gravitational forces on the formation of the internal flow structure. The said effect induces in the fluid its own, internal gravitational field of constant intensity $z = 0.25$ g ≈ 2.45 m/s^2. It forms

"molecular chaos" in the fluid, observed experimentally under static conditions.

(4) In dynamic conditions of peaceful flow that "chaos" is gradually oriented by opposition forces, defined by the characteristic vector $a_{\max.L}$. However, in the case of peaceful flows, such opposition forces are always equal to active forces, and thus $a_{\max.L} = a_{\max.C}$.

(5) The degree of "chaos" orientation is measured by the coefficient "U" whose growth is proportional to the growth of flow dynamics. At the threshold flow ($Re_{pr} = 1,962$), the orientation is completed ($U = 1$).

3. Peaceful Flows—Additional Information to Ref. [1]

Prior to describing non-peaceful flows it is necessary to introduce to the previous paper a number of additional information and new definitions of selected notions.

3.1 Fluid Phase Space

The uniform mass of fluid described in the paper constitutes a "space" filled with an unlimited number of dimensions, each of which corresponds to one coordinate of position, velocity, acceleration and time. The said space is referred to as the fluid phase space. For n molecules, the said space has 10 n dimensions, i.e.:

• three position coordinates (two coordinates in two-dimensional space);

• three velocity components (two components in two-dimensional space);

• three acceleration components (two components in two-dimensional space);

• one time component.

Thanks to mathematical equations introduced in the previous paper, the description of movement of any point in the phase space is equivalent to the description of evolution of the entire structure of the system pervading that space. The phase space is not empty. In the discussed case, it is filled by fluid containing unitary carriers of gravitational field forces, known as gravitons.

3.2 Reminder Classical Definition of Graviton

Graviton—a hypothetical elementary particle, a quantum of energy, which has no rest mass or electric charge, but is able to transmit the gravitational interaction.

3.3 New Definition of Graviton

Graviton—a quantum of energy, unitary force of gravitational field dG, induced in the phase space of the fluid affected by the said field, measured with the product of molecular mass of the fluid dm and twice the value of the gravitational field intensity z, in accordance with the following:

$$dG = 2z\rho\, dV = \frac{g}{2}\rho dV = \frac{g}{2} dm \qquad (4)$$

Gravitons are oriented spatially and directionally. Under terrestrial conditions, a spatially oriented graviton has a constant value equal to 2 g dm ≈ 19.62 [m/s^2] dm. A directionally oriented graviton has a value of $z = 0.5\, g$ dm. A graviton consists of a centripetally oriented prograviton (dG_C) and a centrifugally oriented antigraviton (dG_L), for which the following equation is true:

$$dG_C = dG_L = \frac{dG}{2} = z\rho\, dV = \frac{g}{4} dm \qquad (5)$$

The directional action of a graviton is always perpendicular to the monolayer of the phase boundary in multiphase systems.

3.4 Vector Field of Motion

The vector field of motion in the fluid phase space means the sum of overlapping internal fields of momentums and dynamic forces generated by the flow. The description of the force field requires strict adherence to Newtonian laws (Isaac Newton 1642-1727), whereby the position of each particle is analyzed together with the pace of its position changes. In the description of the field of momentums (momentum of a particle is equal to the product of its mass and velocity), the position of each particle is analyzed together with its velocity, just like in

Hamilton's equations (William Rowan Hamilton 1805-1865) [3].

3.5 Internal Molecular Forces and Their Transmission Lines

An internal molecular force means the unitary force dP applied to an individual fluid molecule of nearly zero mass dm, with acceleration a_{max}. In peaceful flows (described in the previous paper) the internal molecular forces were divided into:

• Active molecular forces (oriented centripetally), where d$P_C = a_{max.C}$ d$m = \rho\, a_{max.C}$ dV;

• Opposition molecular forces (oriented centrifugally), where d$P_L = a_{max.L}$ d$m = \rho\, a_{max.L}$ dV.

The flow of fluid builds within that fluid a motion structure, or orientated transmission of internal molecular forces. Chaotic oscillation of molecules induced by gravitons under static conditions is thus replaced by systematized, orientated oscillation with clear shape of force transmission lines (paths). Such lines form a graphical representation of motion structures. In peaceful flows they were divided into:

• centripetal active force transmission lines (C)—taking the form of a dynamic semi-cycloid—forming the image of semi-cycloidal motion structure;

• centrifugal opposition force transmission lines (L)—exactly transverse to fluid momentum direction lines—forming the image of transverse motion structure;

• infinite set of clearly shaped semi-cycloidal transmission lines of active forces and infinite number of corresponding transverse transmission lines of opposition forces forms a graphic representation of the motion force field structures and thus motion acceleration field structures.

3.6 Structure of Momentums Field of Progressive Motion

In accordance with the dualism theory [2], the structure of active force field (C) is a derivative of the structure of the momentum field with respect to time. Particularly important is the structure of momentums

field of progressive motion. The said structure is directional and matches the flow direction and directional lines of the momentum of each molecule of fluid in motion. The distribution of momentums in the longitudinal section of this motion takes a characteristic parabolic shape that can be measured experimentally.

In the classical laminar motion theory based on Poiseuille's classical model of laminar flows, the structure of the progressive motion has a parabolic shape as well. It follows from the above that both structures are identical, despite being built on different models.

3.7 Principle of Constancy and Uniformity of Opposition Forces Internal Field

If one assumes that internal opposition forces field is created by free gravitons and by gravitons linked to the motion structure, it is easy to realize that the principle of constancy and uniformity of the internal field of opposition forces applies to peaceful flows. In the entire mass of fluid in motion the intensity of that field is exactly the same, and its value is $z = 0.25\ g \approx 2.45$ m/s^2, in accordance with the following dependency:

$$a_{\max.LG} = a_{\max.L} + a_{\max.GL} = z = \frac{g}{4} \qquad (6)$$

It should be emphasized that the value of opposition forces, defined by means of the characteristic vector $a_{\max.L}$, is variable, while the value of intensity of the opposition force field formed by opposition forces (with centrifugally oriented vector $a_{\max.L}$) and antigravity forces (with centrifugally oriented vector $a_{\max.GL}$), is constant and remains unaffected by flow dynamics. This means that in peaceful flows the growth in opposition forces (L) is at the expense of the depletion of free gravitons (GL).

The principle of constancy and uniformity of the intensity of the opposition forces' internal field will be applicable (in a slightly changed form) also to non-peaceful flows, which means that it will be applicable across the entire range of laminar flows.

3.8 Work and Internal Friction

Progressive motion of fluid is induced by the excess of "ascending" work over "descending" work. The underlying fact is that the "ascending" path along the dynamic cycloid arch ($a_{\max.C}$) is longer than the "descending" path perpendicular to the duct axis and flow direction ($a_{\max.L}$, where, $a_{\max.L} = a_{\max.C}$).

The work induced by active forces (C) is converted by opposition forces (L) to internal friction, defined by means of the classical Darcy-Weisbach equation (Henry Philibert Gaspard Darcy 1803-1858, Julius Ludwig Weisbach 1806-1871):

$$J = \lambda \frac{1}{2R} \frac{\alpha V_{sr}^2}{2g} \qquad (7)$$

3.9 No Fluid Friction against the Duct Wall

Until now, fluid friction against the wall was understood as the force tangent to the wall, counteracting the movement of fluid relative to the wall. On the basis of solid state physics one could expect this to be slide friction that depends on wall roughness and the pressure force perpendicular to the direction of the friction force. Simultaneously, it has been shown empirically that in laminar flows (both peaceful and non-peaceful), friction forces are independent from wall roughness and are always equal to zero, as if duct walls were always "perfectly smooth". Therefore, a paradoxical conclusion can be drawn that the only reason for the lack of fluid friction against the wall is the lack of a perpendicular pressure force acting on the wall.

The dualism theory describes and explains the above phenomenon in an alternative way. Active molecular forces (C) generated in fluid in motion are equal to opposition molecular forces (L). At the directional lines of those forces (transverse to fluid momentum direction lines), near the duct wall and axis, those forces are equal to one another, but their senses are opposite. Therefore, the forces are zeroed out, as shown in Fig. 1.
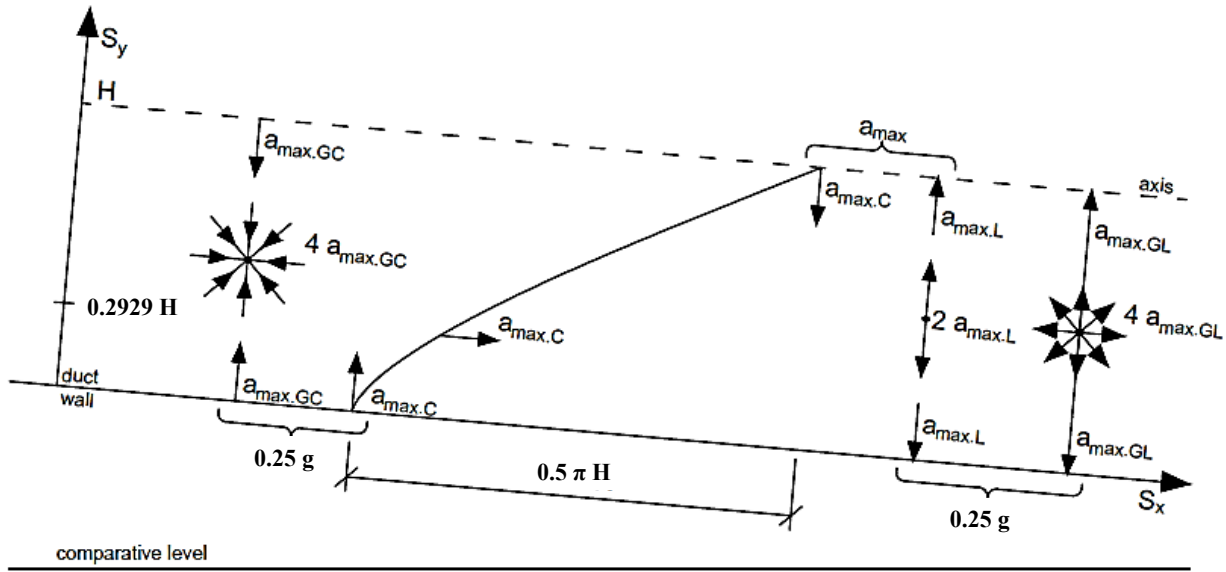
Fig. 1   Structure of accelerations field (internal forces) of axially-symmetric peaceful flow.

3.10 Density Coefficient

An analysis of non-peaceful flow must be preceded by mentioning and redefining the coefficient α. This value, thus far known as Coriolis coefficient (Gaspard Coriolis 1792-1843) or Saint-Venant coefficient (Adhemar Saint-Venant 1797-1886), was defined as the ratio of the actual kinetic energy of stream filaments to apparent energy, calculated for average velocity, as the following formula shows [4]:

$$\alpha = \frac{\int_F V^3 dF}{V_{śr}^3 F} \tag{8}$$

The above formula is in fact empirical. Therefore, for the purpose of further discussion a purely theoretical definition has been assumed, whereby the coefficient α is redefined as the density coefficient of the dynamic vector field.

The said coefficient is the ratio of the field's extended surface F of the thickness H and intensity a_{max} (a rectangle of the sides $2\pi R$, H) to its compacted surface (a ring of the external circumference $2\pi R$ and thickness H). In a uniform force field, the coefficient is expressed (after conversion) as the ratio of the vector field surface to its hydraulic radius, as the following formula shows:

$$\alpha = \frac{F \, a_{max}}{F_R \, a_{max}} = \frac{H}{R_h} \tag{9}$$

For instance, for already discussed peaceful flow through a duct of the radius R the value of the hydraulic radius R_h is:

$$R_h = \frac{\pi R^2}{2\pi R} = \frac{R}{2} \tag{10}$$

For peaceful flow the density coefficient α is:

$$\alpha = \frac{R}{R/2} = 2 \tag{11}$$

4. Components of Non-peaceful Flows

The notion of non-peaceful flows was partially defined in Ref. [2]. In general, non-peaceful flows are classified as laminar flows ($0 < Re \leq Re_{gr}$), but due to their specific nature, they constitute a separate group of such flows, that stays within the following range: $Re_{pr} < Re \leq Re_{gr}$. In the analyzed case (steady, axially-symmetric laminar flow of Newtonian fluid through a straight-axis duct of a circular cross-section and radius R, under the action of natural gravitational forces), the value of the threshold Reynolds number is $Re_{pr} = 1,962$. The boundary Reynolds number Re_{gr} is different. It defines the laminar flow boundary.

Searching of theoretical Re_{gr} value is the subject of the analysis in this paper.

The dualism theory shows that the structure of motion, created for the purposes of peaceful flows, becomes ineffective in the case of non-peaceful flows. This structure must be redeveloped for flows $Re >$ 1,962, because there are no sources of new, free gravitons in the fluid to build opposition forces ($a_{max.GL}$ = 0). This means that these forces are not capable of further growth. Further increase in the value of vector $a_{max.L}$, coupled with the growth of flow dynamics, becomes impossible. Changes are thus necessary.

And such changes take place. In non-peaceful flows the vector of opposition forces field intensity $a_{max.L}$ is conventionally transformed into the vector of primary laminar motion forces field intensity $a_{max.RL}$. The said vector is not capable of further growth, despite growing flow dynamics. To the contrary, its value decreases, because the part of gravitons, previously embedded in the motion structure, are spontaneously freed. However, these gravitons do not come from the natural, terrestrial gravitational field. They are freed and require primary forces of creation motion to sustain their existence. They create a new field of forces $a_{max.G1L}$, whose intensity is defined by a characteristic product $z(1$-$U1)$, which now becomes a passive component of primary field of opposition forces.

The field of opposition forces pervades the entire phase space of fluid in motion (in the analyzed case the said field pervades the entire mass of fluid in a duct of the radius R). In accordance with the above-assumed principle of constancy and uniformity of the intensity of the opposition forces' internal field, the intensity of the primary field of opposition forces (sum of laminar motion forces and freed antigravity forces) is constant and equal to:

$$a_{max.LG1} = a_{max.RL} + a_{max.G1L} = a_{max.pr} = z_1 \quad (12)$$

where,

$$a_{max.G1L} = z_1(1\text{-}U1) = \frac{g}{4} - a_{max.RL} \quad (13)$$

Also in this case, like in peaceful flows, the value of

opposition forces ($a_{max.RL}$) is variable, while the value of intensity of the opposition force field ($a_{max.RL} + a_{max.G1L}$) is constant and remains unaffected by flow dynamics. At the same time, active forces do not face such limitations. They increase quickly.

The vector of active force field intensity $a_{max.C}$, known from peaceful flows, is conventionally converted to the intensity vector of active forces primary field $a_{max.RC}$ in non-peaceful flows. The said vector is a sum of intensities of the primary force field in semi-cycloidal motion $a_{max.RCC}$ and in primary semi-laminar motion $a_{max.RCL}$.

Primary active forces field also pervades the entire mass of fluid, but it is divided into two overlapping components, A and B (two partial field forces). The intensity of both fields is diverse. As a result of such division, the coaxial flow core with the radius $R1$ is created (field A). Inside that core these forces additionally generate secondary motion.

The flow core is surrounded by concentric, annular boundary layer (field B). It takes the form of a coaxial ring. The core wall, separating core from boundary layer, creates a fluid-to-fluid monophase boundary, invisible to the naked eye. It has its own specific properties, such as: lack of roughness, flexibility and specific tightness, which allow for clear separation of forces generated within the core from those within the boundary layer.

The formation of the flow core structure and its surrounding ring-shaped boundary layer is not a one-off phenomenon. It is rather a cyclical, consecutive and time-determined process, whose individual cycle phases form a sequence. The structures of force fields in each phase differ from one another. In this paper four structures, considered to be the most characteristic, are described. They are marked with consecutive Roman numerals: I, II, III and IV. The time delay between each cycle phase causes periodical fluctuation of all physical values of the flow. In Reynold's experiment, the colored streak in the tube containing flowing fluid fluctuates restlessly, although it is still

coherent and well visible. However, it gives an impression that the flow is instability, which is why flows exhibiting this kind of fluctuation are referred to as non-peaceful.

4.1 Peaceful and Non-peaceful Flows

Laminar flows were divided into:

• peaceful flows $(0 < Re \leq Re_{pr})$—discussed in paper No. 1;

• non-peaceful flows $(Re_{pr} < Re \leq Re_{gr})$—discussed below.

4.2 Flows and Internal Motion

External forces acting on fluid make it flow, and the resulting directional motion within fluid first creates structures of the field of momentums, and then structures of the field of internal molecular forces (motion force field is a derivative of its field of momentums with respect to time).

Internal motion is understood as oscillation motion of each molecule. Once orientated, molecules form the field of momentums, and then the force field. It needs to be emphasized that this notion serves the purpose of describing orientated transfer of forces along the lines of orientated oscillation of molecules. It is not a description of the displacement of individual fluid molecules within its mass.

4.3 Primary Motion and Secondary Motion

Systematized internal motion induced by fluid flow is divided into:

• Primary motion (R), forming its axisymmetric structure in a duct, with characteristic flow core;

• Secondary motion $(R1)$, formed in the flow core on the basis of the primary motion, and then dispersed throughout the entire phase space of fluid—this kind of flow is always absent from peaceful flows.

Internal friction is a reaction to this motion. Given that secondary motion is fully created on the basis of the primary motion, the friction caused by it is fully contained in the friction caused by the primary motion.

5. Primary Motion and Its Forces in the Phase Space of Fluid in Motion

To further describe physical phenomena occurring in fluid in motion it is necessary to adopt a new set of relevant notions.

5.1 Modification of Notions Describing Internal Forces in Peaceful Flows

In peaceful flows, described in detail in paper No. 1, internal molecular forces were divided into:

• Active molecular forces $(dP_C, a_{max.C})$, oriented centripetally, transmitted along a dynamic cycloid arch;

• Opposition molecular forces $(dP_L, a_{max.L})$, oriented centrifugally, transmitted perpendicularly to the directional lines of momentum;

• Active forces are equal to opposition forces $(dP_C = dP_L, a_{max.C} = a_{max.L})$;

• The intensity of the field of opposition forces is constant $(a_{max.L} + a_{max.GL} = 0.25\ g)$.

In peaceful flows, the same internal molecular forces can be alternatively divided into:

• Active molecular forces $(dP_{RC}, a_{max.RC})$, constituting a sum of centripetally oriented forces of semi-cycloidal motion $(dP_{RCC}, a_{max.RCC})$, transmitted on the "ascending" path along the dynamic cycloid arch and semi-laminar motion forces $(dP_{RCL}, a_{max.RCL})$ transmitted on the "descending" path perpendicular to the directional lines of momentum;

• Opposition molecular forces $(dP_{RL}, a_{max.RL})$, constituting a sum of centripetally oriented forces of semi-cycloidal motion $(dP_{RLC}, a_{max.RLC})$, transmitted on the "ascending" path along the dynamic cycloid arch and semi-laminar motion forces $(dP_{RLL}, a_{max.RLL})$ transmitted on the "descending" path perpendicular to the directional lines of momentum;

• Semi-cycloidal motion forces are equal to semi-laminar motion forces $(dP_{RCC} = dP_{RCL}, a_{max.RCC} = a_{max.RCL}; dP_{RLC} = dP_{RLL}, a_{max.RLC} = a_{max.RLL})$;

• Active forces and opposition forces are equal $(dP_{RC} = dP_{RL}, a_{max.RC} = a_{max.RL})$;

- The field intensity of opposition forces is constant $(a_{max.RL} + a_{max.GL} = 0.25\ g)$.

In non-peaceful flow, the other (alternative) division will be used, with indexes marked with the letter R (primary motion). At a later stage of the deliberations, the index $R1$ will be introduced to denote secondary motion values.

5.2 Notions Describing Primary Internal Forces in Non-peaceful Flows

In non-peaceful flows, primary internal forces are divided into:

- Molecular active forces of cycloidal motion (dP_{RC}, $a_{max.RC}$), further divided into forces of semi-cycloidal motion (dP_{RCC}, $a_{max.RCC}$) and forces of semi-laminar motion (dP_{RCL}, $a_{max.RCL}$);

- Opposition molecular forces of laminar motion (dP_{RL}, $a_{max.RL}$) to facilitate further notations they are not subdivided into forces of semi-cycloidal motion and forces of semi-laminar motion, even though such subdivision actually exists;

- Semi-cycloidal motion forces are equal to semi-laminar motion forces ($dP_{RCC} = dP_{RCL}$, $a_{max.RCC} = a_{max.RCL}$; $dP_{RLL} = dP_{RLL}$, $a_{max.RLL} = a_{max.RLL}$);

- Active forces are greater than opposition forces ($dP_{RC} \geq dP_{RL}$, $a_{max.RC} \geq a_{max.RL}$);

- The intensity of the primary field of opposition forces is constant ($a_{max.RL} + a_{max.G1L} = 0.25\ g$).

Freed antigravitons ($a_{max.G1L}$) are one of the components of the intensity of the primary field of opposition forces. The amount of antigravitons grows in line with the growth of flow dynamics which means that the value of opposition forces ($a_{max.RL}$) is proportionally reduced at the same time. This also means that freed gravitons are quanta of energy freed from internal motion structures and form "secondary molecular chaos" within fluid.

In accordance with the dualism theory, the action of internal forces in Newtonian (viscous) fluid induces internal friction forces, divided into:

- friction induced by active forces;

- friction induced by opposition forces.

5.3 Primary Cycloidal Motion and Primary Laminar Motion

The entirety of the steady primary non-peaceful flow consists of: primary cycloidal motion denoted as C_R and the primary laminar motion denoted as L_R. It has been assumed that the average value of primary flow is the sum of its components, in accordance with formula:

$$V_{sr.R} = V_{sr.RC} + V_{sr.RL} = C_R V_{sr.R} + L_R V_{sr.R} = \\ = (C_R + L_R)\ V_{sr.R} \quad (14)$$

where,

C_R—share of the primary cycloidal motion in the entirety of primary motion;

L_R—share of the primary laminar motion in the entirety of primary motion.

$$C_R + L_R = 1 \qquad C_R \geq L_R \qquad (15)$$

The notion of laminar motion differs from the motion of laminar flow. It has been assumed that flow is caused by the action of external forces. In its turn, motion is a response to flow and is induced by the action of internal forces.

5.4 Primary Progressive Motion and Primary Transverse Motion

The resultant of the action of orientated oscillation forces induces the flow of fluid and orientates internal motion, which is divided into:

- progressive motion—forming a directional structure aligned with the flow direction and directional lines of momentum of individual molecules of fluid in motion—the distribution of momentums in this motion can be measured experimentally;

- transverse motion—forming a directional structure perpendicular to the flow direction due to motion symmetry in axially-symmetric laminar flows, transverse motion cannot be measured experimentally—pure transverse motion occurs only at the duct wall.

The response to motion takes the form of internal friction, which is divided into:

- friction induced by progressive motion;
- friction induced by transverse motion.

5.5 Force Transmission Lines in Primary Motion

The structure of the primary force field and accordingly the field of motion accelerations in the phase space of fluid is formed by an infinite set of force transmission lines that form a graphical representation of those structures. In non-peaceful flows the said lines are divided into:

- transmission lines of cycloidal motion (RC) forces—transmission lines of active forces;
- transmission lines of semi-cycloidal motion (RCC) forces—taking the shape of dynamic semi-cycloidal arch;

- transmission lines of semi-laminar motion (RCL) forces—transverse to directional lines of fluid momentum;
- transmission lines of laminar motion (RL) forces—transmission lines of opposition forces.

5.6 Common Designations of Forces and Internal Motion in Non-peaceful Flows

The diversity of types of unitary forces forming internal motion and the resultant flow of fluid in the duct, as well as the diversity of internal forces' transmission lines forming motion structure in non-peaceful flows requires the introduction of common set of notions describing internal motion and internal forces. Such notions will be based on designations of unitary accelerations in each of the force fields, superimposed on motion fields (Table 1).

Table 1   New set of notions of internal vector field.

Internal motion	Internal motion caused by internal active forces (C)		Internal motion caused by internal: opposition forces (L) spatial motion (G1)
	Semi-cycloidal motion (C)	Semi-laminar motion (L)	
Core-annular primary motion (R)	$a_{\max.RCC}$ $a_{\max.RAC}$	$a_{\max.RCL}$ $a_{\max.RAL}$	$a_{\max.RL}$
	$a_{\max.(R1)}$ $a_{\max.RANC}$	$a_{\max.RANL}$	
	$a_{\max.RBC}$ $a_{\max.RBNC}$ $a_{\max.R(R1)}$	$a_{\max.RBL}$ $a_{\max.RBNL}$	
Examples of mathematical relations	$a_{\max.RA} = a_{\max.RAC} + a_{\max.RAL}$ $a_{\max.RB} = a_{\max.RBC} + a_{\max.RBL}$ $a_{\max.RA} = a_{\max.RAN} + a_{\max.(R1)}$ $a_{\max.RB} = a_{\max.RBN} + a_{\max.R(R1)}$ $a_{\max.RA} = H_{RB}/H_{RA}\, a_{\max.RB}$ $a_{\max.G1} = 2(a_{\max.RB} - a_{\max.RA})$ $a_{\max.RAN} = H_{RB}/H_{RA}\, a_{\max.RBN}$ $a_{\max.(R1)} = H_{RB}/H_{RA}\, a_{\max.R(R1)}$ $a_{\max.RB} - a_{\max.RA} + a_{\max.RL} = 0.25\ g$ $a_{\max.RL} + a_{\max.G1L} = 0.25\ g$	look at: (40) (42) (52) (53) (62) (62)	
Core-annular secondary motion (R1)	$a_{\max.(K1)C}$ $a_{\max.KK1C}$ $a_{\max.RK1C}$		$a_{\max.KK1}$ $a_{\max.G1}$ $a_{\max.(K1)L}$ $a_{\max.KK1L}$ $a_{\max.RK1L}$
Examples of mathematical relations	$a_{\max.KK1} = R/R1\, a_{\max.(R1)}$ $a_{\max.KK1} = a_{\max.K1} + a_{\max.(K1)}$ $a_{\max.K1} = a_{\max.K1C} + a_{\max.K1L}$ $a_{\max.K1} = H_{RA}/2R1\, a_{\max.(R1)}$ $a_{\max.(K1)} = H_{RB}/2R1\, a_{\max.(R1)}$ $a_{\max.KK1} = 2R/H_{RA}\, a_{\max.K1}$ $a_{\max.RK1} + a_{\max.(K1)} + a_{\max.RL} = 0.25\ g$	look at: (51) (71) (72) (73) (73) (74)	

6. Primary Cycloidal Motion in Active Force Field—Velocity Field Structure

Primary cycloidal motion (C_R) in the field of active forces in non-peaceful flow is a continuation of cycloidal motion of peaceful flows. The said motion (RC) pervades the entire phase space of fluid in a duct of the radius R. The said space is divided into two components: concentric partial space RA (core space) and concentric partial space RB (ring space). Each of the partial spaces is pervaded by the primary vector field of velocities and accelerations.

6.1 Velocity Field Structure of Primary Semicycloidal Motion [5]

The structure of velocity field of primary semicycloidal motion derived from the semicycloidal motion of peaceful flows. Under new conditions, this structure becomes more complicated, but the rule of its construction remains unchanged. The said rule states that the growth of the velocity vector (local velocity component) in phase space of primary semicycloidal motion is directly proportional to the growth of fluid mass in that velocity's field, such mass being calculated as from the duct wall in accordance with the following formula:

$$V_{x.RCC} = V_{max.RCC} \frac{R^2 - (R - h_{RCC}) \cdot |R - h_{RCC}|}{R^2 - (R - H_{RCC}) \cdot |R - H_{RCC}|} \quad (16)$$

The maximum velocity value in both subspaces of primary semicycloidal motion is in accordance with the following formula:

$$V_{max.RCC} = \frac{g J_{RCC} H_{RC}^2}{4 v \, \alpha_{RCC}} \cdot \frac{R^2 - (R - H_{RC}) \cdot |R - H_{RC}|}{R^2} \quad (17)$$

Vector dependencies in primary semicycloidal motion velocity field are based on the basic output dependency:

$$V_{max.RAC} = V_{max.RBC} = \frac{1}{2} C_R V_{sr.R} \quad (18)$$

The thickness of the RA subspace layer is greater (equal for $Re = 1,962$) than R ($H_{RA} \geq R$), and the thickness of the RB subspace is smaller (equal for $Re = 1,962$) than R ($H_{RB} \leq R$), and thus the resultant dependencies:

$$V_{max.RAC} = \frac{g \, J_{RAC} \, H_{RA}^2}{4 v \, R^2} \cdot \left(2R^2 - 2RH_{RA} + H_{RA}^2\right) \quad (19)$$

$$V_{max.RBC} = \frac{g \, J_{RBC} \, H_{RB}^2}{4 v \, R^2} \cdot H_{RA} H_{RB} \quad (20)$$

The average velocity in phase space of primary semicycloidal motion:

$$Q_{RC} = Q_{RCC} + Q_{RCL} = \pi R^2 \, V_{sr.RC} \quad (21)$$

$$Q_{RCC} = Q_{RAC} + Q_{RBC} = \pi R^2 \, V_{sr.RC} \quad (22)$$

$$Q_{RCC} = \iint_{F_{RA}} V_{x.RAC} \, dF_{RA} + \iint_{F_{RB}} V_{x.RBC} \, dF_{RB} = \int_0^{2\pi} \int_0^R \frac{R^2 V_{max.RXC}}{R^2 + (R - H_{RA})^2} \left[1 - \left(\frac{R - h_{RA}}{R}\right)^2\right] (R - h_{RA}) \, d(R - h_{RA}) \, d\varphi +$$

$$+ \int_0^{2\pi} \int_0^{(H_{RA} - R)} \frac{R^2 V_{max.RXC}}{R^2 + (R - H_{RA})^2} \left[1 + \left(\frac{R - h_{RA}}{R}\right)^2\right] (R - h_{RA}) \, d(R - h_{RA}) \, d\varphi +$$

$$+ \int_0^{2\pi} \int_{(R - H_{RB})}^R \frac{R^2 V_{max.RXC}}{R^2 - (R - H_{RB})^2} \left[1 - \left(\frac{R - h_{RB}}{R}\right)^2\right] (R - h_{RB}) \, d(R - h_{RB}) \, d\varphi = \pi R^2 V_{sr.RCC} \quad (23)$$

6.2 Velocity Field Structure of Primary Semi-laminar Motion

The structure of the velocity field of primary semi-laminar motion duplicates the structure of the velocity field of primary semi-cycloidal motion.

Since the velocity fields match each other, all relationships deduced above will be applicable to the mathematical description of the primary semi-laminar flow.

6.3 Velocity Field Structure of Primary Cycloidal Motion (Primary Field of Active Forces)

The structure of the velocity field of primary cycloidal motion is the sum of velocity fields' structures of the primary semi-cycloidal motion and the primary semi-laminar motion. The structure of this field in an axial section is shown graphically in Fig. 2. The mean velocity of cycloidal motion $V_{sr.RC}$ is determined by the following dependency:
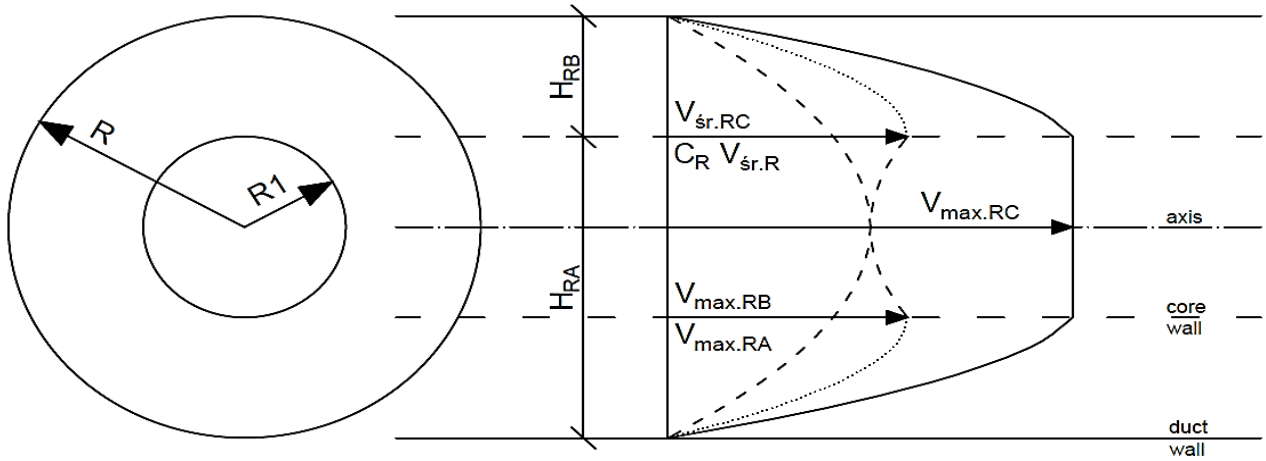
Fig. 2   Axial section of velocity field structure of primary cycloidal motion.

$$V_{sr.RC} = 2V_{sr.RCC} = 2V_{max.RAC} = 2V_{max.RBC} = \tag{24}$$
$$= V_{max.RA} = V_{max.RB}$$

The maximum velocity of cycloidal motion $V_{max.RC}$ is determined by the following dependency:

$$V_{max.RC} = V_{sr.RC} \; \frac{2R^2}{R^2 + (R - H_{RA})^2} = \tag{25}$$
$$= V_{sr.RC} \; \frac{2R^2}{2R^2 - 2RH_{RA} + H_{RA}^2}$$

6.4 Characteristic Values of Primary Cycloidal Motion

An analysis of structure of primary cycloidal motion velocity field allows one to identify in classical way (Poiseuille model) an internal friction forces which are induced by active forces. In RA subspace the characteristic vectors of the field are:

$$V_{max.RAC} = \frac{1}{2}V_{sr.RC} = \omega_{RA}\frac{H_{RA}}{2} = \tag{26}$$
$$= \frac{g \, J_{RA} H_{RA}^2}{16 \, v \, R^2} \cdot \left(2R^2 - 2RH_{RA} + H_{RA}^2\right)$$

$$\omega_{RA} = \frac{V_{sr.RC}}{H_{RA}} = \tag{27}$$
$$= \frac{g \, J_{RA} \, H_{RA}}{4 \, v \, R^2} \cdot \left(2R^2 - 2RH_{RA} + H_{RA}^2\right)$$

$$a_{max.RA} = \omega_{RA}^2 \frac{H_{RA}}{2} = \frac{V_{sr.RC}^2}{H_{RA}} = \tag{28}$$
$$= \frac{g^2 \, J_{RA}^2 \, H_{RA}^3}{64 \, v^2 \, R^4} \cdot \left(2R^2 - 2RH_{RA} + H_{RA}^2\right)^2$$

In RB subspace the characteristic vectors of primary cycloidal motion velocity field are:

$$V_{max.RBC} = \frac{1}{2}V_{sr.RC} = \omega_{RB}\frac{H_{RA}}{2} = \tag{29}$$
$$= \frac{g \, J_{RB} \, H_{RB}^2}{16 \, v \, R^2} \cdot H_{RA} H_{RB}$$

$$\omega_{RB} = \frac{V_{sr.RC}}{H_{RB}} = \frac{g \, J_{RB} \, H_{RB}}{4 \, v \, R^2} \cdot H_{RA} H_{RB} \tag{30}$$

$$a_{max.RB} = \omega_{RB}^2 \frac{H_{RB}}{2} = \frac{V_{sr.RC}^2}{H_{RB}} = \tag{31}$$
$$= \frac{g^2 \, J_{RB}^2 \, H_{RB}^3}{64 \, v^2 \, R^4} \cdot H_{RA}^2 H_{RB}^2$$

The energy line gradient resulting from active resistance:

$$J_{RC} = \lambda_{RC}\frac{1}{2R}\frac{\alpha_{RC} \, V_{sr.RC}^2}{2g} = \alpha_{RA}J_{RA} + \alpha_{RB}J_{RB} = \frac{4v \, \alpha_{RA} \, R^2 \, V_{sr.RC}}{g \, H_{RA}^2 \left(2R^2 - 2RH_{RA} + H_{RA}^2\right)} + \frac{4v \, \alpha_{RB} \, R^2 \, V_{sr.RC}}{g \, H_{RA} \, H_{RB}^3} =$$
$$= \frac{4 \, vv^2 \, V_{sr.RC}}{g \, H_{RA}}\left[\frac{\alpha_{RA}}{H_{RA}\left(2R^2 - 2RH_{RA} + H_{RA}^2\right)} + \frac{\alpha_{RB}}{H_{RB}^3}\right]\frac{8 \, R^2}{8 \, R^2}\cdot\frac{V_{sr.RC}}{V_{sr.RC}} =$$
$$= \frac{32 \, C_R}{\dfrac{V_{sr.RC} \cdot 2R}{v}}\cdot\frac{R^4}{H_{RA}}\left[\frac{\alpha_{RA}}{H_{RA}\left(2R^2 - 2RH_{RA} + H_{RA}^2\right)} + \frac{\alpha_{RB}}{H_{RB}^3}\right]\frac{1}{2 \, R}\cdot\frac{V_{sr.RC}^2}{2g} \tag{32}$$

where, λ_{RC}—coefficient of linear resistance of active forces (Darcy's formula):

$$\lambda_{RC} = \frac{32C_R}{Re_R} \cdot \frac{R^4}{H_{RA}}\left[\frac{1}{H_{RA}\left(2R^2 - 2RH_{RA} + H_{RA}^2\right)} + \frac{1}{H_{RB}^3}\right] \tag{33}$$

$$\alpha_{RC} = \frac{\dfrac{\alpha_{RA}}{H_{RA}\left(2R^2 - 2RH_{RA} + H_{RA}^2\right)} + \dfrac{\alpha_{RB}}{H_{RB}^3}}{\dfrac{1}{H_{RA}\left(2R^2 - 2RH_{RA} + H_{RA}^2\right)} + \dfrac{1}{H_{RB}^3}} = \frac{\alpha_{RA}H_{RB}^3 + \alpha_{RB}H_{RA}\left(2R^2 - 2RH_{RA} + H_{RA}^2\right)}{H_{RB}^3 + H_{RA}\left(2R^2 - 2RH_{RA} + H_{RA}^2\right)} \tag{34}$$

$$\alpha_{RA} = \frac{2RH_{RA}}{2R^2 - 2RH_{RA} + H_{RA}^2} = \frac{2\pi RH_{RA}}{F_{RA}} \tag{35}$$

where, $R \leq H_{RA} \leq 2R$

$$\alpha_{RB} = \frac{2R}{2R - H_{RB}} = \frac{2\pi RH_{RB}}{F_{RB}} \tag{36}$$

where, $0 \leq H_{RB} \leq R$

7. Primary Cycloidal Motion in the Active Forces Field—Force Field Structure

The above described relationships in the field of active forces (based on Poiseuille's laminar motion model) can be simultaneously described on the basis of the cycloidal motion model. In cycloidal motion, the structure of the primary field of active forces in non-peaceful flow (C_R) is a derivative of the structure of the velocity field with respect to time. The said structure consists of two component structures: force field of primary semi-cycloidal motion and force field of primary semi-laminar motion. All mathematical relationships deduced for the force field of semi-cycloidal motion are true for the mathematical description of the force field of semi-laminar motion.

Internal friction forces of both components are equal to each other. A graphical representation of the structure is presented in Figs. 3 and 4.

7.1 Structure of the Primary Field of Semi-cycloidal Motion Forces

In non-peaceful flows ($Re_{pr} < Re \leq Re_{gr}$) the boundary between the two subspaces (RA and RB) goes beyond the axis of the duct and moves towards its wall, as the Re value grows. It forms an axi-symmetric core of the radius $R1 = (H_{RA} - H_{RB})/2 = H_{RA} - R$ in the axis of the duct. Outside the core an annular boundary layer of thickness H_{RB} is formed, where $H_{RA} + H_{RB} = 2R$ and $F_{RA} + F_{RB} = 2F$. At the boundary of both fields the maximum velocities continue to be equal ($V_{max.RC} = V_{max.RA} = V_{max.RB}$).

Bearing in mind the principles of modeling peaceful flows [2], it was assumed that the value of semicycloidal motion forces forming the structure of progressive primary semicycloidal motion is equal to Newtonian forces, in accordance with formulas:
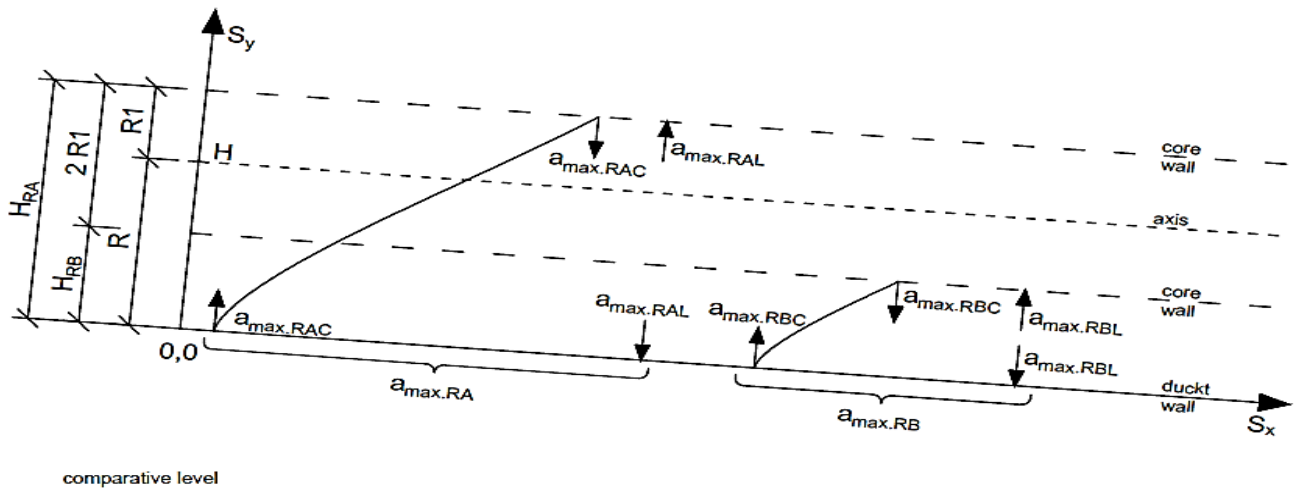
Fig. 3   Axial section of the primary field of active forces.
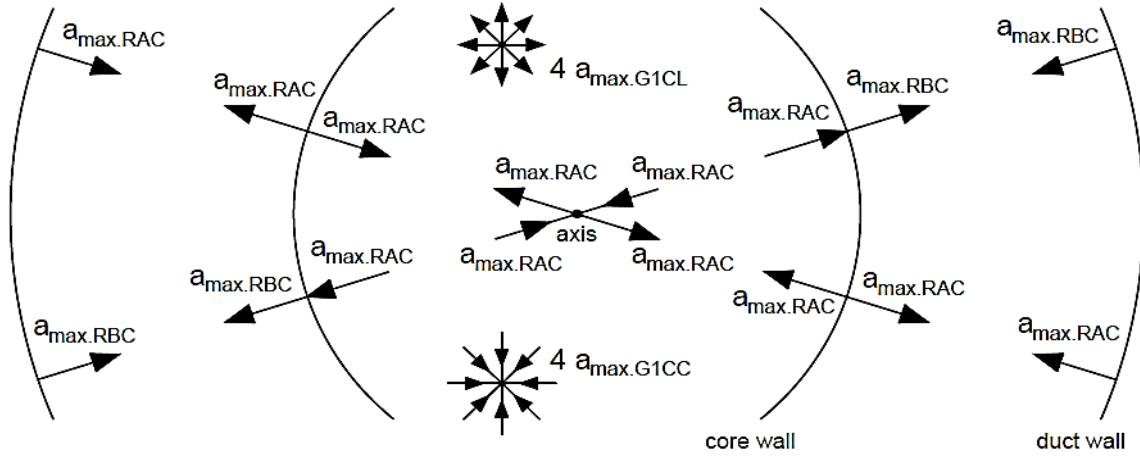
Fig. 4 Cross-section of the primary field of internal forces (accelerations) of semi-cycloidal motion.

$$P_{RCC} = \pi \left(2R^2 - 2RH_{RA} + H_{RA}^2 \right) \rho \; \frac{V_{max.RCC}^2}{4H_{RA}} + \pi \left(2\, RH_{RB} - H_{RB}^2 \right) \rho \; \frac{V_{max.RCC}^2}{4H_{RB}} = \tag{37}$$

$$= \frac{\rho}{2} \left(F_{RA}\, a_{max.RAC} + F_{RB}\, a_{max.RBC} \right) = \rho \cdot \frac{C_R^2\, V_{sr.RC}^2\, F}{R} \cdot \left(\frac{F_{RA}}{F}\, \frac{R}{H_{RA}} + \frac{F_{RB}}{F}\, \frac{R}{H_{RB}} \right)$$

$$a_{max.RAC} = \frac{g}{8} \cdot \frac{a_{max.RAC}}{a_{max.pr.RAC}} = \frac{g}{8} \cdot \frac{2\, C_R^2\, V_{sr.RC}^2}{H_{RA}} \cdot \frac{2\, R}{V_{sr.pr.RC}^2} = \frac{g}{8} \cdot \frac{R}{H_{RA}} \cdot \frac{4\, C_R^2\, Re_{RC}^2}{1962^2} = \frac{g}{8} \cdot \frac{R}{H_{RA}} \cdot \left(\frac{C_R\, Re_{RC}}{981} \right)^2 \tag{38}$$

$$a_{max.RBC} = \frac{g}{8} \cdot \frac{a_{max.RBC}}{a_{max.pr.RBC}} = \frac{g}{8} \cdot \frac{2\, C_R^2\, V_{sr.RC}^2}{H_{RB}} \cdot \frac{2\, R}{V_{sr..pr.RC}^2} = \frac{g}{8} \cdot \frac{R}{H_{RB}} \cdot \frac{4\, C_R^2\, Re_{RC}^2}{1,962^2} = \frac{g}{8} \cdot \frac{R}{H_{RB}} \cdot \left(\frac{C_R\, Re_{RC}}{981} \right)^2 \tag{39}$$

The intensity of the motion's field force ($a_{max.RAC}$, $a_{max.RBC}$) increase their value as dynamics of flow accrues, measured by the Reynolds number of the primary flow Re_R, where, $R \leq H_{RA} \leq 2R$.

The resulting dynamic negative pressure at the core ($a_{maxRBC} \geq a_{maxRAC}$) introduces instability to the structure of the primary field of semi-cycloidal motion forces. Theoretically this causes the risk of implosion of fluid into the core, but the said risk is not observed empirically. This means that the dynamic pressure between the core and the ring must be equalized, which indeed takes place. The core field of internal forces (unitary accelerations) of semi-cycloidal motion is supplemented with freed antigravitons ($a_{max.G1CL}$) "borrowed" from the primary core field of opposition forces. At the same time, the ring field of internal forces (unitary accelerations) of semi-cycloidal motion "lends" its freed gravitons ($a_{max.G1CC}$) to the primary ring field of opposition forces.

7.2 Structure of the Field of Semi-laminar Motion Forces

The structure of the primary field of semi-laminar motion forces is formed by an infinite set of lines transmitting oscillation forces of individual molecules ($a_{max.RAL}$, $a_{max.RBL}$), the said lines being perpendicular to the directional lines of fluid momentums. The said structure differs from the above-described structure of the primary field of semi-cycloidal motion forces. Nevertheless, in accordance with the dualism theory both structures are derivatives of the same field of velocities, which means that relationships deduced for the field of internal velocities (unitary accelerations) of the primary semi-cycloidal motion are applicable to the mathematical description of the field of forces in primary semi-laminar flow.

7.3 Formation Process of the Field of Active Forces in Cycloidal Motion

The formation sequence of orientated transmission of internal molecular forces in the structure of active forces is as follows:

• On the "ascending" path (from the duct wall along an arch approximately in the shape of a dynamic cycloid) the characteristic vector $a_{max.RAC}$ passes through the core wall and then through the core axis—the path ends at the opposite core wall—the vector $a_{max.RAC}$ is oriented centripetally;

• The "ascending" path (from the duct wall) of the characteristic vector $a_{max.RBC}$ is shorter—it ends at the first core wall—the vector $a_{max.RBC}$ is also oriented centripetally; the ratio of the value of the vector $a_{max.RAC}$ to the value of the vector $a_{max.RBC}$ is:

$$\frac{a_{max.RAC}}{a_{max.RBC}} = \frac{a_{max.RA}}{a_{max.RB}} = \frac{H_{RB}}{H_{RA}} \quad (40)$$

• Dynamic negative pressure is formed in the core (with forces oriented centripetally), which manifests itself at the core wall with the following difference $a_{max.RBC}$—$a_{max.RAC}$;

• To prevent temporary implosion of fluid into the core, active forces temporarily "borrow" freed antigravitons from opposition core forces ($a_{max.G1L}$), and they simultaneously "lend" their freed progravitons ($a_{max.G1C}$) to opposition ring forces—it creates a new balance of forces:

$$a_{max.G1C} = a_{max.G1L} =$$
$$= a_{max.RA} + a_{max.RB} = \frac{1}{2}a_{max.G1} \quad (41)$$

• The equality of accelerations (forces) of semi-cycloidal motion (RC) on the one hand and accelerations (forces) of semi-laminar motion (RL) on the other shows that as a result of the above-described exchange of freed gravitons the intensity of the primary core field of accelerations (forces) is temporarily equalized with the primary ring field of accelerations (forces), where,

$$2a_{max.RA} + a_{max.G1L} = 2a_{max.RB} - a_{max.G1C} =$$
$$= a_{max.RA} + a_{max.RB} = \frac{1}{2}a_{max.G1} \quad (42)$$

7.4 Structure of the Primary Field of Active Forces (of Cycloidal Motion Forces)

The structure of the primary field of active forces is a sum of forces of semi-cycloidal motion and semi-laminar motion.

The structures of those motions are built differently, but their values are equal. Thus, the aggregated value of those forces (C_R) is equal to Newtonian forces, in accordance with the following:

$$P_{RC} = \rho \cdot \frac{C_R^2 \, V_{sr.R}^2 \, F}{R} \cdot \left(\frac{F_{RA}}{F} \frac{R}{H_{RA}} + \frac{F_{RB}}{F} \frac{R}{H_{RB}} \right) \quad (43)$$

$$a_{max\,RB} - a_{max.RA} =$$
$$= \frac{g}{8} \cdot \frac{R(H_{RA} - H_{RB})}{H_{RA} \cdot H_{RB}} \cdot \left(\frac{C_R Re_R}{981} \right)^2 \quad (44)$$

$$a_{max.RA} = \frac{g}{8} \cdot \frac{a_{max.RA}}{a_{max.pr.RA}} = \frac{g}{8} \cdot \frac{2 C_R^2 V_{sr.R}^2}{H_{RA}} \cdot \frac{2R}{V_{sr.pr.R}^2} = \frac{g}{8} \cdot \frac{R}{H_{RA}} \cdot \frac{4C_R^2 Re_R^2}{1{,}962^2} = \frac{g}{8} \cdot \frac{R}{H_{RA}} \cdot \left(\frac{C_R Re_R}{981} \right)^2 \quad (45)$$

$$a_{max.RB} = \frac{g}{8} \cdot \frac{a_{max.RB}}{a_{max.pr.RB}} = \frac{g}{8} \cdot \frac{2 C_R^2 V_{sr.R}^2}{H_{RB}} \cdot \frac{2R}{V_{sr..pr.R}^2} = \frac{g}{8} \cdot \frac{R}{H_{RB}} \cdot \frac{4 C_R^2 Re_R^2}{1{,}962^2} = \frac{g}{8} \cdot \frac{R}{H_{RB}} \cdot \left(\frac{C_R Re_R}{981} \right)^2 \quad (46)$$

8. Instability Phases of the Structure of Primary Field of Active Forces

The above-described structure of the primary field of active forces stabilizes only after the exchange of freed gravitons with the field of opposition forces, which entails certain consequences. Namely, the field of opposition forces is destabilized. Such instability can only be temporary, which is why it is referred to as phase I instability.

The flow being steady, phase I instability is converted to subsequent, cyclically consecutive phases of instability. In a single cycle each "molecular chaos" introduced by the exchange of gravitons is always neutralized by forces restoring order to that "chaos".

The time shift between each cycle phase causes temporary, weak fluctuation in fluid flow, making it non-peaceful. Below, four characteristic instability phases are identified. They are marked with Roman numerals I, II, III and IV, where,

- phase I—is the initial phase (described above);
- phase II—is the phase of forming secondary gravitational field in the core;
- phase III—is the phase of forming secondary motion by means of primary active forces;
- phase IV—is the phase of sustaining secondary motion by means of primary opposition forces.

Despite the lack of stability of the structure of force fields, all internal forces induced by fluid flow are fully utilized in each phase to induce the flow. In all instability phases of the structures of primary field of active forces, the intensity of the primary core field of accelerations (forces) is equal to the intensity of the primary ring field of accelerations (forces), as shown graphically in Fig. 5.

9. Phase II of Structure Instability of the Primary Active Forces Field

Momentary arrest of the vector $a_{max.RA}$ in the core in phase I causes changes to the vector's action. Its "ascending" path ($a_{max.RAC}$) does not go through the core axis, but is divided into components:

- $a_{max.RANC}$—perpendicular to the core axis;
- $a_{max.(R1)C}$—longitudinal to the core axis.

This division, taking place in the axis, causes a similar division of the vector $a_{max.RAC}$, first at the liquid core wall, then at the rigid duct wall. However, the sense of the component $a_{max.(R1)C}$ at the duct wall is opposite to sense of the corresponding component at the axis. Thus, both components temporarily form a couple of forces, resulting in a couple forces moment.
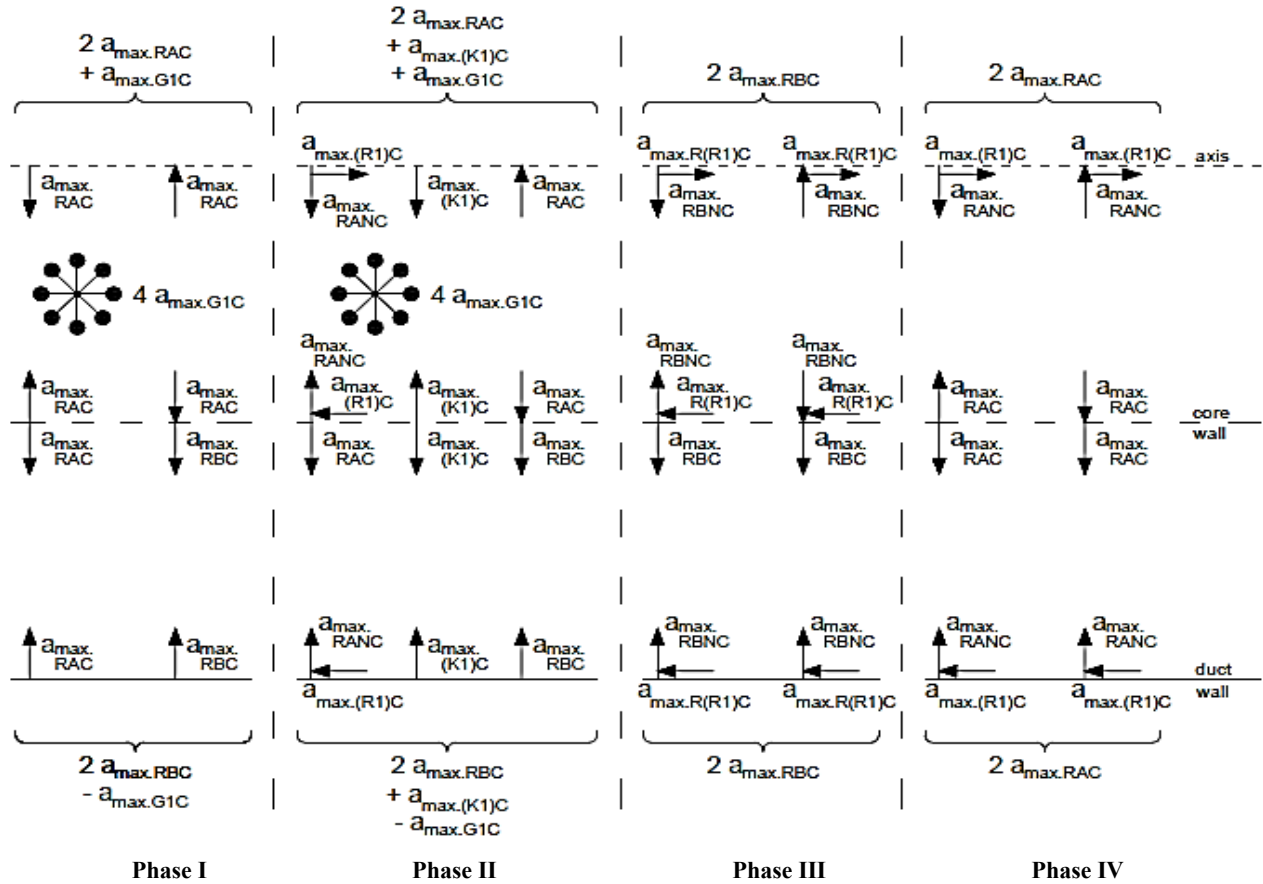

Fig. 5   Instability phases of the structure of the primary field of forces (accelerations) in semi-cycloidal motion.

The vector of semi-laminar motion $a_{max.RAL}$ behaves adequately to the vector of semi-cycloidal motion $a_{max.RAC}$. One of the consequences is that the above-described moment of a couple of forces, built by the forces of semi-cycloidal motion, is immediately neutralized by the forces of semi-laminar motion.

9.1 Normal Acceleration in the Duct Axis

Once the threshold Reynolds number is exceeded ($Re_{pr} > 1,962$), the value of the primary normal (perpendicular and centripetal) acceleration vector to the axis and direction of the flow $a_{x.RAN}$ is as follows:

$$a_{x.RAN} = a_{max.RA} \cdot \left(1 - 2\frac{V_{x.RA}}{V_{max.RA}}\right) =$$
$$= a_{max.RA} \cdot \left(1 - 2\frac{R^2 - (R - h_{RA})|R - h_{RA}|}{R^2 - (R - H_{RA})|R - H_{RA}|}\right) \quad (47)$$

For $h_{RA} = R$ and $H_{RA} \geq 1$ (subspace RA) the above equation takes the following form:

$$a_{max.RAN} = B_{R1} \cdot a_{max.RA} =$$
$$= a_{max.RA} \cdot \frac{R^2 - (H_{RA}\text{-}R)^2}{R^2 + (H_{RA}\text{-}R)^2} \quad (48)$$

where,

$$B_{R1} = \frac{a_{max.RAN}}{a_{max.RA}} = 1 - \frac{2(H_{RA}\text{-}R)^2}{R^2 + (H_{RA}\text{-}R)^2} =$$
$$= \frac{R^2 - (H_{RA}\text{-}R)^2}{R^2 + (H_{RA}\text{-}R)^2} = \frac{F_{RB}}{F_{RA}} \quad (49)$$

9.2 Longitudinal Acceleration in the Duct Axis

The longitudinal to the core axis vector of primary acceleration $a_{max.(R1)}$ becomes consistent with the following dependency, when the Reynolds number exceeds the threshold value ($Re_{pr} > 1,962$),

$$a_{max.(R1)} = a_{max.RA} - a_{RAN} = (1 - B_{R1})a_{max.RA} \quad (50)$$

9.3 Longitudinal Acceleration Accumulation in the Duct Axis—

Longitudinal acceleration measured by means of the vector $a_{max.(R1)}$ has an unusual direction of action along the axis.

As a result of such orientation, the force in the fluid acts like a wedge driven into the core axis and near the duct wall. The wedge in the axis "expands" transversely in the core fluid medium. The wedge at the duct wall "pushes" against that wall. Both forces generate forces of centripetal action (perpendicular to the wall) in the fluid. The latter forces in the ring (at the boundary layer) do not meet any counterbalancing forces, which results in their accumulation. At the core wall they reach the value $a_{max.KK1}$, where:

$$a_{max.KK1} = a_{max.(R1)} \frac{2\pi R}{2\pi R1} = a_{max.(R1)} \frac{R}{R1} =$$
$$= (1 - B_{R1}) a_{max.RA} \frac{R}{R1} \quad (51)$$

9.4 Secondary Gravitational Field

The secondary gravitational field creation will be described below, when discussing the phase II of structure instability of the primary opposition forces field in the core.

10. Phase III of Structure Instability of the Primary Active Forces Field

As a result of the accumulation of active forces in the core in phase II, the intensity of the primary core field of accelerations (forces) becomes momentarily greater than the intensity of the primary ring field of accelerations (forces). This imbalance invokes the next phase (III) of structure instability of the primary active forces field.

A characteristic feature of phase III is that active forces temporarily seize from opposition forces all freed gravitons $a_{max.G1}$. For that seizure to occur, the vector $a_{max.RAC}$ (generated in phase II at the duct wall) is converted in phase III into one, and then into two vectors $a_{max.RBC}$, each of which is divided into component vectors $a_{max.RBN}$ and $a_{max.R(R1)}$, where,

$$a_{max.RBN} = a_{RAN} \cdot \frac{a_{max.RB}}{a_{max.RA}} =$$
$$= B_{R1} \cdot a_{max.RA} \cdot \frac{H_{RA}}{H_{RB}} \quad (52)$$

$$a_{\max.R(R1)} = a_{\max.(R1)} \cdot \frac{a_{\max.RB}}{a_{\max.RA}} =$$

$$= \left(1 - B_{R1}\right) a_{\max.RA} \cdot \frac{H_{RA}}{H_{RB}} \qquad (53)$$

The amplification of longitudinal forces at the core wall (now described with the vector $a_{\max.R(R1)}$, where $a_{\max.R(R1)} \geq a_{\max.(R1)}$) results in a similar amplification of the vector $a_{\max.R(R1)}$ at the core wall and in the core axis. However, the sense of the component $a_{\max.R(R1)}$ at the wall is opposite to the sense of the component $a_{\max.R(R1)}$ in the axis. Consequently, a couple of forces is temporarily formed, resulting in an amplified couple forces moment. Amplification of the longitudinal force in the core axis results in equalization of intensities in the core and ring fields of active forces (to the value $2a_{\max.RB}$).

The new forces balance in the duct is schematically shown in Fig. 6.

10.1 Normal Acceleration at the Duct Wall

In phase III, the vector field of normal accelerations (active forces) in the boundary layer is built by the vector $a_{\max.RBN}$. As will be shown below, at the duct wall and in its axis the vector $a_{\max.RBN}$ is joined by the opposition forces vector $a_{\max.RL}$.

The sum of these two vectors forms together the primary parietal normal acceleration vector $a_{\max.RN}$ in accordance to Eq. (54):

$$a_{\max.RN} = a_{\max.RBN} + a_{\max.RL} =$$

$$= B_{R1} \cdot a_{\max.RB} + a_{\max.RL} \qquad (54)$$

It is worth emphasizing that the duct wall is the geometrical place of application points of uniformly (transversely to the flow direction) oriented molecular forces. At the wall, the oscillating motion of molecules forming the side monolayer is exactly perpendicular to the directional lines of fluid momentum. It is the only place where transverse motion occurs in its pure form.

11. Phase IV of Structure Instability of the Primary Active Forces Field

The structure of active forces built on "borrowed" gravitons in phase III is not stable. Therefore, it is transformed into phase IV of instability, characterized by the process of "returning" all freed gravitons back to opposition forces. This means the breakdown and the end of the structures of secondary motion velocities (momentums) and accelerations (forces), built by means of primary motion active forces.

In phase IV, the said structures are intercepted by opposition forces (previously enriched by gravitons) which transform them into structures for sustaining secondary motion by means of opposition forces. The said name results from the fact that opposition forces are weaker than active forces, and therefore, the newly formed structures are weaker as well. They can only sustain the existing motion. This means (in steady flows) a quick closure of phase IV of the cycle and quick return to the initial structure (phase I).

11.1 Physic Laws and Structures Instability

In solid state physics, velocity (momentum unit) is the first derivative of displacement with respect to time. Acceleration (force unit) is the first derivative of velocity with respect to time and the second derivative of displacement with respect to time [6].

In discussed above case (non-peaceful flow), the road of forces unit displacement means a stable unit of the physical, under steady flow. The first derivative of stable displacement (velocity field) also means a stable physical unit. But the derivative of a stable velocity field (acceleration field) means already unstable unit. This instability is returnable passed to the velocity field. But this instability only marginally affects the stability of road of forces unit displacement in fluid in motion.

The shown above returnable transfer of stability and instability of vector fields is beneficial for the flow. It brings a reduction of flow resistance. It will be shown below, also by graphically in the depending chart on $\lambda = f(Re)$.

12. Primary Laminar Motion in the Opposition Forces Field

Primary laminar motion (L_R) in the field of opposition forces of non-peaceful flow derives from

(a) Simplified structure   **(b) Expanded structure**
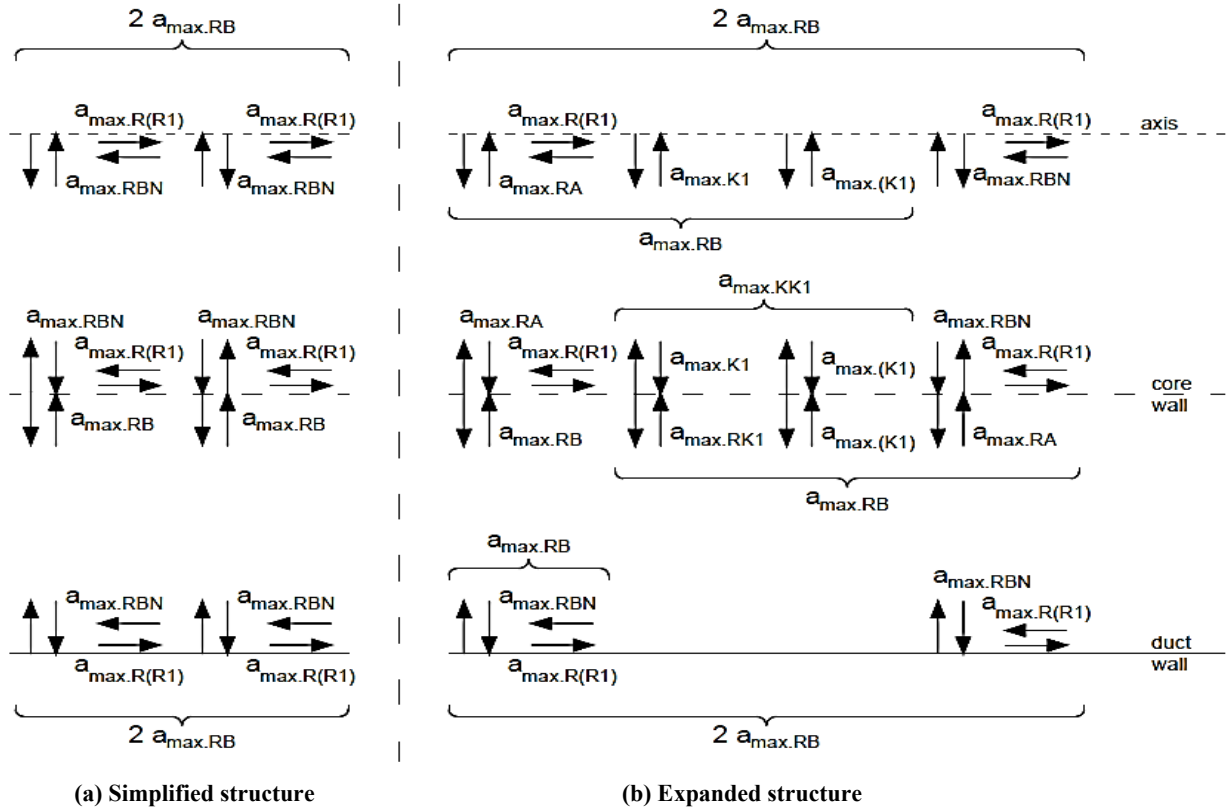
Fig. 6   Structure of primary accelerations (active forces) field in phase III.

laminar motion of peaceful flows. This motion (RL) pervades the entire phase space of fluid in a duct of the radius R. Under the new condition, the said motion becomes similar to primary cycloidal motion, but it is less meaningful and does not form a flow core. Thus, the description of the field of momentums (velocities) of this motion assumes (in the longitudinal section) a characteristic parabolic shape (like in peaceful flows). The maximum velocity value is

$$V_{\max.RL} = 2\,V_{sr.RL} = \frac{g\,J_{RL}\,R^2}{4\,v\,\alpha_{RL}} \qquad (55)$$

where, $\alpha_{RA} = 2R$.

The primary laminar motion is built of opposition forces (L_R). It is already known that in non-peaceful flows the vector of intensity of the primary field of those forces $a_{\max.RL}$ is unable to grow, despite a growth in flow dynamics. To the contrary, its value is being reduced because part of gravitons, previously embedded in the motion structure, are spontaneously freed and form a field of forces of freed gravity of the

intensity $a_{\max.G1}$. The release of gravitons weakens opposition forces.

Primary forces of laminar motion (L_R) together with primary forces of primary cycloidal motion (C_R) build the primary field of internal forces ($C_R \geq L_R$).

12.1 Creation of Primary Opposition Forces Field (Creation of Lamina Motion Forces)

In line with the principles of peaceful flow modeling [2] it was assumed that the value of the forces creating the structure of the primary laminar motion field is equal to Newtonian forces, in accordance with the following formula:

$$P_{RL} = \rho\,F\,a_{\max.RL} = \pi\,R^2\,\rho\,\frac{V_{\max.RL}^2}{2R} =$$
$$= \rho \cdot \frac{2\,L_R^2\,V_{sr.R}^2\,F}{R} \qquad (56)$$

where, the value of motion force field intensity $a_{\max.RL}$ decreases proportionally to the increase of dynamics flow which is measured by Reynolds number of

primary flow Re_R in accordance with the following formula:

$$a_{max.RL} = \frac{g}{4} \frac{a_{max.RL}}{a_{max.pr}} = \frac{g}{4} \cdot \frac{2 L_R^2 V_{sr.R}^2}{R} \cdot \frac{2R}{V_{sr..pr.R}^2} = \quad (57)$$

$$= \frac{g}{4} \cdot \frac{4 L_R^2 Re_R^2}{1,962^2} = \frac{g}{4} \cdot \left(\frac{L_R Re_R}{981}\right)^2$$

12.2 Internal Friction Forces Induced by Forces of Opposition

Assumption of the principle of constancy and uniformity of the intensity of the opposition forces internal field with regard to non-peaceful flows means that the value of opposition forces and internal friction forces for those flows is constant and equal to opposition and friction forces of threshold flow.

For practical reasons, it is convenient to formulate the above dependency in the following way:

$$J_{RL} = \frac{8 v \, \alpha_{RL} \, V_{sr.RL}}{g \, R^2} = \quad (58)$$

$$= \frac{8 v \, \alpha_{1,962.RL} \, V_{1,962.sr.RL}}{g \, R^2} = J_{1,962.RL}$$

where, $\alpha_{RL} = \alpha_{1962.RL} = 2$

$$\frac{J_{RL}}{J_{1,962.RL}} = \frac{2 L_R V_{sr.R}}{V_{1,962.sr.R}} = \frac{L_R Re_R}{981} \quad (59)$$

$$J_{RL} = J_{1,962.RL} \frac{J_{RL}}{J_{1,962.RL}} = \lambda_{RL} \cdot \frac{1}{2R} \cdot \frac{\alpha_{RL} \, V_{sr.R}^2}{2g} = \quad (60)$$

$$= \frac{64 U_R^2}{981} \cdot \frac{1}{2R} \cdot \frac{\alpha_{RL} \, V_{sr.R}^2}{2g}$$

where, λ_{RL}—coefficient of linear resistance of opposing forces (Darcy's formula):

$$\lambda_{RL} = \frac{64 \, L_R^2}{981} \quad (61)$$

12.3 Instability Phases of the Structure of Primary Field of Opposition Forces

The above described instability of the structures of primary field of active forces corresponds to the instability of the structures of primary field of opposition forces. This means that also here one can

identify four phases of that instability. In this case, phase II is constructed a secondary gravitational field in the core—after prior transformation of opposition core forces into freed gravitons.

It is worth to mention that in instability phases I and II of structures of the opposition forces primary fields, core and ring intensities of the field of accelerations (forces) are not equalized as shown in Fig. 7.

13. Phase II—Phase of Constructing a Secondary Gravitational Field in the Core

Momentary secondary core gravitational field is present only in phase II. It results from the "dynamic negative pressure" trapped in the core and indirectly from radical changes in the structure of the field of active forces. In phase II in the core there exist:

• dynamic negative pressure, induced by the difference in active forces ($a_{max.RB} - a_{max.RA}$);

• laminar motion forces ($a_{max.RL}$);

• freed gravitons—forces of freed gravity ($a_{max.G1}$).

Assumption of the principle of constancy and uniformity of the intensity of the opposition forces internal field leads to a conclusion that active and opposition forces momentarily form in the core a field of centrifugally oriented forces of constant intensity. The intensity of that field is

$$a_{max.RB} \ -a_{max.RA} \ +a_{max.RL} \ =a_{max.G1L}+a_{max.RL}=0.25g \quad (62)$$

All the parameters of that field are identical to the parameters of the natural terrestrial gravitational field. Therefore, the said field is referred to as the momentary secondary core gravitational field.

It should be remembered that the secondary gravitational field in non-peaceful flows ($a_{max.RL}$, $a_{max.G1}$) is formed by the forces of the primary motion, while the gravitational field in peaceful flows ($a_{max.L}$, $a_{max.G}$) was formed by the forces of the natural terrestrial gravitational field.

13.1 Theoretical, Primary Boundary of Laminar Flows [5]

The above mechanism of creation of the secondary gravitational field simultaneously describes the
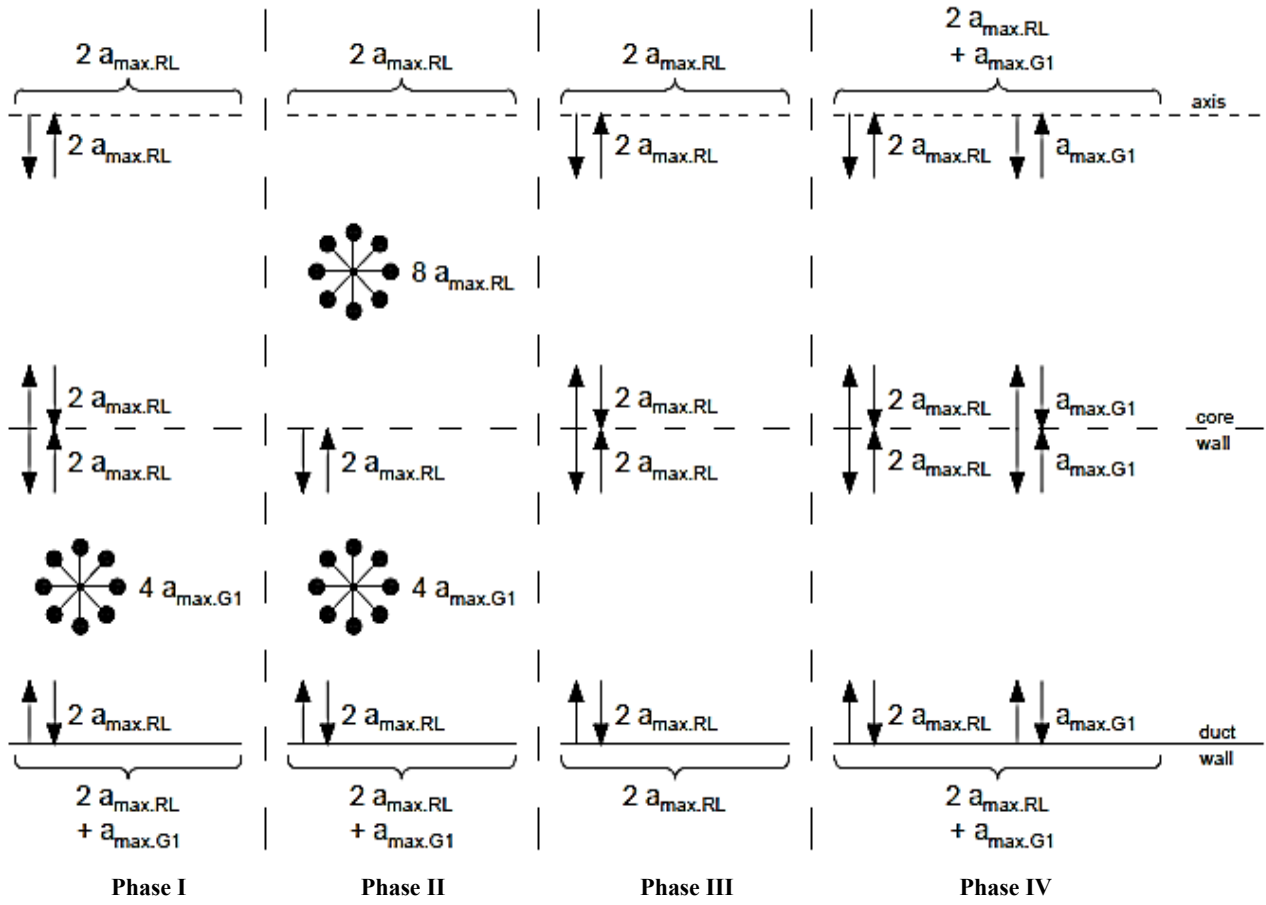
Fig. 7 Instability phases of the structure of the primary field of opposition forces (accelerations).

formation of limitations for such creation, which are identical to the limitations for the existence of laminar flows. It is obvious that the said limitations must grow together with the flow dynamics. The theoretical boundary of laminar flows can be calculated with transformation in Eq. (62):

$$\left[\frac{1}{8}\left(\frac{R}{H_{RB}}-\frac{R}{H_{RA}}\right)\left(\frac{C_R\,Re_R}{981}\right)^2\right]+ \tag{63}$$

$$+\frac{1}{4}\left(\frac{L_R\,Re_R}{981}\right)^2=\frac{1}{4}$$

$$\left(\frac{R}{H_{RB}}-\frac{R}{H_{RA}}\right)C_R^2+2\,L_R^2=2\left(\frac{981}{Re_R}\right)^2 \tag{64}$$

$$\left(2+\frac{R}{H_{RB}}-\frac{R}{H_{RA}}\right)C_R^2-4C_R+ \tag{65}$$

$$+2\left[1-\left(\frac{981}{Re_R}\right)^2\right]=0$$

The plot of the function $C_R=f(H_{RA}/R,\,Re_R)$ defines the plot of the share of the primary creation motion in the entirety of the primary flow which grows together with the flow dynamics until:

$$C_R=\frac{2-\sqrt{4-2\left(2+\dfrac{R}{H_{RB}}-\dfrac{R}{H_{RA}}\right)\left[1-\left(\dfrac{981}{Re_R}\right)^2\right]}}{2+\dfrac{R}{H_{RB}}-\dfrac{R}{H_{RA}}} \tag{66}$$

the equation makes numerical sense, which is true only if:

$$4-2\left(2+\frac{R}{H_{RB}}-\frac{R}{H_{RA}}\right)\left[1-\left(\frac{981}{Re_R}\right)^2\right]\geq 0 \tag{67}$$

$$Re_R\leq 981\sqrt{1+\frac{2\,H_{RA}\,H_{RB}}{R\,(H_{RA}-H_{RB})}} \tag{68}$$

Eq. (68) allows one to define the set of terminal Reynolds numbers of the primary motion $Re_{gr.R}$ above which non-peceful flows do not exist, because of

mathematical limitations stipulating, that the radicand of the square root must be non-negative.

The above allows one to formulate the following theorem:

"If flowing fluid is affected by natural terrestrial gravitational forces, then it has its theoretical determinable initial phase, known as laminar flow."

This statement was similarly formulated by Osborne Reynolds over a century ago. But the phrase "similarly" makes a significant difference in this particular case, as the above statement introduces the theoretical boundaries of laminar flow. The presentation introduces theoretical division of the previously already known empirical counterpart.

14. Secondary Motion

Secondary motion forces structure is formed by orientating forces, which are making order in "secondary molecular chaos" in the core. These are cumulative forces ($a_{\max.KK1}$) transversely oriented to the axis of the core (and duct).

The initial structure of the secondary motion forces field (in phases I and II) is limited to the core alone, because only in the core the secondary gravitational field (i.e., the foundation for secondary motion) is generated. In phases III and IV, the "secondary chaos" penetrates into the ring (boundary layer), which requires introduction of orientating forces, i.e., forces that form the structures of secondary motion. The final structure of those forces orientates the "secondary motion" across the entire phase space of fluid. The said structure becomes similar to peaceful flow structure, and thus the original mean core velocity $V_{sr.R1}$ formed in the core is rescaled to the final, duct velocity $V_{sr.RR1}$, in accordance with the flow continuity equation:

$$V_{śr.RR1} = V_{śr.R1}\ \frac{\pi\,(R1)^2}{\pi\,R^{\,2}} = V_{śr.R1}\left(\frac{R1}{R}\right)^2 \quad (69)$$

The formation of the structures of rescaled secondary motion ($V_{sr.RR1}$, $a_{\max.RR1}$) takes some time. First, secondary motion structures are accumulated in the core, and only after the said motion is "pushed out"

towards the boundary layer. The full structure of rescaled secondary motion is temporary. It is present only in phase III. In the remaining phases, this structure is built by active forces (phases I and II), and then it is only sustained by opposition forces (phase IV).

An interesting role in secondary motion formation is played by longitudinal forces ($a_{\max.(R1)}$, $a_{\max.R(R1)}$). Acting along the core and walls (both core and duct walls), these forces support the formation process of semi-cycloidal secondary motion (first in the core, then dispersed).

14.1 Accumulated Force Formation Sequence

The force accumulated in the core, measured by the value of the vector $a_{\max.KK1}$, is built in stages. In phase II, the longitudinal action vector $a_{\max.(R1)}$ first generates the transverse force $a_{\max.(K1)}$ in the core, and soon afterwards in the ring. As a result, in phase II, the entire phase space of fluid in motion is filled with the base transverse action vector $a_{\max.(K1)}$.

In phase III, the longitudinal (axial) action vector $a_{\max.(R1)}$ increases its value up to $a_{\max.R(R1)}$. This entails an increase in the transverse force $a_{\max.(K1)}$ in the core up to $a_{\max.K1}$. However, the said increase is limited because the value of the transverse core force vector cannot be greater than the value of the accumulated vector $a_{\max.KK1}$ newly formed in the core. Thus, the vector $a_{\max.K1}$ is unable to either "push out" or replace the base vector $a_{\max.(K1)}$. This means that a sum of vectors $a_{\max.(K1)}$ and $a_{\max.K1}$ is formed in the core. The said sum is (and must be) equal to the value of the accumulated vector $a_{\max.KK1}$, where,

$$a_{\max.K1} = a_{\max.(K1)}\cdot\frac{a_{\max.R(R1)}}{a_{\max.(R1)}} = \qquad\qquad (70)$$

$$= a_{\max.(K1)}\,\frac{a_{\max.RB}}{a_{\max.RA}} = a_{\max.(K1)}\,\frac{H_{RA}}{H_{RB}}$$

$$a_{\max.KK1} = a_{\max.K1} + a_{\max.(K1)} =$$

$$= a_{\max.K1}\cdot\left(1+\frac{H_{RB}}{H_{RA}}\right) = a_{\max.K1}\cdot\left(\frac{2R}{H_{RA}}\right) \quad (71)$$

where,

$$a_{\max.K1} = a_{\max\,(R1)}\,\frac{H_{RA}}{2\,R1} \qquad (72)$$

$$a_{\max.(K1)} = a_{\max(R1)} \frac{H_{RB}}{2 R 1} \qquad (73)$$

In phase III, the transverse force vector ($a_{\max.K1}$) formed in the core momentarily has no counterpart in the ring (boundary layer). Such counterpart is indeed necessary to complete the orientation of the "secondary molecular chaos" in the ring, partially orientated (in phase II) by the base vector $a_{\max.(K1)}$. The said counterpart is referred to as the transverse ring force vector ($a_{\max.RK1}$). As previously in the core, it is now in the ring that the increase of the value of the vector $a_{\max.RK1}$ is limited. In this case, the limitation results from the principle of constancy and uniformity of the intensity of the opposition forces internal field, assumed in the introduction to this paper. This means that:

$$a_{\max.RK 1L} + a_{\max.(K 1)L} + a_{\max.RL} =$$
$$= a_{\max.G 1L} + a_{\max.RL} = 0.25 g \approx 2.45 \ m/s^2 \qquad (74)$$

Transverse forces, formed both in the core and in the ring ($a_{\max.K1}$, $a_{\max.RK1}$) are disperse forces of secondary motion in the entire phase space of fluid in motion. In order to do so, the said forces must not be different to each other ($a_{\max.K1} \neq a_{\max.RK1}$). One may assume that the ratio of those (transverse) forces is equal to the ratio of longitudinal forces and the following dependency is true:

$$a_{\max.RK1} = a_{\max.G1L} - a_{\max.(K1)} =$$
$$= a_{\max.K1} \frac{a_{\max.R(R1)}}{a_{\max.(R1)}} = a_{\max.K1} \frac{H_{RA}}{H_{RB}} \qquad (75)$$

14.2 Share of Secondary Motion in the Entire Flow

The share of secondary motion was determined by means of Reynolds numbers assuming that in the range of non-peaceful flows ($Re_{pr} < Re \leq Re_{gr}$) secondary motion can only be peaceful ($0 < Re_{R1} \leq 1,962$ and $0 < Re_{RR1} \leq 1,962$). We know that in primary peaceful motion the following dependency is true:

$$Re = 1,962 \frac{a_{\max}}{g / 2} \qquad (76)$$

The same dependency is taken for secondary motion dependency rule:

$$Re_{R 1} = 1,962 \frac{a_{\max.KK 1}}{g / 2} \qquad (77)$$

The initial value of Reynolds number Re_{R1} (with regard to the core diameter $R1$) results from the dependency in phase III:

$$Re_{R 1} = \frac{1,962}{g / 2} (1 - B_{R 1}) a_{\max.R A} \frac{R}{R 1} \qquad (78)$$

The rescaled value of Reynolds number Re_{RR1} (with regard to the duct diameter R) results from the following dependency:

$$Re_{RR 1} = \frac{R 1}{R} Re_{R 1} = \frac{1,962}{g / 2} (1 - B_{R 1}) a_{\max.R A} \qquad (79)$$

The share of secondary motion in the entire flow of fluid is described by the following dependency:

$$Re = Re_R + Re_{RR 1} \qquad (80)$$

15. Non-peaceful Flows and Their Characteristic Values

Non-peaceful flow is described below with the use of coefficients α and λ, i.e., factors from the classical Darcy-Weisbach equation. Below, the said factors, thus far determined experimentally only, are described theoretically, for the first time in history of fluid mechanics.

15.1 Primary Motion Linear Resistance Coefficient λ_R

In the deliberations presented thus far, considerable confusion is caused by the phenomenon of the exchange of freed gravitons ($a_{\max.G1}$) between the fields of active and opposition forces. The said phenomenon makes the structure of the primary force field unstable. As a result, it becomes necessary to identify representative states of fluid in motion, based on which it will be possible to continue the mathematical description of physical phenomena. Therefore, it is necessary to assume an underlying thesis, which is as follows:

"Changes of normal acceleration at the duct wall ($a_{\max.RN}$—described in Eq. (54)) in non-peaceful flows are directly proportional to the square of the mean velocity of primary flow."

To prove the above thesis, a comparison of longitudinal forces (R) forming the primary progressive motion with transverse forces (RN) of the primary side surface motion is presented below. The said comparison was made on the basis of the cycloidal flow model [2].

Simultaneously with the above comparison, another comparison was made, this time on the basis of Poiseuille's classical mathematical-physical model; here, the compared values were internal friction forces formed as a result of the action of the forces analyzed in the first comparison. The result of both comparisons is a dependency in Eq. (82) that enables to calculate linear resistance J_R of the primary motion in non-peaceful flow, where J_R is defined in following form:

$$J_R = J_{RC} + J_{RL} = \lambda_R \frac{1}{2R} \frac{\alpha_R V_{sr.R}^2}{2g} =$$

$$= \lambda_{RC} \frac{1}{2R} \frac{\alpha_{RC} V_{sr.R}^2}{2g} + \lambda_{RL} \frac{1}{2R} \frac{\alpha_{RL} V_{sr.R}^2}{2g} \tag{81}$$

NB: Eq. (84), after being supplemented with Eqs. (85) and (86), contains two unknowns: H_{RA} and Re_R. The solution of the equation is a set of numerical pairs forming the linear function $Re_R = f(H_{RA})$. The choice of pairs is made by means of approximation in tabular form (Table 2).

The resultant values of the coefficient λ_R are also presented in a graphical form in Fig. 8, in a functional relationship with the primary motion Reynolds number Re_R.

$$\frac{J_R}{J_{RN}} = \frac{F_{RA}\, a_{max.RA} + F_{RB}\, a_{max.RB} + 2\, F\, a_{max.RL}}{2\, F\, a_{max.RN}} = \frac{\lambda_{RC} \dfrac{1}{2R} \dfrac{\alpha_{RC} V_{sr.R}^2}{2g} + \lambda_{RL} \dfrac{1}{2R} \dfrac{\alpha_{RL} V_{sr.R}^2}{2g}}{\lambda_{1962.R} \cdot \dfrac{1}{2R} \cdot \dfrac{\alpha_{1962.R} V_{sr.R}^2}{2g}} \tag{82}$$

$$\frac{J_R}{J_{RN}} = \frac{F_{RA} \dfrac{2V_{sr.RC}^2}{H_{RA}} + F_{RB} \dfrac{2V_{sr.RC}^2}{H_{RB}} + 2F \dfrac{2V_{sr.RL}^2}{R}}{2\, B_{R1}\, F \dfrac{2V_{sr.RC}^2}{H_{RB}} + 2\, F \dfrac{2V_{sr.RL}^2}{R}} = \frac{\lambda_{RC} \dfrac{1}{2R} \dfrac{\alpha_{RC} V_{sr.R}^2}{2g} + \lambda_{RL} \dfrac{1}{2R} \dfrac{\alpha_{RL} V_{sr.R}^2}{2g}}{\dfrac{64}{1962} \cdot \dfrac{1}{2R} \cdot \dfrac{2V_{sr.R}^2}{2g}} \tag{83}$$

$$\frac{\dfrac{F_{RA}}{2F} \dfrac{H_{RB}}{H_{RA}} + \dfrac{F_{RB}}{2F} + \dfrac{H_{RB}}{R} \dfrac{L_R^2}{C_R^2}}{B_{R1} + \dfrac{H_{RB}}{R} \dfrac{L_R^2}{C_R^2}} = \frac{981}{64} \left(\alpha_{RC} \lambda_{RC} + \alpha_{RL} \lambda_{RL} \right) = \frac{981}{64} \alpha_R \lambda_R \tag{84}$$

where,

$$\frac{981}{64} \alpha_{RC} \lambda_{RC} = \frac{981\, C_R\, \alpha_{RC}}{2\, \mathrm{Re}_R} \frac{R^4}{H_{RA}} \left[\frac{1}{H_{RA}\left(2R^2 - 2RH_{RA} + H_{RA}^2 \right)} + \frac{1}{H_{RB}^3} \right] \tag{85}$$

$$\frac{981}{64} \alpha_{RL}\, \lambda_{RL} = L_R^2\, \alpha_{RL} \tag{86}$$

$$\alpha_R\, \lambda_R = \alpha_{RC}\, \lambda_{RC} + \alpha_{RL}\, \lambda_{RL} \tag{87}$$

$$\alpha_R = \frac{\alpha_{RC}\, a_{max.RC} + \alpha_{RL}\, a_{max.RL}}{a_{max.RC} + a_{max.RL}} \tag{88}$$

$$a_{max.RC} = \frac{F_{RA}\, a_{max.RA} + F_{RB}\, a_{max.RB}}{F} \tag{89}$$

$$\lambda_R = \frac{\alpha_{RC}\, \lambda_{RC} + \alpha_{RL}\, \lambda_{RL}}{\alpha_R} \tag{90}$$

Table 2 Examples of primary motion characteristic values [7].

From equations No.		(28)(45)	(31)(46)	(57)	(50)	(40)	(53)	(88)	(90)
Re_R	H_{RA}/R	$a_{\max.RA}/g$	$a_{\max.RB}/g$	$a_{\max.RL}/g$	$a_{\max.(R1)}/g$	H_{RA}/H_{RB}	$a_{\max.R(R1)}/g$	α_R	λ_R
1,962	1.000	0.125000	0.125000	0.250000	0.000000	1.000000	0.000000	2.000000	0.032620
1,967	1.010	0.126303	0.128855	0.247448	0.000025	1.020202	0.000026	1.999797	0.032459
1,972	1.020	0.127668	0.132879	0.244789	0.000102	1.040816	0.000106	1.999176	0.032307
1,977	1.030	0.129098	0.137083	0.242015	0.000232	1.061856	0.000247	1.998118	0.032164
1,981	1.040	0.130333	0.141194	0.239139	0.000416	1.083333	0.000451	1.996608	0.032047
1,986	1.050	0.131909	0.145794	0.236115	0.000658	1.105263	0.000727	1.994623	0.031922
1,990	1.060	0.133295	0.150311	0.232984	0.000956	1.127660	0.001078	1.992154	0.031824
1,994	1.070	0.134765	0.155052	0.229713	0.001314	1.150538	0.001512	1.989178	0.031737
1,999	1.080	0.136609	0.160368	0.226242	0.001737	1.173913	0.002040	1.985664	0.031645
2,003	1.090	0.138278	0.165630	0.222648	0.002222	1.197802	0.002662	1.981618	0.031580
2,007	1.100	0.140059	0.171183	0.218876	0.002773	1.222222	0.003390	1.977010	0.031528
2,011	1.110	0.141965	0.177058	0.214908	0.003394	1.247191	0.004234	1.971820	0.031488
2,015	1.120	0.144011	0.183287	0.210724	0.004089	1.272727	0.005204	1.966028	0.031463
2,019	1.130	0.146216	0.189912	0.206303	0.004860	1.298851	0.006312	1.959611	0.031452
2,024	1.140	0.148919	0.197404	0.201515	0.005725	1.325581	0.007589	1.952499	0.031439
2,028	1.150	0.151517	0.204993	0.196523	0.006668	1.352941	0.009022	1.944752	0.031460
2,033	1.160	0.154693	0.213624	0.191069	0.007723	1.380952	0.010665	1.936238	0.031482
2,038	1.170	0.158174	0.222968	0.185206	0.008886	1.409639	0.012526	1.926968	0.031524
2,043	1.180	0.162018	0.233147	0.178870	0.010169	1.439024	0.014634	1.916900	0.031586
2,045	1.185	0.163911	0.238325	0.175586	0.010848	1.453988	0.015774	1.911595	0.031634
2,048	1.190	0.166302	0.244321	0.171982	0.011589	1.469136	0.017025	1.905983	0.031672
2,050	1.195	0.168445	0.250052	0.168393	0.012341	1.484472	0.018320	1.900238	0.031732
2,053	1.200	0.171136	0.256704	0.164432	0.013164	1.500000	0.019746	1.894155	0.031783
2,056	1.205	0.174013	0.263755	0.160258	0.014036	1.515723	0.021275	1.887817	0.031842
2,060	1.210	0.177538	0.271926	0.155612	0.014997	1.531646	0.022971	1.881089	0.031891
2,064	1.215	0.181348	0.280686	0.150663	0.016025	1.547771	0.024803	1.874059	0.031950
2,067	1.220	0.185023	0.289394	0.145628	0.017083	1.564103	0.026720	1.866845	0.032035
2,071	1.225	0.189554	0.299618	0.139936	0.018268	1.580645	0.028875	1.859150	0.032114
2,076	1.230	0.195120	0.311685	0.133435	0.019606	1.597403	0.031319	1.850908	0.032189
2,081	1.235	0.201410	0.325152	0.126258	0.021082	1.614379	0.034034	1.842201	0.032280
2,086	1.240	0.208683	0.340483	0.118200	0.022731	1.631579	0.037087	1.832946	0.032389
2,092	1.245	0.218110	0.359664	0.108445	0.024701	1.649007	0.040733	1.822791	0.032509
2,102	1.250	0.233833	0.389722	0.094111	0.027510	1.666667	0.045850	1.810558	0.032620
2131	1.2518497	0.292457	0.489356	0.053101	0.034887	1.673260	0.058375	1.793002	0.032706

Depending charts on $\lambda_R = f(Re_R)$ and $\lambda = f(Re)$ in Fig. 8, it shows how important is the role of secondary motion for the reduction of flow resistance.

Calculations conducted by approximation confirm the thesis presented above (described in Eq. (82)) about changes of normal acceleration at the duct wall $a_{\max.RN}$ in non-peaceful flows. This thesis can be considered as proven, because calculation results presented in Tables 2 and 3 validate the earlier assumption on the dispersion of forces of the seed of secondary motion in the entire phase space of fluid,

described in Eq. (74).

Additional evidence for the validity of above-presented thesis is the fact that at the core there is a mathematical relationship:

$$a_{\max.RB} = a_{\max.RA} + a_{\max.R(R1)} + a_{\max.KK1} \quad (91)$$

That means that all free and freed gravitons, in whole range of non-peaceful flows, are related by the structures of the motion.

NB: It follows from the analysis that transverse forces (RN) of primary side surface motion are greater
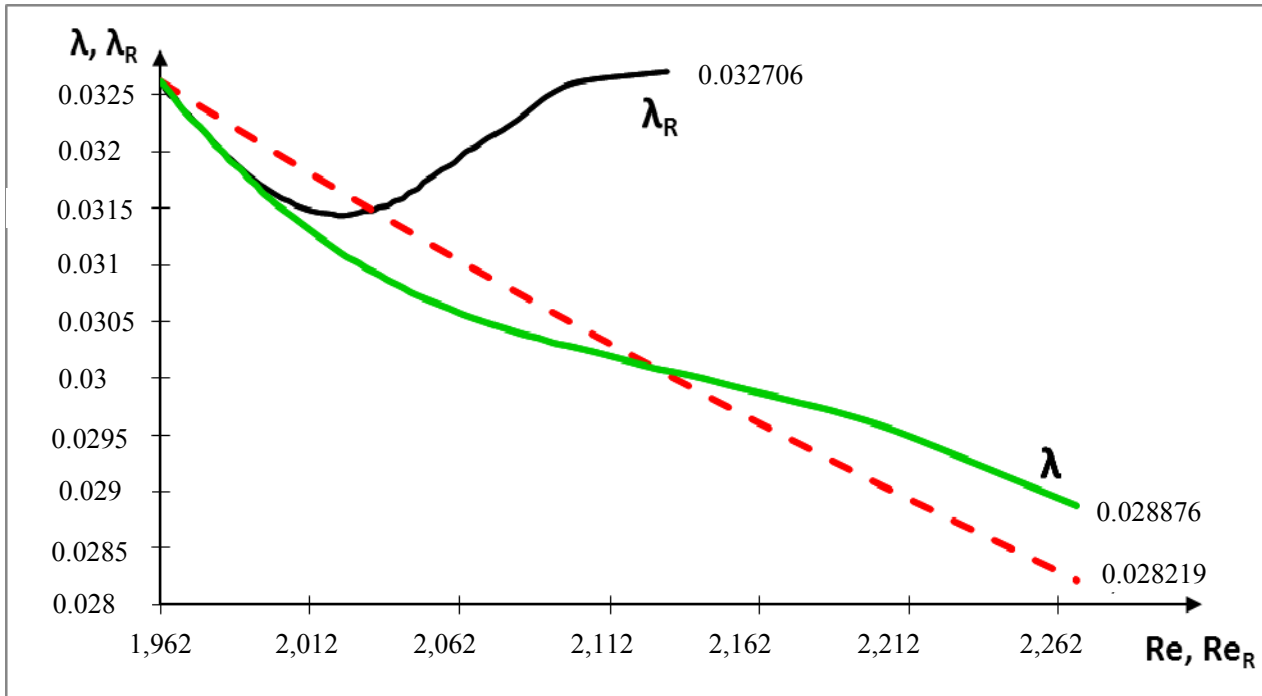
Fig. 8   Graphs of dependencies $\lambda_R = f(Re_R)$ and $\lambda = f(Re)$—solid lines with graph of dependency $\lambda = f(64/Re)$—dotted line.

than longitudinal forces (R) of the same motion and that the difference between the two grows in line with the growth in flow dynamics. This means that not only does fluid in motion increase its kinetic energy, but it also accumulates potential energy.

15.2 Linear Resistance Coefficient λ

The aggregated reduction of primary and secondary motion energy lines is equal to the reduction of primary motion energy line and the reduction of non-peaceful flow energy line, and amounts to:

$$J = J_R + J_{R1} = J_R \qquad (92)$$

It follows Eq. (87) that linear resistance of non-peaceful flow is equal to linear resistance of primary motion. The foregoing results from the fact that secondary motion is fully formed by the forces of primary motion ($J_{R1} = 0$). Under such circumstances, the product of the coefficients α_R and λ_R of aggregated (primary and secondary) flow is equal to the product of the coefficients α and λ of non-peaceful flow, and amounts to:

$$\alpha \ \lambda = \alpha_R \ \lambda_R \ \frac{V_{sr.R}^2}{V_{sr}^2} = \alpha_R \ \lambda_R \ \frac{Re_R^2}{Re^2} \qquad (93)$$

where,

$$\alpha_R \ \le \ \alpha \ \le \ 2 \qquad (94)$$

$$\frac{\alpha_R \ \lambda_R}{2} \ \frac{Re_R^2}{Re^2} \le \lambda \ \le \ \lambda_R \ \frac{Re_R^2}{Re^2} \qquad (95)$$

Eq. (94) shows that secondary motion formation in fluid introduces process flexibility to flows, thus making it possible to replace the coefficients α and λ. Such flexibility is necessary if the flow causes cyclical instability of force structures both of the primary field.

In steady flows the said flexibility is not utilized. Therefore, in the range of non-peaceful flows it was assumed that the density coefficient α always takes the value equal to $\alpha_R = 2$.

The non-peaceful flow linear resistance coefficient λ was calculated by approximation. The results of those calculations are presented in Table 3. The resultant values of the coefficient λ (at $\alpha = 2$) are presented graphically in Fig. 8, in a functional relationship with the Reynolds number of the flow Re.

15.3 Flow Velocity

The aggregated mean velocity of primary and secondary motion is equal to the mean velocity of non-peaceful flow and amounts to:

Table 3   Examples of primary and secondary motion characteristic values.

From equations No.	(73)	(51)(71)	(75)	(98)	(94)	(95)		
Re_{RR1}	Re	$a_{max.(K1)}/g$	$a_{max.KK1}/g$	$a_{max.RK1}/g$	V_{max}/V_{sr}	$\alpha = \alpha_R$	λ	$lg\,Re$	$lg\,(100\,\lambda)$
0	1,962	0.000000	0.000000	0.000000	2.000000	2.000000	0.032620	3.29270	0.51348
0	1,967	0.001250	0.002526	0.001301	1.999899	1.999797	0.032456	3.29383	0.51129
0	1,972	0.002501	0.005105	0.002710	1.999594	1.999176	0.032294	3.29500	0.50912
1	1,978	0.003753	0.007739	0.004232	1.999080	1.998118	0.032134	3.29621	0.50697
2	1,983	0.004997	0.010410	0.005864	1.998354	1.996608	0.031994	3.29724	0.50507
3	1,989	0.006250	0.013158	0.007635	1.997410	1.994623	0.031839	3.29854	0.50296
4	1,994	0.007491	0.015938	0.009526	1.996247	1.992154	0.031705	3.29967	0.50112
5	1,999	0.008730	0.018775	0.011557	1.994860	1.989178	0.031574	3.30085	0.49933
7	2,006	0.009991	0.021719	0.013768	1.993242	1.985664	0.031430	3.30229	0.49734
9	2,012	0.011234	0.024690	0.016118	1.991395	1.981618	0.031307	3.30357	0.49564
11	2,018	0.012480	0.027734	0.018644	1.989312	1.977010	0.031189	3.30490	0.49400
13	2,024	0.013732	0.030859	0.021360	1.986990	1.971820	0.031075	3.30628	0.49242
16	2,031	0.014992	0.034072	0.024284	1.984423	1.966028	0.030968	3.30772	0.49091
19	2,038	0.016262	0.037384	0.027434	1.981606	1.959611	0.030866	3.30922	0.48948
22	2,046	0.017585	0.040896	0.030900	1.978522	1.952499	0.030753	3.31100	0.48788
26	2,054	0.018893	0.044455	0.034583	1.975185	1.944752	0.030664	3.31264	0.48663
30	2,063	0.020272	0.048266	0.038659	1.971561	1.936238	0.030564	3.31456	0.48521
35	2,073	0.021691	0.052269	0.043103	1.967651	1.926968	0.030472	3.31657	0.48390
40	2,083	0.023163	0.056496	0.047966	1.963441	1.916900	0.030387	3.31867	0.48269
43	2,088	0.023896	0.058640	0.050518	1.961230	1.911595	0.030357	3.31964	0.48226
45	2,093	0.024702	0.060993	0.053316	1.958913	1.905983	0.030311	3.32087	0.48160
48	2,098	0.025473	0.063287	0.056134	1.956536	1.900238	0.030285	3.32189	0.48122
52	2,105	0.026329	0.065821	0.059239	1.954043	1.894155	0.030242	3.32318	0.48061
55	2,111	0.027216	0.068468	0.062526	1.951454	1.887817	0.030202	3.32450	0.48003
59	2,119	0.028210	0.071417	0.066178	1.948728	1.881089	0.030145	3.32610	0.47921
63	2,127	0.029255	0.074534	0.070083	1.945888	1.874059	0.030089	3.32774	0.47841
67	2,134	0.030284	0.077652	0.074088	1.942963	1.866845	0.030054	3.32920	0.47790
72	2,143	0.031461	0.081189	0.078603	1.939863	1.859150	0.030001	3.33096	0.47714
77	2,153	0.032820	0.085246	0.083746	1.936557	1.850908	0.029930	3.33303	0.47611
83	2,164	0.034314	0.089709	0.089429	1.933057	1.842201	0.029859	3.33520	0.47507
89	2,175	0.035991	0.094712	0.095809	1.929319	1.832946	0.029787	3.33750	0.47403
97	2,189	0.038060	0.100822	0.103494	1.925192	1.822791	0.029694	3.34023	0.47266
108	2,210	0.041265	0.110039	0.114624	1.920142	1.810558	0.029511	3.34438	0.46998
137	**2,268**	0.051818	0.138524	0.145081	1.911692	1.793002	0.028876	3.35562	0.46054

$$V_{sr} = V_{sr.R} + V_{sr.R\,1}\frac{(R\,1)^2}{R^2} = \frac{v\,Re_R}{2R}\left[1+\frac{Re_{RR\,1}}{Re_R}\right] \quad (96)$$

Fig. 9 presents a graph of the distribution of velocities in progressive motion. The graph shows that progressive motion velocity is a sum of three other velocities:

- primary cycloidal motion velocity V_{RC};
- primary laminar motion velocity V_{RL};
- rescaled secondary motion velocity V_{RR1}.

The maximum velocity in non-peaceful flows (V_{max}) is described by the following dependency:

$$V_{max} = \frac{v\,Re_R}{2R}\left[\frac{2\,C_R\,R^2}{2R^2 - 2RH_{RA} + H_{RA}^2} + 2\,L_R + \frac{2\,Re_{RR1}}{Re_R}\right] \quad (97)$$

$$\frac{V_{max}}{V_{sr}} = \frac{\dfrac{2\,C_R\,R^2}{2R^2 - 2RH_{RA} + H_{RA}^2} + 2\,L_R + \dfrac{2\,Re_{RR1}}{Re_R}}{1 + \dfrac{Re_{RR1}}{Re_R}} \quad (98)$$
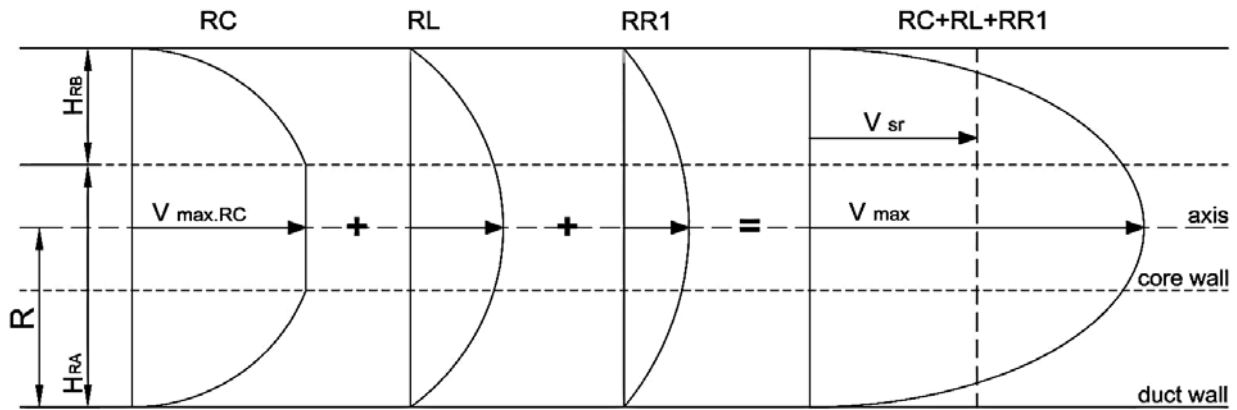
Fig. 9 Velocity $V = f(h)$ distribution graph.

It is worth emphasizing that the aggregated distribution of velocities in progressive motion of non-peaceful flow is either parabolic ($V_{max}/V_{sr} = 2$) or nearly parabolic ($V_{max}/V_{sr} \approx 2$) which means that it is consistent with the corresponding empirical distribution.

15.4 Boundary (Lower Boundary) Reynolds Number Re_{gr}

It follows from Reynolds experiment that when the flow of fluid in a tube is reduced, the numerical value Re_{gr} is always present. The said value separates turbulent flows from laminar flows. The number of Re_{gr} is referred to as the lower boundary Reynolds number. Its empirical value has never been precisely determined. In the literature two values are typically used: $Re_{gr} = 2,000$ or $Re_{gr} = 2,300$.

The purpose and the culminating point of this paper is to arrive at the theoretical value of the said number. Calculations by approximation (Tables 2 and 3) indicate that the said number is:

$$Re_{gr} = 2,268 \qquad (99)$$

The value $Re_{gr} = 2,268$ is the sum of the primary motion terminal value $Re_{gr.R} = 2,131$ and the secondary motion terminal value $Re_{gr.R1} = 137$ at $H_{gr.RA}/R = 1.2518497$.

It is worth to noting that the theoretical value of Re_{gr} is determined for steady state but also in unstable conditions at the same time induced by the successive phases of cyclic instability. This is only apparent paradox. But this paradox is useful at the moment in considerations because it credible explains the reasons of difficulties faced by researchers when trying to experimentally determine the value of Re_{gr} number. It shows in theoretical way that even small external disturbances can have influence for test results.

16. Summary and Conclusions of Ref. [2]

(1) The objective of Ref. [2] is to theoretically describe that very well-known (and described in literature) steady, axially-symmetric non-peaceful flow of homogenous Newtonian fluid through a straight-axis duct of a circular cross-section under the action of constant natural gravitational forces. Non-peaceful flows ($Re_{pr} < Re \leq Re_{gr}$) are classified as laminar flows ($0 < Re \leq Re_{gr}$);

(2) The said non-peaceful flow is described on the basis of the new theory of dualism of Newtonian fluid motion, which states that flow induces orientated oscillation motion within fluid. That motion has its own structure built of an infinite number of orientated and clearly determined lines (paths) transmitting oscillation motion and internal forces. The motion's structure has its first derivative in the form of a structure of the field of momentums (velocities) within fluid. It also has its second derivative in the form of a structure of the field of accelerations (molecular forces) within fluid;

(3) The dualism theory of oscillation-laminar motion is a novelty in fluid mechanics. It describes internal motion within fluid in two ways simultaneously, each of which is based on a physical model: an improved Poiseuille's laminar flow model and a new cycloidal motion model;

(4) The dualism theory recognizes the existence of transverse forces in fluid flows, generated by internal motion. This is the big novelty of dualism theory, because the existence of these transverse forces is confirmed by the experiences [5] while the existence of these forces is omitted in different theories of fluid flows. There are no transverse forces in Newton's Hypothesis, nor in classical Poiseuille's Law [8] and they are not determined by differential Navier-Stokes (Navier Claude Louis 1785-1836, Stokes George Gabriel 1819-1903) Equations [9];

(5) The dualism theory shows that a model (dual) description of physical phenomena taking place in fluid in motion makes it possible to develop a comprehensive, theoretical description of the orientation of motion structures and motion forming forces that induce laminar flows of fluid ($0 < Re \leq Re_{gr}$). As it will be shown in the forthcoming papers in the series, the theory will also allow for the first time in the history of fluid mechanics to develop a comprehensive, theoretical description of turbulent flows ($Re \geq Re_{gr}$);

(6) The theoretical description of non-peaceful flow shows the complexity of structures that govern this relatively simple flow. It shows that:

• non-peaceful flow creates orientated internal motion in the phase space of fluid;

• the internal forces of motion build their structures in the form of lines that transmit forces forming this motion;

• the internal forces of motion build the secondary gravitational field in core of flow first and then build the secondary motion on the basis of this gravitational field;

• internal motion structures are divided into primary motion structures and secondary motion structures;

• primary motion results from direct transformation of external forces to internal forces; it is the first motion to be created and it is formed in two differing structures: core motion (motion in the core) and ring motion (motion in the boundary layer);

• secondary motion results from transformation of primary motion internal forces to secondary motion internal forces (external forces build secondary motion in an indirect way only); secondary motion is first formed in the core (separated from the duct wall) and subsequently it is dispersed throughout the entire phase space of fluid;

• all free and freed gravitons in whole range of non-peaceful flows are related on the structures of the motion (free gravitons on primary motion structures, freed gravitons on secondary motion structures);

• secondary motion plays an important role in decreasing the flow resistance.

(7) The paper introduces a number of new notions and definitions to physics (including in particular fluid mechanics) such as:

• non-peaceful flow;

• graviton (new definition);

• internal molecular forces and their transmission lines;

• motion structure and vector field structure of velocities (momentums) and accelerations (internal forces);

• density coefficient α (new definition);

• secondary gravitational field;

• core motion and ring motion;

• primary motion and secondary motion;

• active forces and opposition forces;

• secondary gravitational field and accumulated force;

• instability of the structure of primary active forces field and others.

(8) The very specific structure characteristic only for non-peaceful flows is the secondary gravitational field in core of fluid flow;

(9) Non-peaceful flow is characterized by

empirically observed fluctuation of the structure of the field of its internal forces caused by cyclical instability of the structures of the primary active forces field. The theoretical description of this phenomenon presented in the paper explains the previously unexplainable transitory instability (untranquility) of this flow which is assumed to be steady;

(10) The culminating point of this paper is the theoretical calculation of the lower boundary Reynolds number (Re_{gr} = 2.268). Thus far, this number was calculated empirically only. The fluctuation phenomenon (as described in paper No. 2) makes empirical determination of the value Re_{gr} exceptionally difficult. This assertion is confirmed in practice since empirical values Re_{gr} quoted by different researchers differ from one another. However, in all cases they are close to the theoretical value calculated above;

(11) The theoretical value of Re_{gr} is determined for steady state but also in unstable conditions at the same time induced by the successive phases of cyclic instability. It explains the reasons of difficulties faced by researchers when trying to experimentally determine of the Re_{gr} number. It shows by theoretical way that even small external disturbances can have great influence for test results;

(12) This paper a second time demonstrates the importance of mathematical principles in solving physical problems. The theoretical value Re_{gr} (boundry Reynolds number) is calculated on the base rule which says that the radicand of the square root must be non-negative. In a previous paper, it was showed that the theoretical value Re_{pr} (threshold Reynolds number) was calculated on the another base principle which says that determinability of the arcus cosine function is limited;

(13) This paper also demonstrates that the derivative of the stable structure must not be stable under steady fluid flow conditions. For example, the derivative of a stable velocity field (acceleration field) means unstable unit. This instability is returnable passed to the velocity field. This issue will be submitted to wider analysis in next papers of the cycle.

17. Issues to Address in Paper 3

Paper No. 3 will continue to present the potential of the theory of dualism of cycloidal-laminar flow of real fluids. The analysis will concentrate on the theory of a steady axially-symmetric turbulent flow ($Re \geq Re_{gr}$) in a perfectly smooth straight-axis duct of a circular cross-section under the action of natural gravitational forces.

Thus far, turbulent flows have never been described theoretically. Contemporary, fluid mechanics does not possess a model of such flows.

Even the very flow turbulence as a physical phenomenon has not been defined so far. The theories known to date and the related calculation methods do not allow for a complete description of those flows, because the systems of equations used so far are incomplete.

The number of unknowns continues to be greater than the number of equations. Therefore, formulae typically obtained by interpolating empirical results and theories based on empirical formulas of hydraulics and pneumatics must be used.

Turbulent flows in tubes with perfectly smooth walls have been investigated by many researchers. The results of their studies are often divergent. This shows the urgency of the need to provide theoretical solutions that will systematize the knowledge of flows and provide a starting point for empirical studies.

To that end, the theory of dualism of cycloidal-laminar flow of real fluid will be extended to include turbulent flows which will be presented in paper No. 3. The said extension will be equivalent to opening the previously locked door to the turbulent flow theory.

References

[1]   S. Drobniak, T. Kowalewski, Technical Sciences: Fluid Mechanics—why is it so difficult to predict fluid motion, http://www.fundacjarozwojunauki.pl. Ch.10. Poland 2011. pp. 389-428.

[2] T. Jankowski, Introduction to the turbulent flows theory—An axially-symetric peaceful flows, Journal of Mechanics Engineering and Automation 3 (1) (2013) 35-52.

[3] R. Penrose, The Emperor's New Mind, Oxford University Press, England, 1989.

[4] A. Troskolański, Hydromechanika, Wydawnictwo Naukowo-Techniczne PWN, Warszawa, Poland, 1962.

[5] T. Jankowski, Primary motion in laminar flows, in: Proceedings of WASET ICFM, Berlin, Germany, May 2013, pp. 1215-1225.

[6] M. Rothman, The Laws of Physics, Basic Books. Inc., New York, London, 1963.

[7] T. Jankowski, Boundary theory between laminar and turbulent flows, in: Proceedings of WASET ICFM, Barcelona, Spain, February, 2013, pp.1083-1091.

[8] R. Leite, An experimental investigation of the stability of Poiseuille flow, Journal of Fluid Mechanics 5 (1) (1959) 81-96.

[9] S.M. Richardson, Poiseuille flow, Thermopedia, http://www.thermopedia.com/content/1042/?tid=104&sn =1163.